ALMA MATER STUDIORUM
UNIVERSITÀ DEGLI STUDI DI BOLOGNA

SCUOLA DI SCIENZE
Dipartimento di Fisica e Astronomia
Corso di Laurea Magistrale in Astrofisica e Cosmologia

Tesi di Laurea Magistrale

The Chandra and XMM-Newton views of the Einstein Cross

Presentata da:
Elena Bertola

Relatore:
Chiar.mo Prof.
Cristian Vignali

Correlatori:
Dott. Massimo Cappi
Dott. Mauro Dadina

Sessione IV
Anno Accademico 2017-2018

Abstract

Given the scaling relations found between the SMBH mass and the properties of their host galaxy bulge, Active Galactic Nuclei (AGN) are thought to be significantly involved in the evolution of their host galaxies. The physical characterization of AGN feedback is, however, still an open issue. It is possibly associated with the generation of massive gas outflows, that might end up expelling most of the interstellar medium and quenching the star formation. These winds are seen to rise from the innermost regions of the accretion disk as fast winds at sub-pc scales (Ultra Fast Outflows, UFOs), visible in the X-ray band. Winds are also seen at other wavelengths, related to different gas phases, showing various velocities and spatial extensions. The current idea is that UFOs, given their extreme properties, could transfer their momenta to other gas components, generating winds that could reach up to kpc scales. A few sources show both UFOs and extended molecular winds, whose kinetic properties were found to correlate as predicted by state-of-the-art models for quasar-mode feedback. UFOs are characterized by the highest outflow velocities (up to $0.2 - 0.3$ c), column densities ($\log[N_H/cm^{-2}] \simeq 22 - 24$) and ionization states ($\log[\xi/erg\ s^{-1}cm] \simeq 3 - 6$). Their characteristic signatures are blueshifted iron resonant absorption lines above ~ 7 keV. Other X-ray wind components are the Warm Absorbers (WAs), located further out from the SMBH, which show less extreme properties ($\log[N_H/cm^{-2}] \simeq 20 - 22$, $\log[\xi/erg\ s^{-1}cm] < 3$). UFOs and WAs seem to produce a sequence of N_H, ξ, v_{out} when related to their distance from the SMBH, implying them to be the two faces of the same phenomenon. Most of the studies about UFOs were carried out in bright and nearby Seyferts. Having a detection fraction of approximately $40 - 50\%$ in local AGN, the current idea is that they might be quite common, but episodic events.

UFOs are expected to be common also at higher redshift, especially at $z \simeq 1 - 2$, when both the AGN activity and the cosmic star formation density peaked, so when AGN-galaxy co-evolution and feedback are expected to be at their maxima. Actually, winds have been detected also in distant AGN, both radio-quiet and radio-loud. Gravitationally lensed quasars, by means of the induced flux amplification, offer a unique tool to obtain good quality X-ray data of distant AGN in a sustainable amount of time. In fact, almost all the UFOs detections at $z > 0.1$ are associated to gravitationally lensed quasars.

In this context, Q2237+0305 (the Einstein Cross), a quadruply–imaged radio quiet quasar lensed by a nearby spiral galaxy ($z_Q = 1.695$, $z_l = 0.0395$), is part of a larger sample of distant AGN (∼10 objects), composed of other gravitationally lensed high-redshift quasars ($z \geq 1.5$) and non-lensed high-flux distant QSOs, which will allow to statistically study the occurrence of fast X-ray winds at high redshift. Using all the available data as of Oct. 2018 (thirty-five *Chandra* archival observations and three XMM-*Newton* observations, two of them public – 2002, 2016 – and one proprietary data – PI: M. Dadina, 2018), we carried out – for the first time – a comprehensive spatially resolved, timing and spectral analysis of the Einstein Cross X-ray properties, spanning in total over 18 years (6.7 yr, source rest frame). Given the superb *Chandra* angular resolution, the four images are resolved, while XMM-*Newton* grants better quality spectra thanks to its effective area. Thus, the combination of data taken with both X-ray facilities is needed to produce a thorough analysis.

The *Chandra* single-image analysis allowed to infer that the column density is dominated by the in-situ component. We detected, for the first time, blueshifted Fe resonant absorption lines in eight (out of fourteen) spectra of the Einstein Cross at more than 90% confidence (from Monte Carlo simulations), leading to an overall confidence of $> 4\sigma$.

Regarding the XMM-*Newton* data, the most interesting features are found in the 2002 EPIC-pn spectrum. We detect a rather thick, highly ionized absorber which is outflowing at ~ 0.1c. We also detect one prominent absorption feature at $E = 7.38^{+0.12}_{-0.12}$ keV that is consistent with being produced by the wind and to be dominated by Fe XXV. This wind could actually impact on the evolution of the host galaxy, given the kinetic power it generates ($\sim 1.3\ L_{bol}$). This, combined to the outflow momentum rate ($\dot{p}_{out}/\dot{p}_{rad} \approx 28$), indicates that magnetic acceleration is partially responsible for the wind launch. The 2018 data show a prominent narrow emission line at $E = 6.84^{+0.11}_{-0.10}$ keV but do not require a reflection component. The 2018 spectrum is best reproduced by a rather thick, neutral and partial covering cold absorber, whose ionization state is too low to interpret the emission line as an ionized FeKα produced by this medium.
Having detected signatures of fast outflows in nine spectra out of a sample of sixteen, we evaluate a rough estimate of the wind duty cycle: $\gtrsim 50\%$.

Only the analysis of good signal-to-noise spectra allows to constrain the presence of this kind of winds and thus their occurrence in distant AGN. Through this kind of studies we are laying the groundwork for next generation X-ray telescopes, namely *eROSITA* (to be launched in June, 2019), that will discover new distant and luminous AGN in its all-sky survey program. These AGN can then be followed-up by XMM-*Newton* and *Chandra* in the next few years and, on a longer timescale (after 2031), by *Athena*.

Sommario

Date le relazioni di scala esistenti tra la massa del buco nero supermassiccio (SMBH) e le proprietà del bulge della galassia ospite, si pensa che i nuclei galattici attivi (AGN) siano significativamente coinvolti nell'evoluzione delle galassie ospite. La caratterizzazione dei fenomeni fisici attraverso i quali questa interazione avviene è però ancora un problema aperto. Il feedback da AGN viene in parte associato alla generazione di venti massicci, che potrebbero portare all'espulsione di grandi quantità di mezzo interstellare e alla definitiva soppressione della formazione stellare nella galassia ospite. Dalle osservazioni è stato dedotto che questi venti potrebbero esser originati come componenti molto veloci su scale del sub-pc (Ultra Fast Outflows, UFOs) nelle zone più interne del disco di accrescimento e quindi osservabili in banda X. Fenomeni di vento sono stati osservati anche ad altre lunghezze d'onda legati ad altre fasi di gas, caratterizzate da diverse velocità ed estensioni spaziali. L'idea attuale è che gli UFOs, date le loro proprietà estreme, possano trasferire la loro quantità di moto ad altre componenti di gas, generando venti che possono raggiungere distanze fino alla scala dei kpc. Alcune sorgenti mostrano sia UFOs che estesi venti molecolari; per questi oggetti è stato possibile trovare una correlazione tra le proprietà cinematiche delle due componenti di vento che è risultata essere compatibile con quanto previsto dai più recenti modelli di quasar-mode feedback. Gli UFOs sono caratterizzati dalle estreme velocità di outflow (fino a $0.2 - 0.3$ c), grandi densità di colonna ($\log[N_H/cm^{-2}] \simeq 22 - 24$) e alti stati di ionizzazione ($\log[\xi/\text{erg s}^{-1}\text{cm}] \simeq 3 - 6$). Venti di questo tipo vengono rivelati grazie alle righe risonanti blueshiftate del ferro che producono ad energie superiori a 7 keV. Altri fenomeni di vento visibili in banda X sono i Warm Absorbers (WAs), i quali si posizionano a distanze maggiori dal SMBH centrale e mostrano proprietà meno estreme ($\log[N_H/cm^{-2}] \simeq 20 - 22$, $\log[\xi/\text{erg s}^{-1}\text{cm}] < 3$). Gli UFOs e i WAs sembrano produrre una sequenza in densità di colonna, grado di ionizzazione e velocità di outflow quando sono messi in relazione alla loro distanza dal SMBH, ad indicazione del fatto che siano le due facce di un unico fenomeno. La maggior parte degli studi sugli UFOs è stata effettuata su galassie di Seyfert brillanti e vicine, ottenendo una frazione di rivelazione del 40-50% negli AGN locali. Questo ha portato all'idea attuale per cui tali venti siano eventi abbastanza comuni, ma episodici.

Ci si aspetta che gli UFOs siano fenomeni comuni anche a più alto redshift, soprattutto attorno a $z = 2$, ossia al picco dell'attività cosmica degli AGN e della densità cosmica di formazione stellare, quindi quando anche i fenomeni di co-evoluzione tra galassie e AGN e lo stesso AGN feedback erano al loro massimo; venti di questo tipo sono stati effettivamente osservati anche in AGN distanti, sia radio-loud che radio-quieti, ma al momento in un numero ancora limitato di sorgenti. I quasar lensati gravitazionalmente, grazie all'amplificazione indotta, offrono uno strumento unico per ottenere dati di ottima qualità di AGN distanti con un tempo di esposizione ragionevole. Infatti, quasi tutti gli UFOs scoperti a $z > 0.1$ sono correlati a quasar gravitazionalmente lensati.

Q2237+030 (la Croce di Einstein) è un quasar radio-quieto lensato in quattro immagini da una vicina galassia a spirale ($z_Q = 1.695$, $z_l = 0.0395$) che è parte di un più grande campione di AGN distanti ($z \geq 1.5$, 10 oggetti), sia lensati, sia AGN brillanti non lensati, costruito per studiare statisticamente la ricorrenza di questi fenomeni di vento ad alto redshift. Utilizzando tutti i dati disponibili ad ottobre 2018 (trentacinque osservazioni *Chandra* d'archivio e tre di XMM-*Newton*, due d'archivio – 2002, 2016 – e una proprietary data – PI: M. Dadina, 2018), abbiamo eseguito un'analisi globale, spazialmente e temporalmente risolta, delle proprietà spettrali in banda X della Croce di Einstein, per un totale di 18 anni di campionamento (6.7 yr nel sistema di riferimento del quasar). Data la superba risoluzione angolare di *Chandra*, è possibile risolvere le quattro immagini, mentre XMM-*Newton* permette di ottenere spettri di ottima qualità grazie alla sua area efficace. La combinazione di dati da entrambi i telescopi è fondamentale per poter produrre un'accurata analisi delle caratteristiche della sorgente.

Dall'analisi degli spettri *Chandra* delle singole immagini abbiamo ricavato informazione sulla densità di colonna del materiale che intercetta la nostra linea di vista. Data la variabilità della densità di colonna, la componente di assorbimento dominante è consistente con l'essere posta al redshift del quasar. Riveliamo per la prima volta righe blueshiftate del ferro risonante in otto (su quattordici analizzati) spettri X della Croce di Einstein, ad un livello di confidenza del 90% (ricavato da simulazioni Monte Carlo). Il livello di confidenza complessivo di questa rivelazione è superiore a 4σ.

Riguardo i dati di XMM-*Newton*, lo spettro più interessante ai fini della nostra analisi è stato quello del 2002, in cui abbiamo rivelato un assorbitore abbastanza spesso, molto ionizzato e in outflow ad una velocità ~ 0.1c. Riveliamo inoltre una riga stretta in assorbimento a $E = 7.38^{+0.12}_{-0.12}$ keV, la quale è consistente con l'essere prodotta dal vento e con l'essere dominata da Fe XXV. Questa componente di vento potrebbe effettivamente influenzare l'evoluzione della galassia ospite data la potenza cinetica che genera ($\sim 1.3\ L_{bol}$). Inoltre, combinando questo dato con il tasso di quantità di moto dell'outflow ($\dot{p}_{out}/\dot{p}_{rad} \approx 28$), si ha indicazione di una possibile accelerazione magnetica oltre che di tipo radiativo. I dati del 2018 invece mostrano una prominen-

te riga in emissione a $E = 6.84^{+0.11}_{-0.10}$ keV, ma non richiedono un continuo di riflessione. Questo spettro è riprodotto al meglio da un assorbitore freddo e abbastanza spesso, che intercetta parzialmente la linea di vista. Lo stato di ionizzazione di tale mezzo è però troppo basso per poter interpretare la riga in emissione come una FeKα ionizzata prodotta dallo stesso assorbitore.
Avendo rivelato caratteristiche tipiche di componenti di vento estreme in nove spettri su un totale di sedici, possiamo dare una stima del duty cycle di tali venti: $\gtrsim 50\%$.

Per poter vincolare la presenza di outflow estremo e fornire una stima della ricorrenza di tali venti in AGN distanti, spettri che mostrino un buon segnale-rumore sono fondamentali. Con questo tipo di studi stiamo aprendo la strada per la prossima generazione di telescopi X; ad esempio *eROSITA* (lancio previsto per giugno 2016), eseguendo una survey a tutto cielo, potrà scoprire altri AGN brillanti ad alto redshift, i quali potranno poi essere studiati nel dettaglio attraverso follow-up mirati con XMM-*Newton* e *Chandra* nei prossimi anni e, su tempi scala più lunghi (dopo il 2031), anche con *Athena*.

Contents

Chapter 1

Introduction

1.1 Active Galactic Nuclei

From observational constraints and statistical arguments, current belief is that every galaxy contains a super massive black hole (SMBH) at its gravitational center; the majority of them are quiescent, like Sgr A* at the center of our own galaxy, but approximately $1\% - 10\%$ are "active". We refer to the latter class as active galactic nuclei (AGN). These objects show an activity that cannot be ascribed to thermonuclear reactions; they are characterized by bolometric luminosities ranging from 10^{42} up to 10^{48} erg/s, covering several decades of frequency, from radio up to γ-rays (Padovani et al., 2017), and rapid time variability that imply extremely compact emission regions (i.e. high energy densities, Ulrich et al., 1997). The AGN paradigm states that this emission can be explained by accretion of matter onto a central SMBH (typical masses of $10^6 - 10^9$ $M_\odot$ Peterson, 2004): the BH is surrounded by gas that, orbiting around it, loses angular momentum and spirals towards the center, releasing gravitational energy then transformed into electromagnetic emission. This, plus the secondary processes it triggers, is powerful enough to account for the overall non-stellar AGN emission, which in some objects overcomes that of the entire host galaxy.

AGN have been catalogued, based on the average properties they show (which also depend on the selected wavelength), in many different categories and types based on the properties of the first objects detected at different wavelengths. This produced a classification that is extremely intricate, because the properties in different energy bands do not always reflect actual intrinsic differences. However, there are two main differentiations that can be made. One main distinction regards the obscuration. Mainly based on their optical and X-ray properties, AGN are divided in type I (unabsorbed) and type II (absorbed) sources. However, the analysis of their polarized emission from type II objects revealed that (almost) every type II AGN "hides" a type I (Antonucci and Miller, 1985). This was interpreted as the proof of

the AGN paradigm, meaning that all AGN are powered in the same way, but type II show additional elements with respect to type I that cause a modification of their spectra. All this led to the formulation of the "unified models" (Antonucci, 1993), which state that the different properties shown by these objects are determined by the line of sight along which we observe them. The one and only discriminating factor in this unification resides in the radio loudness[1] of the AGN, which allows the distinction in radio-loud and radio-quiet objects.

1.1.1 Accretion

When matter orbits around a compact object, it tends to outward-transfer its angular momentum due to viscosity and turbulent processes and spiral toward the center, dissipating its gravitational energy. Given a mass m, the available energy is $E = \eta mc^2$, where η is the efficiency of the conversion of gravitational energy into electromagnetic flux and c the light velocity. Such energy is radiated at a rate

$$L = \frac{dE}{dt} = \eta \dot{m} c^2 \tag{1.1}$$

where $\dot{m} = dm/dt$ is the mass accretion rate. When accreting onto an object of mass M, the falling mass m dissipates its gravitational energy at a rate of

$$L = \frac{dU}{dt} = \frac{GM}{r}\frac{dm}{dt} = \frac{GM\dot{m}}{r} \tag{1.2}$$

which, when compared to eq. (1.1), allows to find a relation between the conversion efficiency and the mass of the central object: $\eta \propto M/r$. Therefore the more massive the accreting object (or alternatively the higher the compactness), the more efficient the conversion is. Regarding the accretion onto SMBHs, the efficiency is assumed to be approximately 10%.

Even though the falling matter is dissipating its energy, the system is stable given that the outward radiation pressure is balanced by the inward gravitational force of the free falling gas. From this equilibrium, one can estimate the minimum mass of the central object and the maximum luminosity the system can irradiate. Assuming a spherical distribution of ionized gas and being $\hat{r}$ the outward radial versor, the force induced by the pressure radiation provided by the Thompson scattering is

$$\vec{F}_{rad} = \sigma_e \, P_{rad} \, \hat{r} = \sigma_e \frac{L}{4\pi r^2 c} \, \hat{r} \tag{1.3}$$

which acts on the electrons but, thanks to the electrostatic interaction, it is communicated also to the protons. The gravitational attraction produced

[1] The radio loudness parameter corresponds to the ratio of the radio flux at 5GHz and the optical one at 4400 Å (Kellermann et al., 1989)

by the central mass is equal to

$$\vec{F}_{\rm grav} = -\frac{\rm GM(m_p + m_e)}{\rm r^2}\,\hat{\rm r} \approx -\frac{\rm GMm_p}{\rm r^2}\,\hat{\rm r}, \quad \text{since } \rm m_p \gg m_e. \tag{1.4}$$

For the system to be in equilibrium, the following condition among the modules of the forces has to be satisfied:

$$\rm F_{rad} \leq F_{grav}. \tag{1.5}$$

Substituting the modules through eq. (1.3) and (1.4), one can derive the maximum rate at which the energy can be irradiated, the so-called Eddington luminosity:

$$\rm L_{Edd} = \frac{4\pi GMm_p c}{\sigma_e} = 1.26 \times 10^{38} \frac{M}{M_\odot} erg\ s^{-1} \tag{1.6}$$

from which one can derive the minimum mass that the central object needs to have in order to assure the equilibrium of a system that is irradiating at the Eddington limit:

$$\rm M_{Edd} = 8 \times 10^5\ L_{[44]}\ M_\odot. \tag{1.7}$$

Therefore, assuming a quasar of luminosity $\rm L_{QSO} \approx 10^{46} erg\ s^{-1}$ and assumed it to be at its Eddington limit, its central compact object should have a minimum mass of $\approx 10^8 \rm M_\odot$. Moreover, from eq. (1.6) one can infer that $\rm L_{Edd} \propto M$, i.e. the more luminous the AGN is, the more massive such object must be. From the timescale of the variability shown by these sources, one can derive an estimate of the size of the emitting regions ($\rm d \leq c\Delta t$). Such timescales can be of the order of days, hours, even minutes, which implies sizes as small as the Solar System. Given the lower limit to the mass determined by the Eddington luminosity and such limited size, these systems are likely to host a SMBH (Rees, 1984).

Black holes can be characterized by three parameters: mass, charge and angular momentum. They are usually assumed neutral (null charge) and the angular momentum is described by the spin of a BH, which corresponds to the adimensional angular momentum per unit mass: $\rm a = Jc/gM_{BH}^2$. It can assume all values between -1 and 1, where positive values indicate that the BH rotates in the same direction as the accreting matter, negative values indicate counter-rotation. When describing the properties of a black hole, one fundamental concept is the event horizon, which represents the distance at which the escape velocity from the gravitational well equals that of the light. Such distance is directly related to the gravitational radius:

$$\rm r_g = \frac{GM_{BH}}{c^2} \tag{1.8}$$

which is often used as unit of measure when referring to small distances from a SMBH. The event horizon directly depends on the spin of the BH; its

radius, in units of r_g, is equal to $r_{\pm} = 1 \pm (1 - a^2)^{1/2}$. For a non-rotating BH ($a = 0$) is is equal to the Schwarzschild radius: $R_S = 2r_g$. For a maximally rotating BH ($a^2 = 1$), it corresponds to the gravitational radius.

1.1.2 The basic ingredients of the AGN

The detailed structure of AGN has not been completely determined yes, but all proposed models and geometries converge on the presence of, at least, the following components, listed below and schematically drawn in the cartoon show in Figure 1.1.

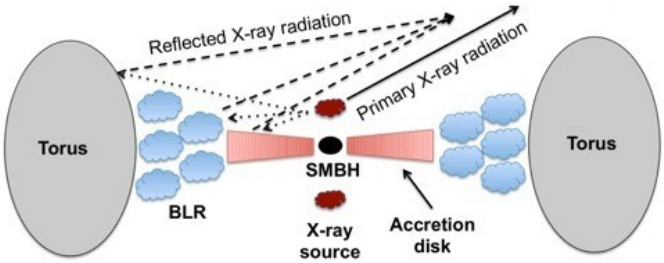

Figure 1.1: Cartoon showing the predicted structure of a radio-quiet AGN (not in scale) alongside the respective emission component, as discussed in the main text. Credit: http://www.isdc.unige.ch/~ricci/Website/AGN_in_the_X-ray_band.html.

Accretion disk. When matter is falling toward the SMBH, the system must preserve its angular momentum, inducing the formation of an accretion flow in the form of a rotating disk. From there, matter spiraling toward the central SMBH must then transfer outward its angular momentum due to viscosity and turbulence; part of the gravitational potential energy is dissipated by the gas as radiation or as kinetic energy that either causes the loss of gas, blown away as a wind, or ends up heating the disk. The accretion flow properties are still matter of debate. The commonly assumed theory is that of an optically thick, geometrically thin disk (Shakura and Sunyaev, 1973), which allows to approximate the disk emission as the superposition of many black body (multi-color black body), induced by the local dissipation of the gravitational energy of the gas. In this scenario, the disk can be considered as an ensemble of annuli, each emitting as a black body peaking at a different temperature; the total disk emission is given by the superposition of each annuli black body. Assuming that half of the dissipated gravitational energy is converted into radiation and that the other half heats up the disk, one can compute the radial profile of the disk temperature. Being $dU/dt = GM\dot{m}/r$ the rate at which the energy is dissipated (following the virial theorem), the corresponding luminosity is $L = GM\dot{m}/2r$. Applying the Stefan-Boltzmann

law to both the sides of the disk, the following equality can be found

$$\mathrm{L} = \frac{\mathrm{GM\dot{m}}}{2\mathrm{r}} = 2\pi \mathrm{r}^2 \sigma \mathrm{T}^4 \tag{1.9}$$

from which, isolating the temperature, one can derive the relation T(r):

$$\mathrm{T(r)} = \left(\frac{\mathrm{GM\dot{m}}}{4\pi\sigma \mathrm{r}^3}\right)^{1/4} \tag{1.10}$$

As eq. (1.10) predicts, the temperature of the disk grows toward the center, therefore so does the peak frequency of the annuli black body spectra. Typical temperatures are in the $10^5 - 10^6$ K range and produce a multi-color black body spectrum that covers the optical/UV band (a.k.a. big-blue bump), sometimes reaching also the soft X-ray frequencies, based on the SMBH mass.

Hot corona. The disk is predicted to be surrounded by the so-called hot corona, whose actual properties and location are still debated. The simplest modeling provides this component as the main X-ray source (two-phase model, Haardt and Maraschi, 1991), considering it as made of hot ($\mathrm{T} \sim 10^8 - 10^9$ K), rarefied ($\mathrm{n} \sim 10^8$ cm^{-3}), optically thin gas, probably placed above or within the inner part of the accretion disk at a distance of $\sim 3 - 10\ r_g$ (Fabian et al., 2015).

Broad line region (BLR) At sub-pc distances from the central source, we find the so-called Broad Line Region (BLR), which is thought to be made up of gas clouds orbiting around and partially covering the central source. The bulk motions are dominated by the central SMBH, thus the dynamical properties of this region are used to infer those of the central engine. The BLR gas reprocesses the optical/UV emission through permitted lines, while the forbidden lines are all collisionally suppressed due to the high density of the clouds ($\sim 10^{9-10}$ cm^{-3}). The temperature of the gas, given the intensity and characteristics of the emission lines, is approximately equal to 10^4 K, while the Doppler-induced broadening of the lines spans from 500 km/s to more than 10^4 km/s, producing a mean FWHM width of $\Delta\mathrm{v} \sim 5000$ km/s.

Narrow line region (NLR) At higher distances from the center (up to hundreds of parsecs), we find the Narrow line region (NLR), whose gas, as similar to that of the BLR, seems to be arranged in clouds but showing lower temperatures ($\sim 10^{3-4}$ K). The presence of forbidden lines indicates that the typical densities are also lower than those of the BLR ($\sim 10^4$ cm^{-3}) and so is the broadening of the lines ($200 \lesssim \Delta\mathrm{v} \lesssim 900$ km/s), as the name suggests. Part of the NLR is placed far enough from the central source to also contain dust. It is the only AGN region to be spatially resolved in the

optical band, where ionization cones rather than a spherical distribution can be appreciated, suggesting an axismmetric structure rather than a spherical one.

Molecular torus The region between ~ 0.1 and ~ 10 *pc* from the SMBH is referred to as the molecular torus. Its properties ($n \sim 10^{4-7}$ cm^{-3}, $\Delta v \sim 1000$ km/s, Jaffe et al., 2004) are inferred from the interpolation of those of BLR and NLR; given its distance from the ionizing source, it contains dust and molecular gas. Its actual geometry is still strongly debated (i.e. either smooth or clumpy) and so is its spatial extent. Most models do however agree on the fact that this gas shall absorb the optical/UV emission and thermally reprocesses it in the Mid-IR band, producing a black body that peaks around tens of microns, as observed.

Relativistic jets The presence of relativistic jets is seen in a small fraction ($\lesssim 10\%$) of radio-quiet AGN, but is typical for almost all the powerful radio-loud AGN. Relativistic jets are thought to be aligned with the simmetry axis of the system and seem to be originated where also the optical/UV and X-ray continuum are produced, even though the responsible mechanism is still unknown. Their emission is mainly attributed to the synchrotron and inverse Compton mechanisms which, based on the Synchrotron-Self-Compton model, can cover from the radio to the γ-ray frequencies.

Component	Approximate size
SMBH	$R_s \sim 0.01 - 10$ AU[a]
Accretion disk	$R_{in} \sim 0.01 - 60$ AU
	$R_{out} \sim 1 - 1000$ AU
BLR	$R_{BLR} \sim 0.01 - 1$ pc
Torus	$R_{torus} \sim 1 - 10$ pc
NLR	$R_{NLR} \sim 10^2 - 10^4$ pc
Jet	$R_{jet} \sim 10^2 - 10^3$pc

Table 1.1: Typical size ranges of the various AGN components, as discussed in the main text. [a] radius of the event horizon

1.1.3 AGN X-ray emission

AGN emission in the X-ray band allows to investigate the innermost regions of the system. At this wavelengths we can study the physics of the accretion phenomena, mainly through the direct emission, and also how matter is distributed around the central source, mainly analyzing how the direct emission gets reprocessed by the surrounding medium.

Direct emission. The AGN emission in the X-ray band ($\sim 0.1 - 100$ keV) can be broken down in two main components: i) the primary emission, ii) the reflection component (continuum plus FeKα line). Component i) is thought to originate in the hot corona, through thermal Comptonization of the optical/UV photons emitted by the accretion disk; they are up-scattered by the relativistic electrons of the corona, through Inverse Compton, and can undergo other up-scattering events before escaping the corona. This process generates a power-law distribution: $F(E) \propto E^{-\Gamma}$, where F(E) is the flux in units of photons$\cdot$cm^{-2}s^{-1}keV^{-1}. Typical predicted photon index values for radio-quiet sources are $\Gamma = 1.5 - 2.5$ (Haardt et al., 1997), however observationally the range seems to be narrower ($\Gamma = 1.8 - 2.0$, e.g. Perola et al., 2002; Piconcelli et al., 2005). The process is efficient until the photons are up-scattered to energies comparable to those of the relativistic electrons; this produces a cut-off in the power-law at ≥ 100 keV.

Component ii) was first predicted based on pure geometrical arguments; part of the photons reprocessed by the corona come to us directly, while another part illuminates the accretion disk, where its optically thick, relatively cold medium absorbs and re-emits the X-ray photons (see Figure 1.1). The surfacing emission is altered both at soft energies by photoelectric absorption and in the hard band by the Compton scattering with the cold electrons of the disk; thus, the reflection continuum is bump-shaped, showing a peak at $20 - 30$ keV, and is often referred to as the Reflection Hump. The interaction with the matter of the disk leaves fluorescence emission lines as signature. These are produced by the most abundant elements (i.e. Fe, O, C, Mg, Ni) in the $0.1 - 8$ keV, but only those whose intensity overcomes the primary emission can be seen in the total spectrum. The most prominent features are usually produced by iron: we find, for neutral iron, the FeKα line at 6.4 keV, the iron absorption edge at ~ 7.1 keV and, if intense enough, the FeKβ line at 7.05 keV (Makishima, 1986). The equivalent width (EW) measures the strength of a line with respect to the continuum emission. Radio-quiet type I objects present FeKα EWs that span in the range $50 - 350$ eV, with a typical value of ~ 150 eV. The described physical origin applies to a Shakura-Sunyaev standard disk, but it is still debated whether the molecular torus or even the BLR might be responsible for part, if not all, of this component.

Reprocessed emission. Many sources show a strong emission at low energies ($0.1 - 2.0$ keV), the so-called soft excess, that cannot be accounted for by the only primary emission (i.e. the power-law). Its origin is still strongly debated. One scenario indicates that this component is the high-energy tail of the disk black body emission. However, when accounted for with a thermal component in the spectral fitting process, the returned temperature of the disk is rather constant, even for sources showing considerably different

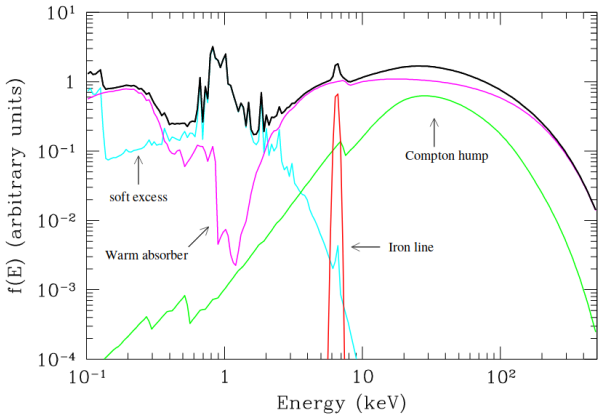

Figure 1.2: Average total spectrum (thick black line) of a type I AGN in the $0.1 - 150$ keV energy range. The primary emission (power-law) is absorbed by a warm absorber (pink line); soft excess (cyan line), cold reflection component (green line) and iron line emission (red line) are also shown. Credit: Risaliti and Elvis (2004).

SMBH masses and luminosities. This fact was interpreted as the hint of this component not being directly produced by the disk but being due to either ionized and/or complex absorption along the line of sight or reflection from the accretion disk itself, if ionized (Done et al., 2007; Petrucci et al., 2018). Intervening matter along the line of sight can produce an energy-dependent reduction of the source flux due to photoelectric absorption. The properties of such material define how the depletion takes place: thickness (in terms of column density N_H, cm^{-2}), ionization state[2], covering fraction (CF, percentage of absorbed flux with respect to the total produced by the source) are the quantities used to parameterize the absorbing matter. In particular, the thickness determines the threshold energy below which the absorption is acting: $N_H \propto E^{-3.5}$. If the material is neutral and involves all the emission produced by the source (CF = 1), all the photons below the threshold energy are absorbed. If the absorber is ionized or partially covering the source (for instance, organized in small clouds) or both of the previous cases, then not all the photons below the threshold are involved and part of the flux is seen directly.

Observationally, type II Seyferts show absorption due to neutral matter that is significantly higher than that of the Milky Way, which is thought to be produced by the molecular torus (Bassani et al., 1999). Such absorption affects the soft energy band, while the hard band is well reproduced by the same models as of type I sources, a fact that has been interpreted as a confirmation of the unified models. About 50% of AGN type I (Nandra and Pounds,

[2]The state of the gas is parameterized through the ionization parameter ξ, which depends on the X-ray luminosity L_X of the incident radiation, the gas density n and the distance from the source: $\xi = L_X/nr^2$.

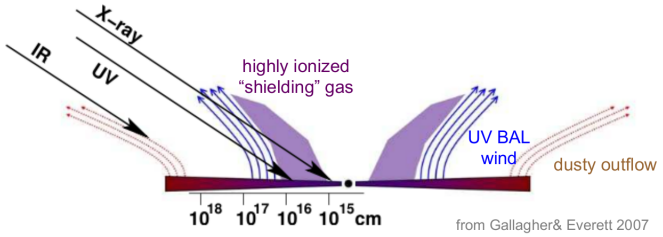

Figure 1.3: Sketch of winds arising at different radii of the accretion disk. Credit: Gallagher and Everett (2007).

1994; Piconcelli et al., 2005) show absorption features at soft energy that cannot be ascribed to the cold matter that obscures type II objects. This led to the idea of the presence of partially ionized, optically thin material, the so-called warm absorbers (WAs), placed at a distance similar to that of the BLR. With low resolution spectroscopy, the features they produce are essentially seen as prominent ionized O absorption edges but, with the advent of high-resolution gratings spectroscopy (i.e. XMM-*Newton* and *Chandra*), more line profiles have been resolved, showing these absorbers to be more complex.

After *Chandra* and XMM-*Newton* gratings observations, we now know that WAs show multiple ionization and kinetic components, outflowing at $v_{out} \approx 100 - 1000$ km/s (Kaspi et al., 2002). Their origin can be possibly interpreted as a radiatively driven wind arising from the accretion disk. Winds in the X-ray band have also been detected in the form of Ultra Fast Outflows (UFOs, Tombesi et al., 2010), which manifest themselves through blueshifted highly ionized iron resonant lines above 7 keV. These components are even more extreme than WAs, showing column densities up to $\log(N_H/cm^{-2}) \simeq 24$ and ionization parameters up to $\log[\xi/(\text{erg s}^{-1}\text{cm})] \simeq 5$. Moreover, these two gas phases (WAs and UFOs) seem to correlate when considering their typical distances from the central SMBH, i.e. UFOs are located nearer the centre than WAs. Winds have been detected also at other wavelengths at larger distances from the center of the AGN, for instance in bright Ultra Luminous IR Galaxies (ULIRGs) and in Broad Absorption Line Quasars (BAL-QSOs). This fact lead to the idea that, based on the distance from the central SMBH, the intervening material changes its properties and that there might be a correlation among the various components (Figure 1.3 displays a sketch of how such winds are thought to arise from the inner parts of the accretion disk, Gallagher and Everett, 2007). These winds may well be at the basis of the formulation of how AGN feedback arises, as will be discussed in Section 1.3, where the scientific rational of this Master thesis is presented.

1.2 Gravitational Lensing

The trajectories of photons traveling across the Universe are perturbed by the gravitational fields induced by the matter it contains. Based on the mass and size of the overdensities, we distinguish between weak and strong gravitational lensing effects. The former is caused by the inhomogeneous distribution of matter and produces small distortions, that can be employed to study the large-scale structure of the cosmos. Strong lensing is produced by massive foreground overdensities, such as galaxies and clusters, that create multiple images of a background source, i.e. other galaxies or quasars. Regarding the modeling of how the strong lens affects the source photons, one will distinguish in this case between macro- and micro-lensing effects, where the former is the strong lensing macroscopic effect of producing multiple images and the latter is mostly due to stars and planets of the lens deviating further the light paths. In the next sections I will briefly go through the fundamentals of such modeling, following the review by Treu (2010).

1.2.1 Macrolensing

A gravitational lens system (GLS) can be broken up in three fundamental components: the source plane, the image plane, the observer position. Figure 1.4 shows a sketch of a typical GLS. Let the source position be D_s, the lens position be D_d, and the relative distance be D_{ds}, if the deflector size is small when compared to such lengths, we can assume the lens to be totally contained in the image plane, showing a 2D structure. In the same way, we can consider the source photons as all emitted at the same distance (D_s), therefore from the source plane. These approximations to planar distributions are referred to as the *thin screen approximation*.

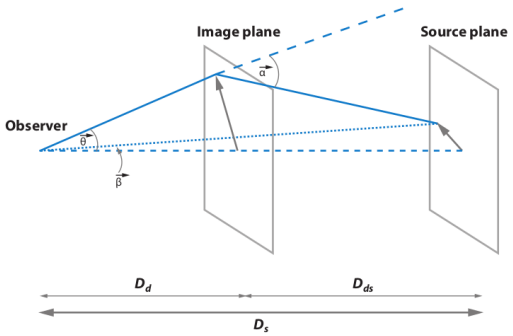

Figure 1.4: Sketch of a gravitational lens system. Credit: Treu (2010).

In absence of the lens, we would observe the source at its intrinsic position $\vec{\beta}$ but, due to the presence of the deflector, the source is actually seen at the apparent position $\vec{\theta}$. Being $\hat{\vec{\alpha}}$ the deflection angle, the relation between

intrinsic and apparent positions is given by the *lens equation*:

$$\vec{\beta} = \vec{\theta} - \vec{\alpha}(\vec{\theta}) \tag{1.11}$$

where $\vec{\alpha}(\vec{\theta})$ is the *reduced deflection angle*:

$$\vec{\alpha}(\vec{\theta}) \equiv \frac{\mathrm{D_{ds}}}{\mathrm{D_s}} \hat{\vec{\alpha}}(\vec{\theta}). \tag{1.12}$$

From the lens equation, it is easy to see that for each $\vec{\theta}$ there can only be one $\vec{\beta}$, thus for a given image the source is uniquely determined, if the lens is known; however, when solving eq. (1.11) for $\vec{\theta}$, the procedure is not so trivial, given that $\hat{\vec{\alpha}}(\vec{\theta})$ is typically a highly non-linear function of $\vec{\theta}$. This implies that more than one solution can be found for $\vec{\theta}$, which means that the source can be lensed into multiple images.

When describing light bending through the general relativity equations and geodesic curves, it turns out that the deflection can be equivalently described by the generalization of the Fermat's principle. It can be demonstrated that the deflection induces a delay in the light travel-time from the source to the observer that depends both on the position $\vec{\theta}$ in the image plane and that in the source plane ($\vec{\beta}$):

$$\Delta \mathrm{t} = \frac{\mathrm{D_d D_s}(1+\mathrm{z_l})}{\mathrm{c D_{ds}}} \left(\frac{1}{2}|\theta - \beta|^2 - \psi(\theta)\right) \tag{1.13}$$

where $\mathrm{z_l}$ indicates the redshift of the lens and $\psi(\theta)$ corresponds to the two-dimensional lensing potential, which satisfies the two-dimensional Poisson equation

$$\nabla^2 \psi = 2\kappa \tag{1.14}$$

where κ is the *convergence*, the deflector's projected surface mass density in units of the critical density Σ:

$$\kappa(\vec{\theta}) \equiv \frac{\Sigma(\vec{\theta})}{\Sigma_{\mathrm{cr}}}, \quad \text{where} \quad \Sigma_{\mathrm{cr}} = \frac{\mathrm{c^2 D_s}}{4\pi \mathrm{G D_d D_{ds}}}. \tag{1.15}$$

A second effect of gravitational lensing is the distorsion of the images, which can be described by the Jacobian matrix A, defined as follows

$$\mathrm{A} \equiv \frac{\partial \vec{\beta}}{\partial \vec{\theta}}; \tag{1.16}$$

it can be demonstrated that its radial and tangential eigenvalues are $\lambda_\mathrm{r} = 1 - \kappa + \gamma$ and $\lambda_\mathrm{t} = 1 - \kappa - \gamma$ respectively, where γ is the *shear* of the lens. The convergence determines the isotropic transformation of the lensed source, while the shear is responsible for anisotropic deformations, stretching the shape of the source along privileged directions (for instance, circular sources can be mapped in elliptical images due to the shear effects).

The third, and final effect, is flux magnification. Gravitational lensing, however, only affects the trajectories of the photons, leaving unchanged both their number and, being an achromatic phenomena, their momenta. These properties translate in the intrinsic conservation of the surface brightness. However, it can be demonstrated that a macro-lensing-induced flux magnification applies and is due to the change in the surface angle subtended by the source. As a result, gravitational lensing acts on the geometry other than on the number or energy of the photons. Let I_ν be the surface brightness in the image plane and $\mathrm{I}^{\mathrm{S}}_\nu$ that in the source plane, the source flux F_ν is given by the following equation

$$\mathrm{F}_\nu = \int_{\mathrm{I}} \mathrm{I}_\nu(\vec{\theta})\mathrm{d}^2\theta = \int_{\mathrm{I}} \mathrm{I}^{\mathrm{S}}_\nu[\vec{\beta}(\vec{\theta})]\mu\mathrm{d}^2\beta \tag{1.17}$$

where μ is the magnification factor which corresponds to the determinant of the coordinate-change matrix between the source and the image planes (the magnification tensor, M) which, in turn, is the inverse matrix of the Jacobian matrix A:

$$\mu = \mathrm{detM} = (\mathrm{detA})^{-1} = \frac{1}{(1-\kappa)^2 - \gamma^2}. \tag{1.18}$$

The ensemble of points where the determinant of the lensing Jacobian vanishes are called *critical lines*. As eq. (1.18) shows, they correspond to formally infinite magnifications, even though the total flux of astrophysical sources with finite sizes is always finite but can be also large (up to ~ 100 or so). The corresponding lines on the source plane are called *caustics*. Sources placed near the location of such lines can be highly magnified.

Another fundamental quantity when describing a GLS is its characteristic angle, the so-called Einstein radius θ_{E}, which for a circular lens corresponds to the region where the average surface-mass density is equal to Σ_{cr}. Its size depends on the properties of the GLS: enclosed mass and redshifts of lens and source. Given a point-like source placed behind the deflector exactly at the center of its mass distribution, it is lensed into the so-called *Einstein ring*, a circle whose radius corresponds to the Einstein radius.

When the lens is extended and multiply-imaging a background source, we refer to the phenomena as macro-lensing. The lens mass distribution defines the actual distance among the images and their multiplicity, for instance the typical separation induced by massive galaxies is of the order of few arcseconds.

1.2.2 Microlensing

When the mass of the lens is small (i.e. from stars to planets), we refer to the phenomena as micro-lensing. At the first order, micro-lenses can be represented as isolated or ensembles of point-masses. Micro-lensing events

can be detected within our Galaxy and in nearby GLS, induced by the stars within the lens.

The relative motion between the source and the lens can induce temporary amplifications of the source flux. Micro-lensing effects can be appreciated, in terms of increment in the source flux, only when the background source is contained within the Einstein ring of the micro-lens. For this reason, one can define the micro-lensing cross section $\sigma_{\rm micro}$ as the solid angle within which the source has to be placed to produce a detectable micro-lensing event. This is equal to the Einstein ring: $\sigma_{\rm micro} = \pi\theta_{\rm E}^2$. The timescale of micro-lensing events is the *Einstein crossing time* $\mathrm{t_E} = \theta_{\rm E}/\mu_{\rm rel}$, where $\mu_{\rm rel}$ expresses the relative motion between the source and the micro-lens, therefore it depends on the geometry of the GLS and the proper motion of the micro-lenses.

In particular, micro-lensing events can be studied through the so-called micro-lensing light curve. These events are extremely hard to model, especially when considering micro-lenses contained in a macro-lens, given the intricate structure of the yielded caustics.

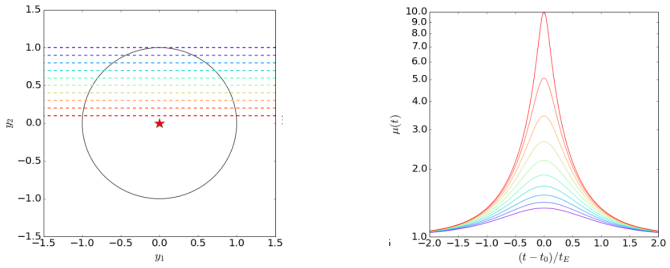

Figure 1.5: *Left panel*: source trajectories projected in the image plane; the different colors correspond to different dimensionless impact parameters (source-lens projected distance in units of the Einstein radius $\theta_{\rm E}$), ranging from 0.1 (red) to 1 (purple). *Right panel*: Micro-lensing light curves color-coded as the trajectories in the left panel, time in given in units of the Einstein crossing time $\mathrm{t_E}$. Credit: Massimo Meneghetti, Gravitational lensing lectures (2017/2018).

To simplify the description of such events, let the lens be stationary and all the motions being ascribed to the background source, even though in reality it happens the other way round; for instance, if we consider a galaxy as macro-lens, micro-lensing perturbations can be induced thanks to the motion of the stars, given the negligible displacement the background source undergoes in the same time. The simplest GLS to describe how a micro-lensing event can occur is that made of a stationary point-mass lens and a point-like background source that moves across the source plane. Figure 1.5 displays the micro-lensing light curves induced by the motion of a source placed at various distances (impact parameter) from the lens. As shown here, the peak of the induced magnification depends on the source-lens

projected distance. The duration of the event is determined by the time the source takes to cross the Einstein ring. Given that gravitational lensing is an achromatic phenomena, wavelength-dependent micro-lensing magnification patterns will be able to tell whether the emission at the varying energy is coming from regions of different sizes.

This example gives a qualitative idea of how a micro-lensing event can be generated. In reality, we parameterize such events through the source crossing time; based on the structure of the GLS, such time ranges between few months and years for extra-galactic sources, while among our Galaxy it is typically of the order of a few days.

1.3 Scientific rationale

Given the scaling relations seen in AGN where the SMBH mass and the properties of the AGN host galaxy bulge (i.e., the "$M_{BH} - \sigma$" relation, Kormendy and Richstone, 1995; Magorrian et al., 1998), AGN are thought to play a significant role in their host galaxy evolution. This role is considered to be so crucial that we refer to these phenomena as the cosmic cycle of galaxy and AGN co-evolution (Hopkins et al., 2006). Despite its importance, however, the characterization of such process is still an open issue. One way the co-evolution could take place is in the case of powerful winds generated by the AGN, resulting in massive gas outflows. In this scenario, the AGN activity could end up expelling all the ISM and quench the star formation. These outflowing winds have been observed at many wavelengths, from sub–mm and IR to X-rays, thus implying different gas phases, from molecular to highly ionized, which show very different outflow velocities and spatial distributions. Fiore et al. (2017) recently searched for scaling relations between the properties of massive AGN winds from sub-pc to kpc scales. Given that many of these winds were detected in different sources, they mostly concentrated on searching scaling relations dividing the sample in base of the wind gas phase. However, for a few sources (i.e. IRASF 11119+3257, Tombesi et al. (2015); Mrk 231, Feruglio et al. (2015); APM08279, Feruglio et al. (2017)), the detection of outflows components at different wavelengths allowed to investigate the relations among the various gas phases (namely molecular and X-ray winds), whose momentum flux and the outflow velocity were found to correlate. This is consistent with the scenario of a unique wind accelerated by the same engine that expands across the galaxy and affects its evolution both compressing (positive feedback) and quenching (negative feedback) its star formation, through the sweeping out the gas (King and Pounds, 2015). However, this is possible only if the winds are accelerated by the central source at sufficient speed (nominally, semi-relativistic velocities).

As mentioned above, X-rays allow us to investigate the physical phenomena related to the innermost regions of the accretion disk (sub-pc scales),

hence those where the highest velocity outflows likely originate. Outflows detected at these wavelengths are divided in Warm Absorbers (WAs; $v_{out} \sim$ few $\cdot$ 1000 km/s, Reynolds and Fabian, 1995; Blustin et al., 2005) and Ultra-Fast Outflows (UFOs; Tombesi et al., 2010). The first typically produce broad absorption features in the soft X-ray continuum, while the latter are (semi)relativistic winds (v_{out} up to 0.2–0.3c), which manifest themselves as blueshifted resonant absorption features in the FeK band, at energies above 7 keV. The mechanical power they generate could in principle eject/compress huge amounts of gas to an extent actually relevant in the galaxy global evolution (Fabian, 2012; King and Pounds, 2015). The number of extreme outflow components detected in X-ray spectra has increased in recent years, both for Seyfert galaxies and quasars. These detections have brought up the idea that these winds might well be common, although probably episodic, since they appear to be detected only intermittently. The two gas phases described above seem to be one the natural evolution of the other, with UFOs originating closer to the BH with more extreme properties, i.e. column densities and ionization ($\log(N_H/cm^{-2}) \simeq 22-24$, $\log[\xi/(\text{erg s}^{-1}\text{cm})] \simeq 3-6$), to be compared with the less extreme values ($\log(N_H/cm^{-2}) \simeq 20-22$, $\log[\xi/(\text{erg s}^{-1}\text{cm})] < 3$) of WAs.

To investigate the way the SMBH-bulge scaling relations formed and the role of AGN in their host galaxy formation and evolution, it is mandatory to search for bright sources at high redshifts, in order to properly model the wind features (if present). Given the Madau plot (Madau et al., 1996), one knows that the cosmic star formation density peaks at $z \simeq 2$, where also the AGN activity peaks. Therefore, one would expect the feedback processes to be most important and, possibly, more easily visible around this cosmic epoch. The best candidates for this kind of studies are thus high-redshift quasars, since they represent the AGN with the highest luminosity. With current technology, studying such distant sources in the X-ray band and collecting one good SNR spectra is a challenge. We have thus selected for this thesis a lensed high-redshift QSO for which the flux amplification induced by the lens offers a unique tool to observe it in a sustainable amount of time with high counting statistics.

1.3.1 The case of the Einstein Cross

Discovered by Huchra (Huchra et al., 1985), Q2237+0305 (the Einstein Cross) is a radio-quiet quasar at $z_Q = 1.695$, quadruply–imaged by a spiral galaxy at $z_L = 0.0395$. Figure 1.6 shows the optical image taken by Hubble Space Telescope (HST).
The individual images are arranged in a ringlike formation. It was the sixth gravitational lens system to be discovered and the first nearby ($z_L < 0.1$) ever detected; given its proximity, it has been studied both for its macro- and micro-lensing properties. From theoretical modelings of the system as

Figure 1.6: HST image of the Einstein Cross. The four images are resolved (A, B, C, D from upper left and clockwise); the central source corresponds to the lensing galaxy. Credit: https://www.spacetelescope.org/images/potw1204a/.

an elliptic lens (Schmidt et al., 1998; Wertz and Surdej, 2014) and observational constrains (Dai et al., 2003), the time delays between the four images have been found to be less than a day ($\Delta t_{AC} \approx -16$hrs, $\Delta t_{AD} \approx -5$hrs, $\Delta t_{AB} \approx 2$hrs) and the total magnification to be $\mu \approx 16$ (Schmidt et al., 1998). From the Hβ emission line, the BH mass was constrained to be $\log M_{BH} = 9.08 \pm 0.39$ $M_\odot$ (Assef et al., 2011), which implies a gravitational radius (see eq. (1.8)) of $R_g \simeq 1.8 \times 10^{14}$ cm.

The Einstein Cross was detected for the first time in the X-ray band in 1997 by ROSAT/HRI (Wambsganss et al., 1999), but it could be resolved in its four images only after the advent of facilities with much higher angular resolution. In particular, after *Chandra*, the scientific community mostly focused on X-ray monitoring campaigns to study the micro-lensing variability of this system, which was also used as a tool to investigate the size of its innermost regions (Dai et al., 2003; Mosquera et al., 2013; Guerras et al., 2017). Several works have been published on the *Chandra* spectral properties of its different image components (Dai et al., 2003; Reynolds et al., 2014; Chen et al., 2012) and one XMM-*Newton* spectrum (Fedorova et al., 2008). Nevertheless, there is still no comprehensive analysis of all the *Chandra* and XMM-*Newton* available spectra.

The average properties of UFOs are known at low redshift, while at $z \geq 1.5$ there are only few detections. Q2237+030 is part of a sample of distant AGN that has been built in order to investigate the origin of outflows in the X-ray band near the Cosmic Noon. Almost all the UFOs detections at $z > 0.1$ are found in gravitationally lensed objects, for instance APM 08279+5255, PG1115+080, H1413+117, HS 0810+2554, MG J0414+0534 (Hasinger et al., 2002; Chartas et al., 2003; Chartas, Brandt, Gallagher and Proga, 2007; Chartas, Eracleous, Dai, Agol and Gallagher, 2007; Chartas et al., 2009, 2016; Dadina et al., 2018). To our knowledge thus far the only exceptions are two bright unlensed distant sources, PID352 (Vignali et al., 2015) and HS 1700+6416 (Lanzuisi et al., 2012). This fact highlights how important the induced magnification is to perform this kind of studies on distant sources. The sample comprising about ten gravitationally lensed

quasars, all at $z \geq 1.5$, summed to other non-lensed high-flux quasars at high redshift (part of a XMM-*Newton* AO16 large program – PI: M. Cappi) would allow statistical studies on their X-ray properties at the peak of the SMBH accretion and cosmic star formation.

Chapter 2

X-ray telescopes: Chandra and XMM-Newton

Just before the beginning of the new millennium, NASA and ESA launched two X-ray telescopes, respectively *Chandra* X-ray Observatory and X-ray Multi-Mirror Mission (XMM-*Newton*), that revolutionized the X-ray astronomy. As I will explain in the next paragraphs, being the expression of two different observational strategies, *Chandra* and XMM-*Newton* properties are rather complementary. NASA focused on building an X-ray imaging system, reaching an unprecedented angular resolution through four high performing mirrors, while ESA aimed at extreme good quality X-ray spectra, through a large effective area, using three identical modules of 58 shells. Given their remarkable characteristics and the complementary good-quality data that the two telescopes are able to provide, it is common to refer to this era as the Golden Age of the X-ray Astronomy.

2.1 The fundamental parameters of X-ray telescopes

X-ray photons are very energetic (E > 100 eV) and require special techniques to be detected. X-ray telescopes can either be collimating or focusing systems; the latter typology, gathering all the signal in a much smaller area, requests smaller detectors, grant better signal-to-noise ratio and achieve lower flux limit. High-energy radiation is hard to reflect or refract because very penetrating into matter; therefore, grazing reflection is necessary, for which an incidence angle smaller than the so-called critical reflection angle θ_c is required. Given a material of density ρ and a photon of energy E, it can be demonstrated that θ_c is proportional to the ratio: $\theta_c \propto \sqrt{\rho}/\mathrm{E}$. From this relation one infers that the more energetic the photon is, the smaller θ_c gets, which makes total reflection harder to achieve. The best performing optics

configuration is the so called Wolter Type–1 (Wolter, 1952): co-axial and co-focal parabolic and hyperbolic mirrors, which focus the radiation through double-grazing reflection (Fig. 2.1).

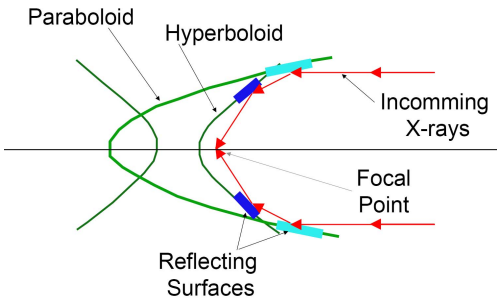

Figure 2.1: Wolter Type-1 optics configuration. Credit: NASA.

Given the relation between θ_c and the photon energy, telescopes with nested mirrors cover a wider range of incidence angles, thus energies, and present larger sensitive areas. The same relation suggests that heavier materials manage to reflect higher energy photons, which is why the mirrors are usually coated with high-Z elements. Current technology allows grazing telescopes to deflect radiation up to ∼80 keV; this limit is achieved by the telescope *NuSTAR* thanks to its multi-layer coating optics, which employ interference between the layers to reflect high-energy photons.
The optics are usually paired to CCD (Charge Coupled Devices) detectors, which allow decent quality spectroscopy and direct imaging at the same time, and grant a significant quantum efficiency ($> 90\%$).
The response of an X-ray telescope is called effective area (A_{eff}, $[cm^2]$), which depends on the energy and the incidence angle (E, θ) of the incoming photon and the position on the focal plane (x,y) as follows:

$$A_{eff}(E, \theta, x, y) = A_{geom} * R(E) * V(E, \theta) * QE(E, x, y) \tag{2.1}$$

- A_{geom} corresponds to the optics cross section at the conjunction of the two types of mirrors;
- R(E) is the reflectivity of the mirrors, which decreases as the incident photon energy increases;
- $V(E, \theta)$ is the vignetting factor (ratio of the off-axis and on-axis counts at different energies and off–axis angles); it accounts for the loss of signal as the energy and the incidence angle increase;
- $QE(E, x, y)$ is the quantum efficiency of the detector, which depends both on the incoming radiation energy and the position on the focal plane.

Another fundamental parameter is the PSF (Point Spread Function), which describes the distribution of a point-like source photons on the focal plane; it is usually measured through its on-axis FWHM (Full Width at Half Maximum) and degrades moving to off-axis positions. It can be visualized in 2D by the so-called encircled energy fraction, which returns the extraction radius needed to have a certain percentage of counts at a given energy; its HEW (Half Energy Width) is equivalent to the PSF FWHM, since it represents the PSF width at 50% of the total energy.
The X-ray energy resolution ΔE is expressed as follows:

$$\frac{\Delta E_{[keV]}(FWHM)}{E_{[keV]}} \propto E_{[keV]}^{-1/2} \tag{2.2}$$

The typical resolution for CCD spectroscopy is ~ 150 eV at $E = 6.4$ keV (the rest-frame energy of the iron Kα line); this can be also expressed through its reciprocal, the resolving power $E/\Delta E$, whose typical values for X-ray CCD spectroscopy are $E/\Delta E \simeq 20 - 50$. The performances of a telescope are defined by its sensitivity, which corresponds to the minimum flux it can detect, while the Signal-to-Noise Ratio (SNR) is a crucial parameter for each observation:

$$\frac{S}{N} = \frac{C_S}{\sqrt{{\sigma_S}^2 + {\sigma_B}^2}} = \frac{C_S}{\sqrt{C_S + C_B}} \tag{2.3}$$

where C_S = source net counts, C_B = background counts and σ_S, σ_B the respective Poisson distribution uncertainties. From its definition (eq. 2.3) it is easy to see that to improve the SNR one has two possibilities:

- increasing the collected signal (i.e. using a higher effective area);
- limiting the "impact" of the background (i.e. improving the spatial resolution[1]),

which correspond to the different philosophies applied by NASA and ESA, as mentioned above.

2.2 The Chandra X-ray Observatory

Launched and deployed by Space Shuttle Columbia on July 23, 1999, *Chandra* X-ray Observatory provides the highest angular resolution ever reached for X-ray telescopes (on-axis PSF FWHM $\simeq 0.5''$, see Fig. 2.2). This is achieved thanks to its highly performing optics (HRMA, High Resolution Mirror Assembly), four iridium shells arranged in a Wolter Type–1 setup, which make *Chandra* the perfect instrument for deep X-ray

[1] A sharper PSF allows to focus the point-like objects on smaller areas, which means that background objects have a limited impact since their contribution is more confined.

surveys (for instance, the *Chandra* Deep Fields). Given the restrictions to the payload of a space mission and the weight of each mirror, the price of such a sharp on-axis PSF is to be found in the number of mirrors that can be nested, thus in its effective area A_{eff}. In particular, having so few shells, the inner parts of the telescope are deprived of mirrors, thus shallower incidence angles are less covered. This makes hard X-ray photons difficult to reflect; in fact, *Chandra* effective area is always lower than that of XMM-*Newton* at all energies, and this difference is at its maximum in the hard band (as shown in Fig. 2.3). Furthermore, *Chandra* effective area is now significantly degraded since its launch, especially in the soft band due to the buildup of molecular contamination on the ACIS filters: for instance, the effective area at 1 keV was $A_{eff}^{[1.0keV]} = 600$ cm^2 at the launch and its predicted value for cycle 21 is $A_{eff}^{[1.0keV]} \gtrsim 100$ cm^2. Figure 2.2 (right panel) shows the comparison between cycle 3 and cycle 21 ACIS-S effective areas.

Chandra's main science instrument, positioned on the focal plane, is ACIS (Advanced CCD Imaging Spectrometer, Figure 2.4), which is composed of ten 1024×1024 pixel CCDs arranged as follows:

- ACIS–I → four CCDs in a 2x2 array configuration, 16.9 by 16.9 arcmin;
- ACIS–S → six CCDs in line (1x6 array), 8.3 by 50.6 arcmin.

Each combination of up to six CCDs can be chosen when programming an observation. Figure 2.5 shows the energy resolution of ACIS-S back illuminated CCDs (S1, S3) separately and the mean resolution referred to all the CCDs, which are front illuminated. Depending on the configuration, the characteristics change; in general, the mean energy resolution is ~ 100 eV at 1 keV and ~ 150 eV at 5.9 keV. ACIS–I is preferred for imaging; given its squared shape, the offset from the CCD array center is typically lower than the one in ACIS–S, granting a better off-axis PSF.
Chandra is also provided of other three science instruments:

- High Resolution Camera (HRC) – It offers the highest spatial ($< 0.5''$) and temporal (16 msec) resolution. The HRC-I has the largest Field of View (FoV, 31x31 arc minutes);
- High Energy Transmission Grating (HETG) – It is most commonly used with ACIS-S for bright sources over the $0.4 - 10$ keV energy band. The resolving power ($E/\Delta E$) varies from ∼800 at 1.5 keV to ∼200 at 6 keV;
- Low Energy Transmission Grating (LETG) – It provides the highest spectral resolving power ($E/\Delta E > 1000$) at low energies (0.07 – 0.2 keV) on *Chandra*, thus it is commonly paired to the HRC-S to observe bright soft sources.

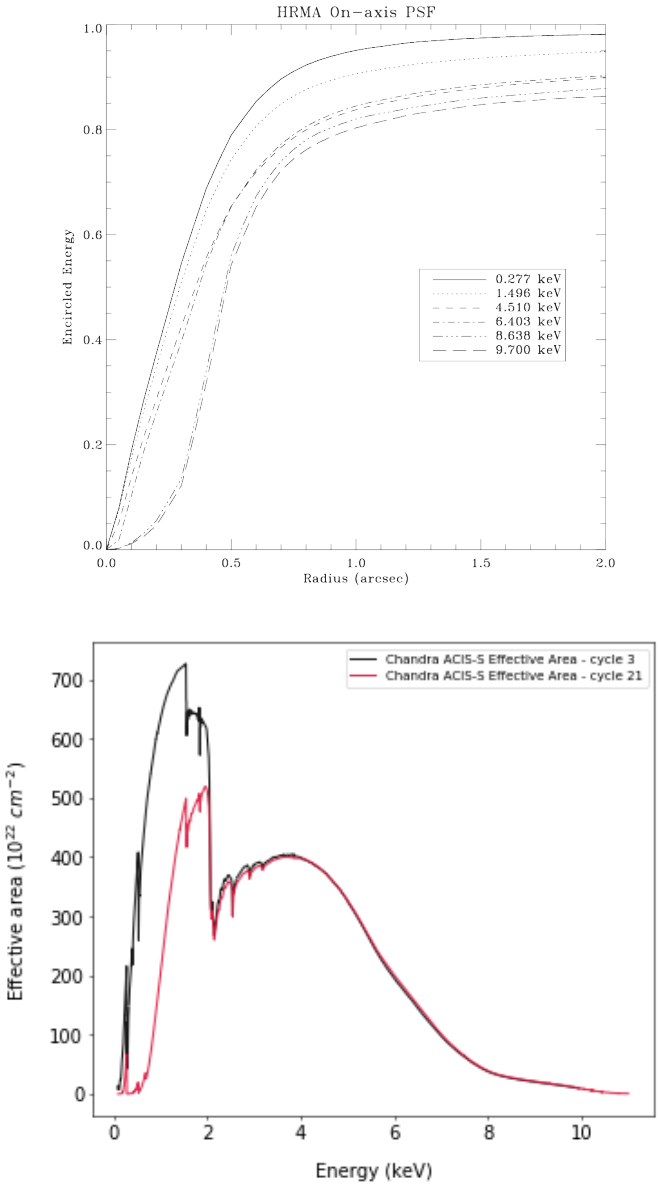

Figure 2.2: *Top panel*: *Chandra*'s HRMA on–axis PSF. The plot shows the encircled energy fraction as a function of the spectral extraction radius at a given energy; for instance, at ∼1.4 keV, the 80% encircled energy fraction is achieved with a radius of $\sim 0.5''$, while at ∼6.4 keV a radius of $\gtrsim 0.8''$ is required. The curves are calculated integrating the PSF. Credit: The *Chandra* Proposers' Observatory Guide. *Bottom panel*: Comparison between *Chandra* ACIS-S effective area for cycle 3 (black) and cycle 21 (red). Credit: The *Chandra* Main Proposer Page.

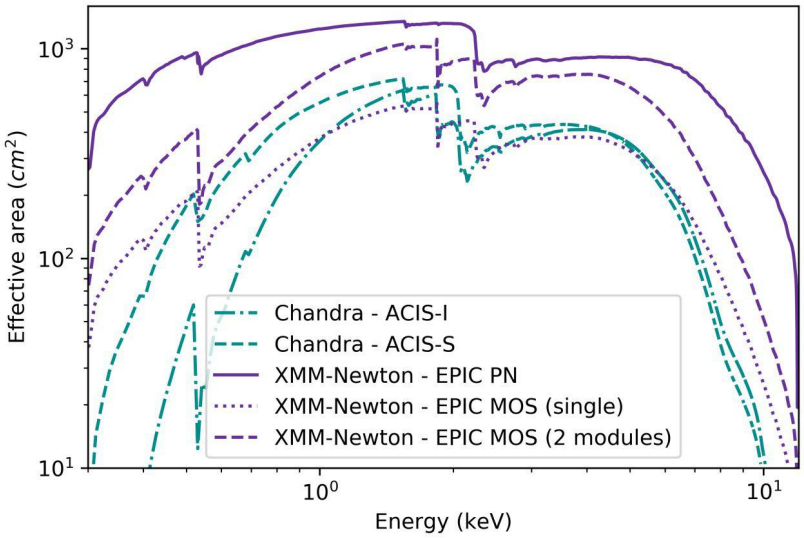

Figure 2.3: Comparison of *Chandra* (blue) and XMM-*Newton* (purple) effective areas of the CCD instruments. Credit: Deborah Costanzo's Master's thesis.

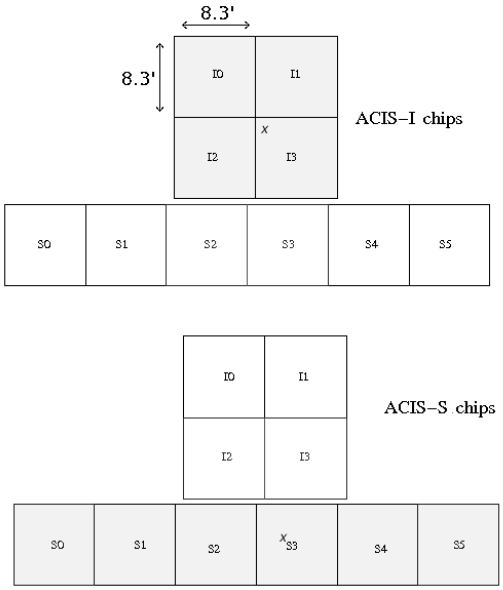

Figure 2.4: Scheme of *Chandra*'s focal plane. The crosses (CCD I3, S3) show the default aimpoints of ACIS-I and ACIS-S. Credit: The *Chandra* Proposers' Observatory Guide.

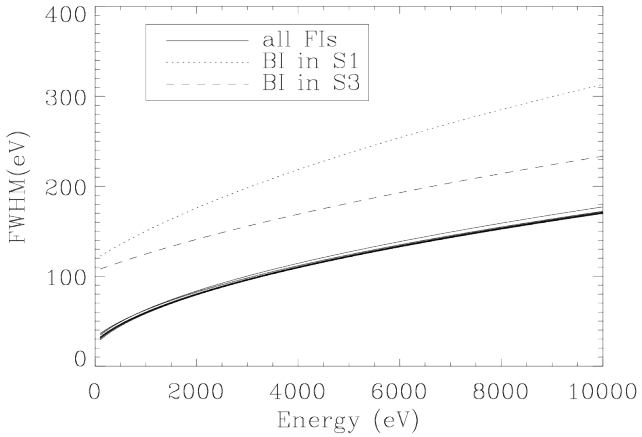

Figure 2.5: *Chandra* ACIS energy resolution. The dashed and the dotted lines are referred to the two back illuminated CCDs of ACIS-S, the solid line to all the other CCDs, which are front illuminated. Credit: The *Chandra* Proposers' Observatory Guide.

2.3 XMM-Newton

While *Chandra*'s main property resides in its PSF and imaging capabilities, XMM-*Newton*, launched on December 10th, 1999 by an Ariane 504, grants an unprecedented effective area, thus high statistics CCD spectroscopy. This is achieved thanks to its Wolter Type-1 optics and science instruments. Furthermore, it is the first system to allow both X-ray and optical imaging, thanks to the UV camera installed onboard. The X-ray telescope comprises three identical modules, each made of 58 nested gold-coated shells; in Figure 2.6 the light path of each module is shown. These provide an on-axis PSF FWHM of $\sim 6''$ and HEW of $\sim 15''$ (Fig. 2.7).

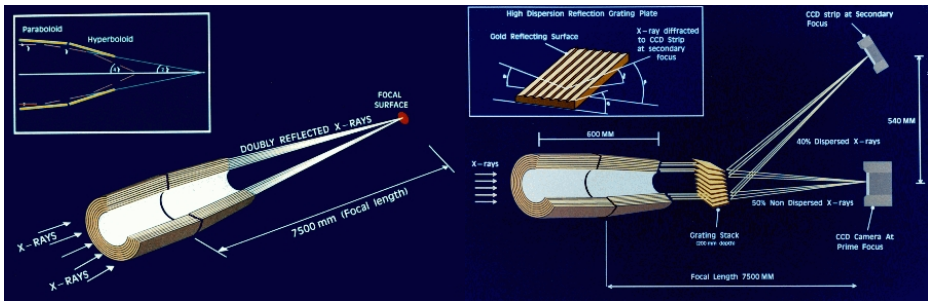

Figure 2.6: XMM-*Newton* light paths; on the left, EPIC-pn light path, on the right EPIC-MOS and EPIC-RGS light paths. Credit: ESA's XMM-*Newton* Users Handbook.

XMM science instruments are the European Photon Imaging Camera

(EPIC), the Reflection Grating Spectrometer (RGS) and the Optical Monitor (OM, paired to the optical/UV camera). The first is composed of three CCDs: pn, MOS1 and MOS2. The strength of XMM design resides in the fact that each of these CCDs is paired to its own module, which allows all the three to work simultaneously and autonomously. They offer the typical resolving power of CCDs ($E/\Delta E \simeq 20 - 50$) and operate in the 0.3 - 10 keV band.The RGS are two excellent quality spectrometers ($E/\Delta E \simeq 200 - 800$), but their energy range is limited to the soft band ($E = 0.3 - 2.5$ keV). They are mounted on the same modules as the MOS cameras; a grating, the RGA, splits almost equally the incoming photons (∼44% to the MOS, ∼40% to the RGS) between the two systems. The EPIC cameras are those that offer the best effective area; as shown in Fig. 2.3, EPIC-pn is the one with the best response, higher than that of *Chandra* and even than the MOS summed together; at ~ 1 keV, for instance, $A_{\rm eff}^{\rm pn} \gtrsim 1000$ cm^2 while $A_{\rm eff}^{\rm MOS} \simeq 800$ cm^2 and $A_{\rm eff}^{Chandra} \simeq 600$ cm^2. This is ascribed to the fact that EPIC-MOS share the incoming radiation with the RGS.

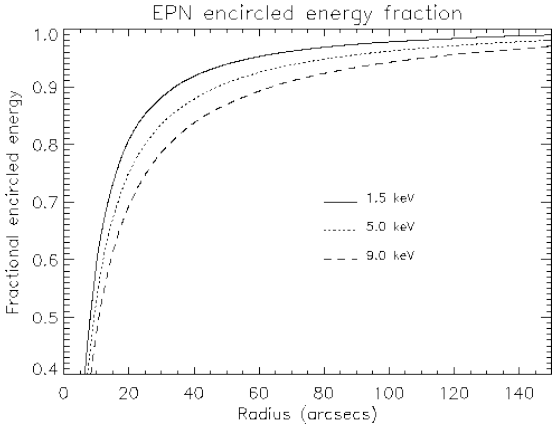

Figure 2.7: XMM-*Netwon* EPIC-pn on–axis encircled energy fraction as a function of the spectral extraction radius at a given energy. Credit: ESA's XMM-*Newton* Users Handbook.

On the one hand, thanks to its sharp PSF, *Chandra* is the ideal instrument to reach lower flux limits and very good sensitivities, as well as when interested in imaging. On the other hand, XMM-*Newton* is the best X-ray telescope when seeking high-statistics spectroscopy data of medium-high flux sources, for instance to study the physics of the target in detail. Combining data from both telescopes allows a more thorough analysis of objects at low and intermediate ($z \sim 2$) redshifts, therefore it is common to propose for observing time with both XMM-*Newton* and *Chandra*. The use and combination of the two telescopes' performances is precisely the approach I have been using in this work, as I will explain in the next chapters.

Chapter 3

The Chandra view of the Einstein Cross

The Einstein Cross has been pointed several times by *Chandra* in the last 20 years. The main purpose of these observations was to use the micro-lensing effects to infer the dimensions of the X-ray emitting region (Dai et al., 2003; Mosquera et al., 2013; Guerras et al., 2017); given its spatial resolution, *Chandra* is the only X-ray Observatory that allows this kind of studies, since they are based on measuring the flux from the individual images. In fact, micro-lensing induced variability produced by the caustic crossing can be inferred from the flux ratios of the individual image components.

I analyzed all the available public observations of the *Chandra* Data Archive as of October 2018, for a total of thirty-five data set. Their properties are summarized in Table 3.1; the observation exposure times vary from few ks to ∼33 ks (Fig. 3.1), and the observations span over sixteen years (∼ 5.9 yr in the source rest frame). The quasar was observed by ACIS–S each time, which means that its signal is gathered by the ACIS-S3 CCD in every observation.

3.1 Data reduction and spectra extraction

Even though the available public data have already been processed through *Chandra* standard pipeline, reducing the raw data was deemed necessary in order to uniformly apply the most up-to-date calibration to all of them (the earliest observation was performed in 2000). In the reduction procedure, the data are calibrated, bad and warm pixels are flagged, the events are filtered in grade[1], Good Time Intervals (GTI) and eventually energy. I re-processed all the *Chandra* observations through the CIAO 4.9 software tool

[1]The event grade corresponds to the pixel pattern produced by the incoming photon. Depending on how many pixels the event "lights up", it is assigned a grade which helps distinguishing between good and bad events.

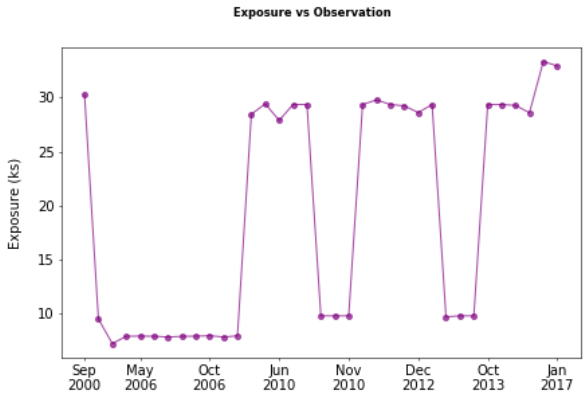

Figure 3.1: Variation of the exposure time in the *Chandra* observations of Q2237+030.

`chandra_repro`[2], which is a script that automates all the above mentioned operations.

Given the superb PSF that *Chandra* offers, it manages to resolve the four images (named A, B, C, D as in Figure 3.2) of the Einstein Cross, which allows the extraction of individual image spectra. To this goal, one has to select the source region and the background region (or regions), not necessarily of the same size, but of a radius that leads to at least 80% of the encircled energy (for the source) in order to properly sample the PSF; regarding *Chandra*, this means an extraction radius larger than 0.5″ (see Fig. 2.2). The background region is used to produce the mean background spectrum, while the total spectrum (source+background) is extracted from the source region; when analyzing the spectra, both information is needed to obtain the net source contribution.

To consistently analyze the data, I adopted the same extraction regions for all the dataset. I used the source position in observation 431 to select the image regions, since it has one of the deepest exposure. I saved them in (Ra, Dec) and then uploaded those regions over each observation raw image to check whether they actually corresponded to the quasar position; this is necessary due to possible astrometric differences among the various datasets, even though they are usually quite limited in *Chandra* data (`http://cxc.harvard.edu/cal/ASPECT/celmon/`). In a few cases (ObsIDs: 6831, 11534, 11535, 11538, 13960, 14515, 16316, 16317) the images are a bit shifted with respect to the extraction regions, while in three observations (ObsIDs: 14513, 14517, 18804) they are significantly shifted. To solve the problem, I shifted the extraction regions by a maximum value of 1 arcsec for all observations mentioned above, without varying the spacing and their sizes.
Figure 3.3 shows, for instance, how I shifted the extraction regions in the

[2]When running `chandra_repro`, I set `check_vf_pha=yes` for all observations except for 431 and 1632 which were taken in faint datamode.

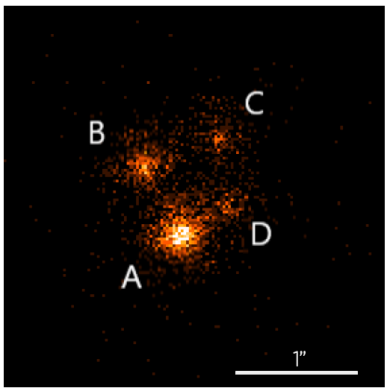

Figure 3.2: Raw image of Q2237+030 (ObsID 431) binned with a binsize of 0.1". The images are named as A, B, C, and D, clockwise, starting from bottom left. Given the quasar redshift ($z_Q = 1.695$), 1" separation corresponds to a distance of 8.68kpc (cosmology values: $H_0 = 70.0$ km/s/Mpc, $\Lambda_0 = 0.73$).

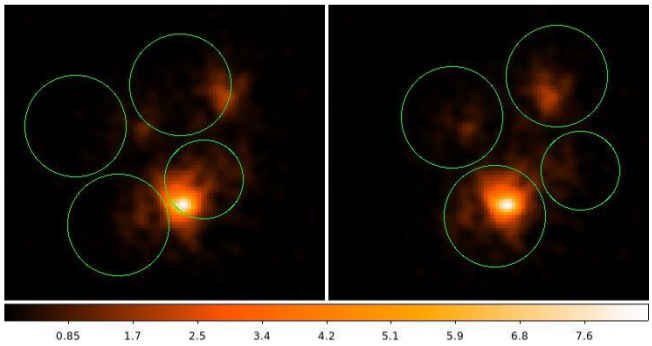

Figure 3.3: Raw images of observation 18804 (both binned with a binsize of 0.1" and smoothed using a Gaussian filter with $2\sigma = 3$ pix) with the individual spectral extraction regions before (left) and after (right) the shifting. The circles for images A, B, C have a radius of $0.8''$, the circles for image D $0.6''$.

case of observation 18804, while in Figure 3.4 one can see the comparison between the raw images of the first and the last observations (ObsIDs 431 vs. 19639) as an example of those that did not require any shift. The regions were selected with a little offset from the image centroid in order to reduce the contamination from their neighbours. The radius for images A, B, and C is $0.8''$, while for image D it is $0.6''$, which leads to an encircled energy fraction of about 90% and 80% (see Fig. 2.2), respectively.

The background extraction region has to be placed near the target in order to be representative of its actual background, but also not too close to prevent contamination by the source itself. I selected it as a circular region of 50" in the same CCD chip as the target (the offset between its center and the quasar is of approximately 1 arcmin), checking for each observation that

it contained no bright field objects.
The CIAO tool that, given the extraction region as input, returns the spectrum is `specextract`; other than that, it produces the Redistribution Matrix File (RMF, channel-energy conversion) and the Ancillary Response Matrix (ARF, combination of the telescope's effective area and the detector's quantum efficiency), which, respectively, are necessary for the energy calibration and to unfold the data for the telescope effective area (see Chapter 2). Since some of the images are very faint, all the spectra were first extracted binning at one count per energy bin and applying the C-Statistics (Cash, 1979) during the analysis. In Table 3.1 the total source net counts and the count rate of each image spectra are reported; those showing over 500 counts are in bold and were then grouped at 20 counts per bin at least and analyzed applying the χ^2 statistics. From now on, I will be referring to these as the high-statistics sample. Remarkably, the background counts in the source extraction regions are almost negligible, which means that the source net counts are essentially equal to the total counts (when rounding to the closest integer). The counts errors in Table 3.1 are calculated as the square root of the source counts, as they follow the Poisson distribution, and the same for the count rate errors.

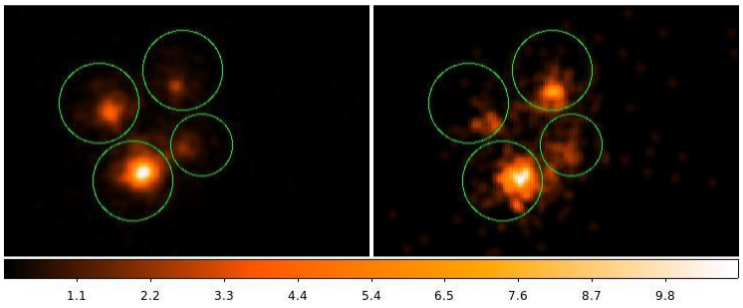

Figure 3.4: Raw images of observation 431 on the left and observation 19639 on the right (both binned with a binsize of 0.1" and smoothed using a Gaussian filter with $2\sigma = 3$ pix) with the individual spectra extraction regions. The circles for images A, B, C have a radius of $0.8''$, the circles for image D $0.6''$.

Table 3.1: List of the information of each *Chandra* observation and details of the individual image spectra. Those with more than 500 counts are reported in bold (the high-statistics sample). The source net counts are referred to the 0.4-7.0 keV observed energy band and so are the count rates. The observations are listed for increasing ObsID.

ObsID	Date	Exp. (ks)	Image	Net Counts	CR (10^{-3} cts/s)
431	2000-09-06	30.29	**A**	**1272±36**	41.99±1.18
			B	**523±23**	17.26±0.26

Continues on next page

Table 3.1 – continued from previous page

ObsID	Date	Exp. (ks)	Image	Net Counts	CR (10^{-3} cts/s)
			C	233±15	7.69±0.50
			D	177±13	5.84±0.44
1632	2001-12-12	9.54	A	309±18	32.39±1.84
			B	99±10	10.38±1.04
			C	51±7	5.34±0.75
			D	52±7	5.45±0.76
6831	2006-01-09	7.27	A	97±10	13.35±1.36
			B	26±5	3.57±0.70
			C	86±9	11.83±1.28
			D	35±6	4.82±0.81
6832	2006-05-01	7.94	A	211±15	26.58±1.83
			B	90±10	11.34±1.19
			C	111±11	13.98±1.33
			D	58±8	7.31±0.96
6833	2006-05-27	7.95	A	118±11	14.83±1.37
			B	54±7	6.79±0.92
			C	56±7	7.04±0.94
			D	21±5	2.64 ±0.58
6834	2006-06-25	7.94	A	272±16	34.26±2.07
			B	74±9	9.32±1.08
			C	111±11	13.98±1.33
			D	54±7	6.80±0.93
6835	2006-07-21	7.87	A	319±18	40.52±2.27
			B	64±8	8.13±1.02
			C	79±9	10.03±1.13
			D	49±7	6.22±0.89
6836	2006-08-17	7.93	A	170±13	21.43±1.64
			B	60±8	7.56±0.98
			C	62±8	7.82±0.99
			D	40±6	5.04±0.80
6837	2006-09-16	7.95	A	166±13	20.89±1.62
			B	39±6	4.91±0.79
			C	62±8	7.80±0.99
			D	35±6	4.40±0.74
6838	2006-10-09	7.99	A	157±13	19.65±1.57
			B	51±7	6.38±0.89
			C	53±7	6.63±0.91
			D	34±6	4.26±0.73
6839	2006-11-29	7.87	**A**	**538±23**	68.32±2.95
			B	108±10	13.71± 1.32

Continues on next page

Table 3.1 – continued from previous page

ObsID	Date	Exp. (ks)	Image	Net Counts	CR (10^{-3} cts/s)
			C	189±14	24.00± 1.75
			D	113±11	14.35± 1.35
6840	2007-01-14	7.98	A	441±21	55.29±2.63
			B	118±11	14.79±1.36
			C	132±11	16.55±1.44
			D	84±9	10.53±1.15
11534	2009-12-31	28.46	**A**	**1756±42**	61.70±1.47
			B	164±13	5.76±0.45
			C	454±21	15.95±0.75
			D	**802±28**	28.18±1.00
11535	2010-04-25	29.43	A	377±19	12.81±0.66
			B	52±7	1.76±0.25
			C	101±10	3.43±0.34
			D	150±12	5.10±0.42
11536	2010-06-27	27.89	A	342±19	12.26±0.66
			B	44±7	1.57±0.24
			C	105±10	3.76±0.37
			D	163±13	5.84±0.46
11537	2010-08-07	29.36	A	228±15	7.76±0.51
			B	44±7	1.50±0.23
			C	68±8	2.31±0.28
			D	116±11	3.95±0.37
11538	2010-10-02	29.36	**A**	**501±22**	17.06±0.76
			B	49±7	1.67±0.24
			C	154±12	5.22±0.42
			D	423±21	14.41±0.70
11539	2010-11-23	9.83	A	93±10	9.46±0.98
			B	13±4	1.32±0.37
			C	31±6	3.15±0.57
			D	40±6	4.09±0.64
13191	2010-11-27	9.83	A	82±9	8.34±0.92
			B	9±3	0.91±0.31
			C	19±4	1.93±0.44
			D	29±5	2.95±0.55
13195	2010-11-26	9.83	A	91±10	9.25±0.97
			B	10±3	1.01±0.32
			C	23±5	2.34±0.49
			D	27±5	2.74±0.53
12831	2011-05-14	29.36	**A**	**2677±52**	91.19±1.76
			B	215±15	7.32±0.50

Continues on next page

Table 3.1 – continued from previous page

ObsID	Date	Exp. (ks)	Image	Net Counts	CR (10^{-3} cts/s)
			C	**575±24**	19.58±0.82
			D	429±21	14.61±0.71
12382	2011-12-27	29.79	A	343±19	11.51±0.62
			B	59±8	1.98±0.26
			C	128±11	4.29±0.38
			D	100±10	3.36±0.34
13960	2012-01-09	29.36	A	308±18	10.49±0.60
			B	52±7	1.77±0.25
			C	122±11	4.15±0.38
			D	117±11	3.98±0.37
13961	2012-08-02	29.24	**A**	**906±30**	30.98±0.10
			B	213±15	7.28±0.50
			C	244±16	8.34±0.53
			D	202±14	6.91±0.49
14513	2012-12-26	28.62	**A**	**684±26**	23.89±0.91
			B	339±18	11.84±0.64
			C	247±16	8.26±0.55
			D	260±16	9.08±0.56
14514	2013-01-05	29.36	**A**	**622±26**	21.18±0.85
			B	298±17	10.15±0.59
			C	215±15	7.32±0.50
			D	268±16	9.13±0.56
14515	2013-08-31	9.73	A	164±22	16.85±1.32
			B	62±8	6.37±0.81
			C	57±8	5.86±0.78
			D	30±5	3.08±0.56
16316	2013-08-26	9.83	A	120±11	12.21±1.11
			B	47±7	4.78±0.70
			C	44±7	4.48±0.68
			D	30±5	3.05±0.56
16317	2013-08-28	9.83	A	105±10	10.68±1.04
			B	45±7	4.58±0.68
			C	43±7	4.37±0.67
			D	24±5	2.44±0.50
14516	2013-10-01	29.35	A	230±15	7.83±0.52
			B	70±8	2.38±0.29
			C	122±11	4.15±0.38
			D	96±10	3.27±0.33
14517	2014-05-14	29.36	**A**	**1071±33**	36.48±1.11
			B	322±18	10.97±0.61

Continues on next page

Table 3.1 – continued from previous page

ObsID	Date	Exp. (ks)	Image	Net Counts	CR (10^{-3} cts/s)
			C	384±20	13.08±0.67
			D	156±12	5.31±0.43
14518	2014-06-08	29.28	**A**	**628±25**	21.45±0.86
			B	206±14	7.03±0.49
			C	263±16	8.98±0.55
			D	117±11	3.99±0.37
18804	2016-04-24	28.60	**A**	**1009±32**	35.28±1.11
			B	132±11	4.61±0.40
			C	269±16	9.40±0.57
			D	126±11	4.41±0.39
19638	2016-12-22	33.34	A	302±17	9.05±0.52
			B	51±7	1.53±0.21
			C	120±11	3.60±0.33
			D	77±9	2.31±0.26
19639	2017-01-04	32.92	A	249±16	7.56±0.48
			B	46±7	1.40±0.21
			C	113±11	3.43±0.32
			D	68±8	2.06±0.25

3.2 Single-image analysis: all Chandra observations

Once the data were reduced, the source and background were spectra extracted with their response matrices, I first produced the source light curves to evaluate the single image components' variability during each observation and found them consistent with being stable. Then, I considered the multi-epoch light curves, to qualitatively assess the variation of each component through years. Thus, I moved to the spectral analysis, starting from the simplest model, i.e. a single power law (Sec. 3.2.2), to focus the analysis on the high-statistics sample (Sec. 3.3). This allowed to better investigate the spectral characteristics of the source through the best *Chandra* spectra available. I analyzed every single image spectra using `XSPEC, v12.10c` (Arnaud, 1996), over the 0.4 - 7.0 keV observed energy range. When the analysis involved all the spectra, I used the one count/bin binning and the *C-stat*; when limited to the high-statistics sample, I considered a higher than twenty-count-per-bin binning and the χ^2 statistics. All the plotted spectra were rebinned for better visualization purposes. All the errors of the fit parameters are calculated at 90% confidence for one parameter of interest (Avni, 1976; Lampton et al., 1976), which corresponds to 1.6σ.

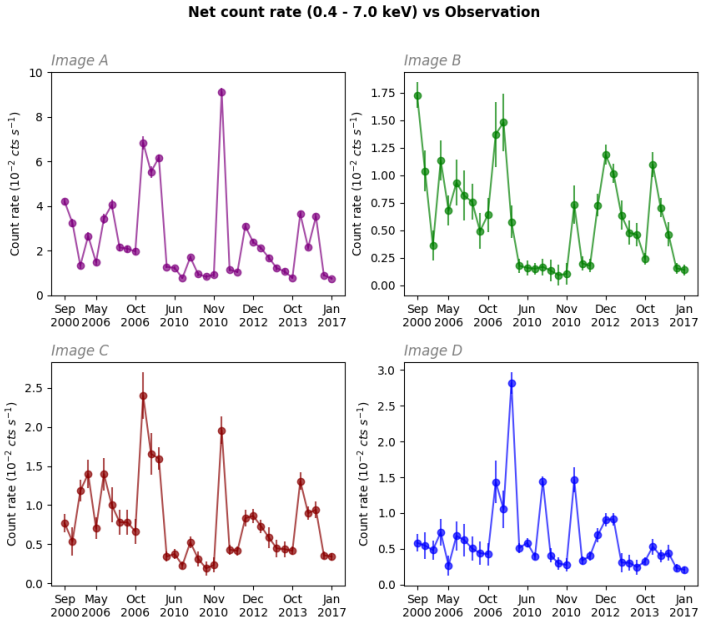

Figure 3.5: Individual-image multi-epoch light curves, the mean count rate of each observation vs time. First row, from the left: image A, image B. Second row, from the left: image C, image D. The error bars are derived by the counts Poisson error.

3.2.1 Multi-epoch light curves

In order to assess if and how the quasar activity varied through time, as a preliminary analysis, I produced the multi-epoch light curves of the individual images, plotting the $0.4 - 7.0$ keV mean count rate per observation of each image (values in Table 3.1) versus the respective epoch, as displayed in Figure 3.5.

The variability patterns they show are quite unexpected when related to each other. Given that the time delay induced by the lens (see Section 1.3.1) is constrained to be much lower than the intrinsic variability timescale expected for the quasar itself[3], one would have supposed that the light curves would have shown the same shape, which is not exactly what Figure 3.5 displays. Under this scenario, discrepancies in the mean count rate trends among the images could be explained as the result of differential magnification induced by micro-lensing effects that, given the proximity of the lens, are expected to exhibit variability on a few months timescale. Indeed, the optical light curves of Corrigan et al. (1991) and Ostensen et al. (1996) do show that micro-lensing actually generates flux variations among the Einstein Cross images. Given that gravitational lensing is wavelength-independent,

[3]Intrinsic variability timescale: $\Delta t^{\rm rest}_{10R_g} \approx 17$hrs $\longrightarrow$ $\Delta t^{\rm obs}_{10R_g} \approx 46$hrs.

similar effects are expected in the X-ray band as well. In fact, micro-lensing induced X-ray variability among different epochs has actually been claimed (Chen et al., 2011; Chen et al., 2012). Therefore, the discrepancies among the four light curves trends are likely due to micro-lensing effects. To verify that such differences could not be ascribed to the *Chandra* effective area decrease induced by the contamination of the ACIS filters along the years or to differential absorption among the images due to the lensing galaxy, another set of multi-epoch light curves was produced, excluding the energies that are most affected by these phenomena, i.e. the soft band below 1.5 keV. Moreover, also the energies above 5 keV were excluded to maximize the signal-to-noise ratio. The results were unchanged with respect to Figure 3.5: images A and C remain those with the most similar light curves, while images B and D seem to show a few different trends compared to each other and to images A and C. To assess how important and how frequent these micro-lensing events are, a different approach would be required. Micro-lensing events can be studied from the variation of the flux ratios of pairs of images through time, and their amplitude can be inferred by comparison to a baseline ratio, selected at a wavelength band not affected by micro-lensing (i.e. emission at wavelengths linked to a region much larger that the Einstein radius of the system). However, a detailed micro-lensing analysis is out of the scope of this thesis, even though surely of interest and relevance by itself.

3.2.2 Single power-law spectra and photon index variability

The usual first approach to X-ray spectroscopy data of accreting sources is the residual analysis of a single power law modeling (see Section 1.1.2). The fit residuals are calculated as (data-model)/error: they express the deviation between the model and the data point in units of sigma. Alongside the statistical tests, the quality of a fit can be inferred based on the residual value and their overall distribution with respect to the best fit.
I fitted all the *Chandra* spectra through a Galactic absorption and single power-law model (`phabs*zpowerlw`, in `XSPEC` notation) over the $0.4 - 7.0$ keV observed-frame energy band (1.1 - 18.9 keV rest frame). Based on the target coordinates, the Galactic absorption corresponds to a column density of $N_H = 5.06 \cdot 10^{20}$ cm^{-2} (Kalberla et al., 2005). A single power-law fit gives a good description of the data for some observations, with all residuals showing small deviations from the best-fit values (e.g. ObsID 6839 image D in Figure 3.6(a)), while many require a more in-depth analysis, given that they present more data points deviating from the best-fit (for instance see the residuals of ObsID 14517 image C in Figure 3.6(b)).
Given the large number of X-ray spectra available and the medium-low statistics that most of them show, instead of focusing on each residuals distribution, I thus chose to inspect the variability of the photon index as a function of time. In Figure 3.7 I show the photon index, for each image, as a function

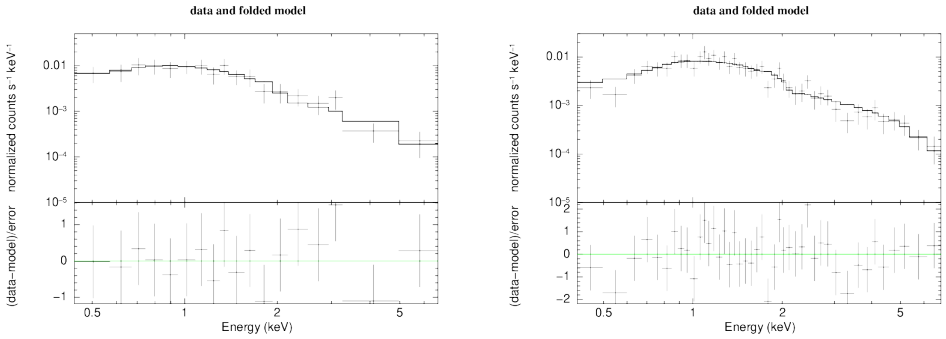

(a) ObsID 6839, image D.

(b) ObsID 14517, image C.

Figure 3.6: Single power-law fits and residuals of *Chandra* ObsID 14517 image A (left panel) and ObsID 6839 image D (right). For the fitting, the spectra are binned at one-count-per-bin, but further rebinned for visualization purposes so that each bin contains a maximum of 5 counts.

of the observation epoch as a proxy of its variability. The figures show that the power law seems to vary across the different epochs and that this trend seems to be qualitatively the same for all of the four images. Fitting with a constant and applying the χ^2 test[4], all the four power law distributions are highly variable ($> 99.9\%$ confidence), in agreement to what found by Chen et al. (2012), while their ratios are consistent with being constant. Therefore, the qualitatively predicted trends are quantitatively confirmed.
Such variation could either be intrinsic to the source or ascribed to an absorber that varies in time; in particular, the presence of absorption, if not included in the spectral fit, could produce a flatter power-law with respect to the expected values for an AGN ($\Gamma \sim 1.8 - 2.0$; Piconcelli et al., 2005). To check what is the most plausible explanation for Q2237+030, the natural approach would be adding an absorption component to the model and see whether it is actually required by the data, considering each spectrum individually. Such procedure, however, could not yield totally reliable results given the intrinsic degeneracy that exists between the photon index and the absorber's column density, and the limited photon statistics for most of the spectra. Therefore, I focused on the high-statistics sample in order to assess how significant such degeneracy is.

[4]All the fits required to analyze the variation of the spectral best-fit parameters are performed rescaling the 90% error bars to 1σ.

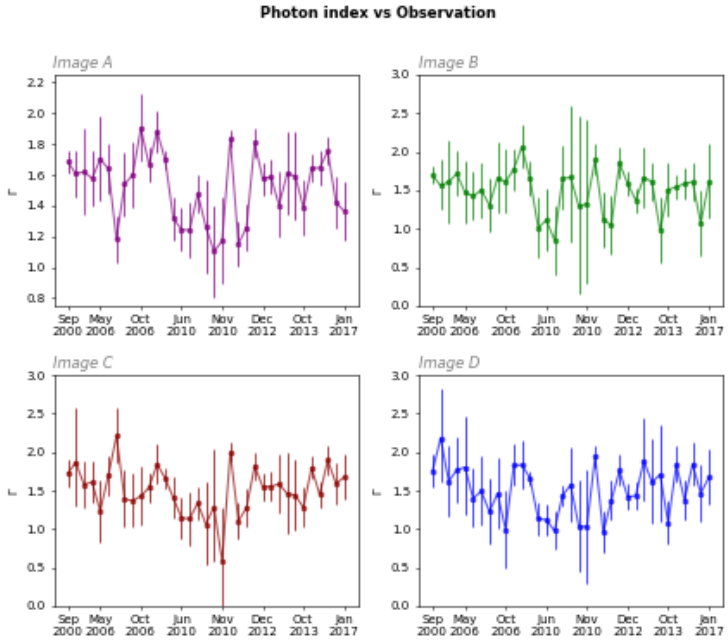

Figure 3.7: Variation of the photon index for each image as a function of time.

3.3 Single-image analysis: High-statistics sample

The high-statistics sample comprises fourteen spectra (almost all image A, see Table 3.2), which show more than 500 source net counts in the 0.4 – 7.0 keV observed energy band. For this sample, it is possible to apply the χ^2 statistics after binning the data to 20 cts/bin.

As for all the other spectra, I first applied a simple power-law and Galactic absorption modeling, as explained above. Once again, their residuals show some structures, implying the need for a more complex modeling; for instance, Figure 3.8 displays the best-fit spectrum and residuals for ObsID 12831 image A, which shows a prominent emission line at $E_{obs} \sim 2.5$ keV and structured absorption at higher energies.
Therefore, I analyzed the significance due to the addition of an absorption component (Section 3.3.1) and the presence of absorption/emission narrow features (Section 3.3.2) through the χ^2 statistics.

Table 3.2: List of the information for the *Chandra* high-statistics sample and details of the individual image spectra. The source net counts are referred to the 0.4-7.0 keV observed energy band and similarly are the count rates.

ObsID	Date	Expo (ks)	Image	Net Counts	CR (10^{-3} cts/s)
431	2000-09-06	30.29	A	1272±36	41.99±1.18
			B	523±23	17.26±0.26
6839	2006-11-29	7.87	A	538±23	68.32±2.95
11534	2009-12-31	28.46	A	1756±42	61.70±1.47
			D	802±28	28.18±1.00
11538	2010-10-02	29.36	A	501±22	17.06±0.76
12831	2011-05-14	29.36	A	2677±52	91.19±1.76
			C	575±24	19.58±0.82
13961	2012-08-02	29.24	A	906±30	30.98±0.10
14513	2012-12-26	28.62	A	684±26	23.89±0.91
14514	2013-01-05	29.36	A	622±25	21.18±0.85
14517	2014-05-14	29.36	A	1071±33	36.48±1.11
14518	2014-06-08	29.28	A	628±25	21.45±0.86
18804	2016-04-24	28.60	A	1009±32	35.28±1.11

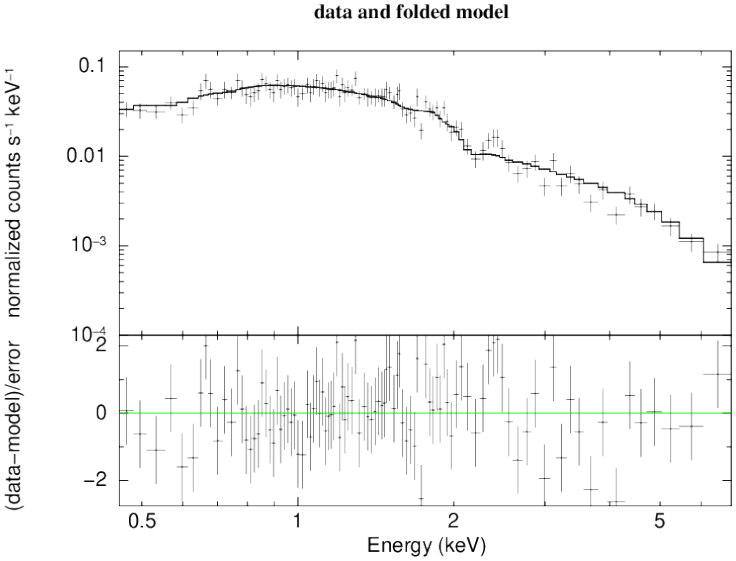

Figure 3.8: Data and best-fit model (top panel) and residuals (bottom panel) of ObsID 12831 image A using a single power-law and Galactic absorption model. The reported energies are in the observed frame.

3.3.1 Photon index - column density degeneracy

To assess the degeneracy that exists between the photon index Γ and the column density N_H of the absorber, I added a `zphabs`[5] multiplicative component in `XSPEC` (model `phabs*zphabs*zpowerlw`) and I focused on two aspects: i) the actual need for such absorption, evaluated through its statistical significance; ii) the determination of the extent of the mentioned degeneracy through the confidence contours[6].

Table 3.3: Summary of the best-fit parameters for the model `phabs*zphabs*zpowerlw` when applied to the high-statistics sample. The sources in bold are those that actually require a cold absorber component at a significance level above 99% according to the F-test.

ObsID	Image	Γ	N_H (10^{22} cm^{-2})	$\Delta\chi^2$	Confidence
431	A	$1.86^{+0.12}_{-0.12}$	$0.34^{+0.20}_{-0.20}$	8.4	90%
	B	$1.90^{+0.42}_{-0.36}$	$0.53^{+0.23}_{-0.20}$	5.9	90%
6839	A	$1.80^{+0.20}_{-0.20}$	$0.46^{+0.52}_{-0.42}$	3.2	68%
11534	**A**	$1.91^{+0.11}_{-0.10}$	$0.62^{+0.29}_{-0.25}$	19.3	**99%**
	D	$2.01^{+0.20}_{-0.18}$	$1.28^{+0.57}_{-0.48}$	24.3	**99%**
11538	**A**	$2.06^{+0.28}_{-0.26}$	$2.88^{+1.40}_{-1.17}$	22.0	**99%**
12831	A	$1.98^{+0.09}_{-0.09}$	$0.27^{+0.22}_{-0.21}$	4.7	90%
	C	$2.10^{+0.27}_{-0.24}$	$0.50^{+0.60}_{-0.49}$	2.9	68%
13961	A	$2.02^{+0.18}_{-0.16}$	$0.67^{+0.53}_{-0.44}$	7.0	90%
14513	A	$1.80^{+0.20}_{-0.18}$	$0.88^{+0.67}_{-0.56}$	7.1	90%
14514	A	$1.79^{+0.22}_{-0.20}$	$0.77^{+0.80}_{-0.66}$	3.7	68%
14517	A	$1.79^{+0.14}_{-0.13}$	$0.59^{+0.49}_{-0.40}$	6.5	90%
14518	A	$1.84^{+0.24}_{-0.22}$	$1.01^{+1.03}_{-0.84}$	4.1	68%
18804	**A**	$2.10^{+0.19}_{-0.18}$	$1.45^{+0.85}_{-0.71}$	13.8	**99%**

Furthermore, I speculated on the position of such absorber; unlike all the other spectral analysis that can be found in literature (for instance, Fedorova et al., 2008; Reynolds et al., 2014), given the variation of the spectral shape (Fig. 3.7) I assumed it to be intrinsic to the quasar, therefore I set its redshift at z = 1.695. The reason for this assumption relies on the fact that if the absorber were placed in the lensing galaxy, then one would expect its column

[5] This component accounts for the photoelectric absorption produced by a cold absorber of column density N_H placed at a certain redshift z. Figure 4.8 in Section 4.2 displays how varying the column density of a neutral medium affects the absorption.

[6] The confidence contours correspond to the contour lines of the χ^2 probability function in a N-parameter space, usually a 2D-space; in this case, it is the parameter space of photon index and column density. Conventionally, when referred to a 2D space, the confidence contours correspond to the 68% (red), 90% (green) and 99% (blue) probability levels.

density to be nearly constant through the epochs; given the photon index variation (Fig. 3.7), it is reasonable to think that it could be produced by a varying absorber other than a variation of the X-ray emission intrinsic to the source. To verify this hypothesis, the N_H values in the different epochs, including their errors, would have to be variable. Therefore, this procedure was aimed at both assessing how broad the degeneracy is and investigating the position of such absorber.

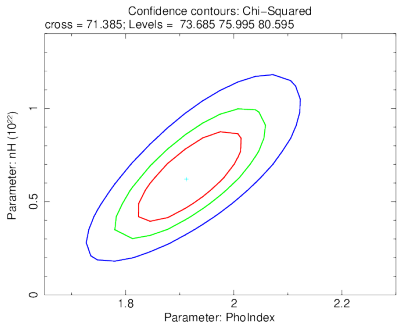

(a) ObsID 11534, image A.

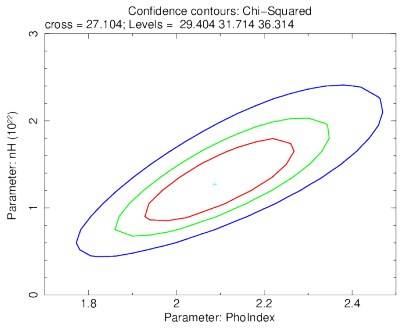

(b) ObsID 11534, image D.

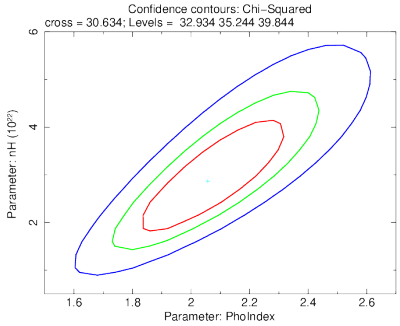

(c) ObsID 11538, image A.

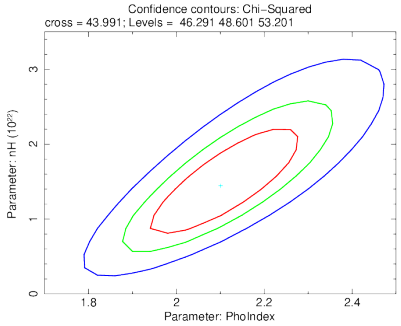

(d) ObsID 18804, image A.

Figure 3.9: Confidence contours of the four *Chandra* observations that require a cold absorber. *On the x axis*: photon index; *on the y axis*: column density (10^{22} cm^{-2}).

Table 3.3 summarizes the best-fit values; only four spectra out of fourteen actually require a cold absorber (11534 image A and D, 11538 image A, 18804 image A) at more than 99% confidence (see Figure 3.9), six spectra[7] require extra absorption at 90−99% confidence, while the remaining four[8] do not require this component ($<$ 68% confidence level). Figures 3.10 and 3.11 show the best-fit values of column density and photon index as a function of the observation ID. ObsID 11538 image A (Fig. 3.9(c)) is the one that presents the least constrained parameters: its 99% contour (2.6σ) stretches from $N_H \simeq 10^{22}$ cm^{-2}, $\Gamma \simeq 1.6$ to $N_H \simeq 6 \cdot 10^{22}$ cm^{-2}, $\Gamma \simeq 2.5$.

[7] ObsIDs 431 A, 431 B, 12831 A, 13961 A, 14513 A, 14517 A.
[8] ObsIDs 6839 A, 12831 A, 14514 A, 14518 A.

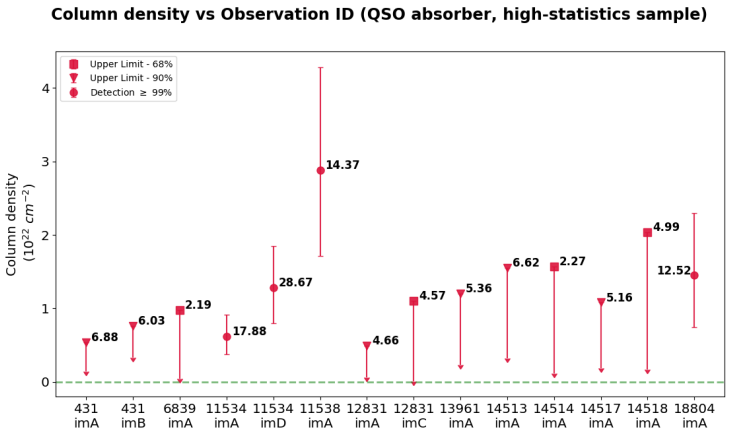

Figure 3.10: Column density vs. Observation ID with 90% error bars (1.6 σ) for the high-statistics sample. The datasets which do not require a cold absorber are indicated as triangles and upper limits (ObsIDs 6839 A, 12831 A, 14514 A, 14518 A); those that require a 90% confidence level are indicated as squares and upper limits (ObsIDs 431 A, 431 B, 12831 A, 13961 A, 14513 A, 14517 A); those that actually require a cold absorber (> 99% confidence) are indicated as dots (ObsIDs 11534 A, 11534 D, 11538 A, 18804 A). The green dashed line corresponds to no extra obscuration besides the Galactic ($N_H^{MW} = 0.05 \times 10^{22}$ cm^{-2}).

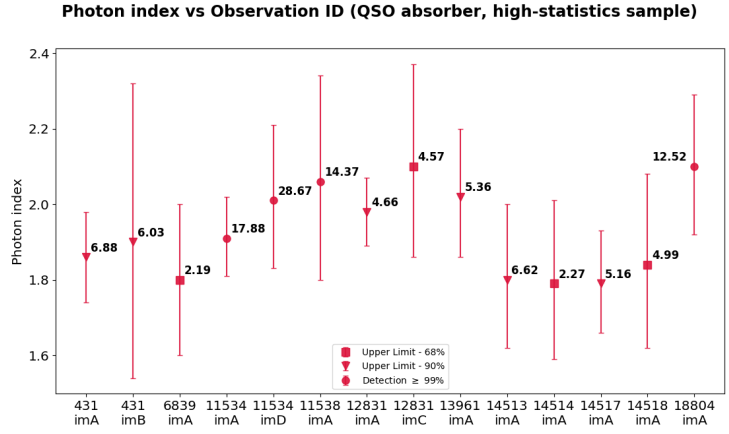

Figure 3.11: Photon index vs. Observation ID with 90% error bars (1.6 σ) for the high-statistics sample. The symbols code is the same as Figure 3.10: the datasets which do not require a cold absorber are indicated as triangles (ObsIDs 6839 A, 12831 A, 14514 A, 14518 A); those that require a 90% confidence level are indicated as squares (ObsIDs 431 A, 431 B, 12831 A, 13961 A, 14513 A, 14517 A); those that actually require a cold absorber (> 99% confidence) are indicated as dots (ObsIDs 11534 A, 11534 D, 11538 A, 18804 A).

To test the assumption on the location of the absorber, I compared the two detected absorbers that show the column densities varying most (ObsID 11534 image A and 11538 image A) by plotting their 90% confidence contours (1.6 σ) of column density vs. photon index to see if they were consistent. As shown in Figure 3.12, while their photon indices are in agreement, the column densities are not consistent within 1.6 σ, which means that the absorber is, at more than 90% confidence, placed at the redshift of the quasar. Furthermore, the time interval among the two observations (see Table 3.2) is ~ 275 d in the observer frame, which means ~ 102 d $\simeq 0.3$ yrs in the quasar rest frame; this fact further supports the argument that the absorber is placed at the source redshift instead of at that of the lens.

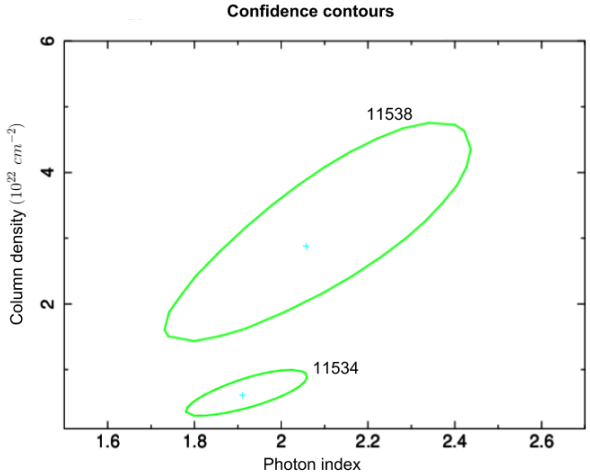

Figure 3.12: 90% confidence contours of N_H vs. Γ for observations 11534 A and 11538 A, which correspond to the spectra that show the largest difference in column density, among the four that require a cold absorber at more than 99% confidence level.

Having tested the location of the cold absorber and the presence of degeneracy with the power law slope, one possible approach is to set a value for the photon index and see how the column density changes, given that this should break the intrinsic degeneracy among the two parameters.
The chosen value for the photon index corresponds to the average of those of each spectra from the sample. It was evaluated through two different methods: first, I fitted the points in Figure 3.11 with a constant[9] using `Python` method `scipy.optimize.curve_fit()`; second, I calculated the average photon index weighted over the counts of each spectrum. The two methods yielded consistent results, leading to an average photon index of $< \Gamma > = 1.93 \pm 0.05$, which is in agreement to the expected power-law slope for an AGN (e.g., Piconcelli et al., 2005). I then froze the power law slope to

[9] According to the χ^2 test, the photon index distribution of the high-statistics sample is consistent with being constant.

this value and repeated the spectral fitting procedure over the sample. Figure 3.13 shows the column density best fit values; as in the previous case, the errors are still large, except for ObsID 12831 image A which does not require an absorption component (the column density upper limit is consistent with zero) and ObsID 12831 image C whose N_H is consistent with zero including its errors. The trend in column density shown in Figure 3.13 was found significantly consistent with being overall constant[10]. When restricting the fitting procedure to the four spectra that require the absorber at more than 99% confidence (11534 image A and D, 11538 image A, 18804 image A), the column densities are found to be variable at more than 99% confidence.

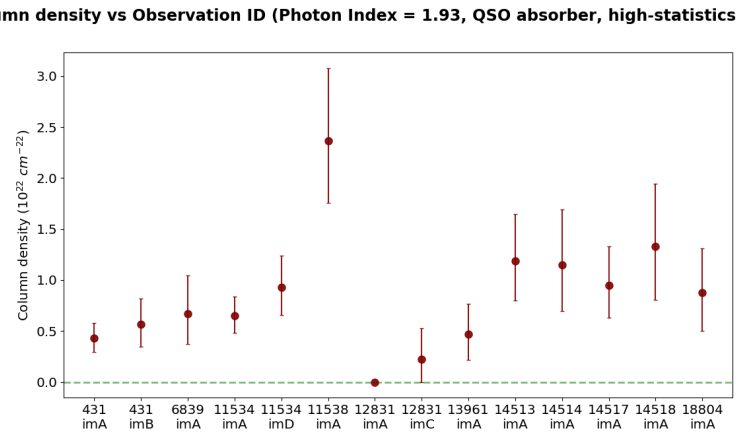

Figure 3.13: Best-fit parameters for the model `phabs*zphabs*zpowerlw` with $<\Gamma>= 1.93$ applied to the high-statistics sample. The green dashed line corresponds to no extra obscuration besides the Galactic ($N_H^{MW} = 0.0506 \times 10^{22}$ cm^{-2}); the column density of ObsID 12831 image A is consistent with zero and its error bars are contained in the dot.

3.3.2 Evaluation of emission/absorption features

A first evaluation of emission/absorption features was carried out as a blind search by applying the method developed in Tombesi et al. (2010). The approach relies on the χ^2 statistics and the F-test, therefore it can be applied only on the high-statistics sample. The procedure can be summarized in few basic steps:

- First step is to provide a good enough representation of the continuum and store its χ^2; in this case, it implies a power law and, where needed (see Section 3.3.1), a cold absorber component;

[10]The values were fitted with a constant applying the same `Python` method as for the photon index, excluding ObsID 12831 image A due to its (almost) null error bars.

- Second step is to include a narrow line component (`gauss`[11]); by narrow we mean that it is unresolved, therefore its width has to be frozen at a value lower than the telescope energy resolution (i.e. $\sigma = 10$ eV);
- Third step is to search both for absorption and emission features performing a series of fits, varying the line energy and normalization[12]; the χ^2 value of each trial is stored to produce a grid of χ^2 in the line energy-normalization parameter space;
- Forth step is to plot the contours corresponding to the same $\Delta\chi^2$ w.r.t. the continuum model; these values are those equivalent to the 68%, 90% and 99% confidence contours translated in $\Delta\chi^2$ through the F-test for the addition of two parameters: $\Delta\chi^2 = -2.3, -4.61$ and -9.21 (negative as they account for an improvement in the fit when adding the new component).

These plots are to be read in the opposite way with respect to the standard contour plots, since the inner contours indicate a higher significance of the added component.
I applied this procedure to all the spectra of the high-statistics sample over the 0.4 – 5.0 keV observed energy range (∼1.1 – 13.5 keV rest frame energy band), which corresponds to the range of interest for both soft X-ray features and iron resonant lines and given that above 5 keV the modeling of the continuum is less constrained. The energy steps of every fit were chosen on the basis of the total counts C_{tot} of each spectra. The lower boundary was determined by the minimum number of bins of those with the least counts[13], while for the spectra with higher statistics the number of steps was chosen as the trade off between their total counts and the number of bins:

- $500 < C_{tot} \leq 750$ cts $\rightarrow$ $\Delta E_{obs} = 0.184$ keV ($\Delta E_{rest} = 0.496$ keV);
- $750 < C_{tot} \leq 1000$ cts $\rightarrow$ $\Delta E_{obs} = 0.092$ keV ($\Delta E_{rest} = 0.248$ keV);
- $C_{tot} > 1000$ cts $\rightarrow$ $\Delta E_{obs} = 0.046$ keV ($\Delta E_{rest} = 0.124$ keV).

Therefore, in the last case, the sampling of the iron lines region was done at about one quarter of the resolution provided by the ACIS-S3 CCD at those energies ($FWHM_{S3} \sim 150$ eV at $E_{obs} \sim 2.5$ keV, see Fig. 2.5).

[11] The parameters for the `gauss` model are: observer frame line energy E, line normalization, line width σ. Fixing the width, adding a line to the model corresponds to the addition of two more parameters, its energy and normalization.

[12] The actual steps are calibrated over each spectrum separately, based on its statistics, shape and the energy range of interest.

[13] Binning a 500-counts-spectrum at 20cts/bin yields a total of 25 bins; therefore, in order not to oversample the instrument energy resolution, no more than 25 steps were allowed. This means an energy step of 4.6keV/25 = 0.184keV.

Table 3.4: Rest-frame energies and intensities of the emission/absorption lines detected at more than 90% confidence in the high-statistics sample. Those showing more than 99% confidence are reported in bold. The intensity of the absorption lines is given as negative.

ObsID	Image	E_{line} (keV)	Intensity (10^{-5} erg/cm^2/s/keV)	Confidence
431	A	$3.19^{+0.10}_{-0.11}$	$-0.38^{+0.26}_{-0.26}$	90%
		$\mathbf{11.92^{+1.69}_{-0.23}}$	$-0.58^{+0.28}_{-0.38}$	**99%**
		$5.90^{+0.31}_{-0.36}$	$0.64^{+0.42}_{-0.42}$	90%
6839	A	$4.15^{+0.22}_{-0.14}$	$2.43^{+1.59}_{-1.59}$	90%
		$3.09^{+0.10}_{-0.17}$	$-2.54^{+1.70}_{-1.76}$	90%
		$9.79^{+0.09}_{-0.06}$	$-6.81^{+3.58}_{-3.87}$	90%
11534	A	$8.01^{+0.42}_{-0.14}$	$-0.90^{+0.58}_{-0.66}$	90%
		$3.65^{+0.13}_{-0.10}$	$1.30^{+0.91}_{-0.90}$	90%
		$5.35^{+0.13}_{-0.12}$	$1.16^{+0.71}_{-0.71}$	90%
11534	D	$2.25^{+0.10}_{-0.10}$	$1.70^{+1.43}_{-1.12}$	90%
11538	A	$2.09^{+0.08}_{-0.28}$	$-3.06^{+1.37}_{-1.44}$	90%
12831	A	$\mathbf{10.90^{+0.53}_{-0.20}}$	$-0.90^{+0.48}_{-0.63}$	**99%**
		$9.78^{+0.43}_{-0.18}$	$-0.76^{+0.50}_{-0.63}$	90%
		$4.04^{+0.14}_{-0.15}$	$1.24^{+0.87}_{-0.86}$	90%
		$\mathbf{6.47^{+0.11}_{-0.12}}$	$1.94^{+0.94}_{-0.94}$	**99%**
13961	A	$\mathbf{9.39^{+1.90}_{-0.08}}$	$-0.72^{+0.38}_{-0.38}$	**99%**
		$3.78^{+0.16}_{-0.12}$	$0.61^{+0.34}_{-0.34}$	90%
		$6.56^{+0.24}_{-0.17}$	$0.44^{+0.35}_{-0.33}$	90%
14513	A	$6.98^{+0.81}_{-0.22}$	$-0.75^{+0.56}_{-0.81}$	90%
14514	A	$12.51^{+0.10}_{-2.28}$	$-1.38^{+0.94}_{-1.00}$	90%
		$3.62^{+0.30}_{-0.19}$	$0.85^{+0.56}_{-0.56}$	90%
		$5.99^{+0.13}_{-0.34}$	$0.12^{+0.08}_{-0.07}$	90%
14517	A	$\mathbf{12.41^{+0.08}_{-0.19}}$	$-0.83^{+0.42}_{-0.42}$	**99%**
		$5.70^{+0.33}_{-1.19}$	$0.65^{+0.44}_{-0.44}$	90%

The resulting contour plots are displayed in Figures 3.14 – 3.16. The black lines in the plots indicate the intensity and energy values that produce a $\Delta\chi^2 = +0.5$, thus a slightly worse best fit with respect to the baseline model. The black lines diverge in normalization below $\simeq 0.8$ keV almost for each spectrum. This is indicates that the continuum at those energies is unconstrained, since the addition of a line component produces almost no difference in the quality of the fit, even considering a rather wide range of intensities. At higher energies, this effect is present only in ObsID 12831 C, one of the high-statistics spectra with less than 600 counts (see Table 3.2). These effects are likely induced by the low statistics of the boundary bins. The fact that the deviation below $\simeq 0.8$ keV is present for each spectra while that above $\simeq 4$ keV is not, is likely due to the intrinsic shape of *Chandra* effective area ($A_{\rm eff}^{[0.8\ {\rm keV}]} < A_{\rm eff}^{[4\ {\rm keV}]}$, see Fig. 2.3). Moreover, Galactic absorption is significant only at the lowest energies, producing an additional decrease of the statistics below $\simeq 0.8$ keV. Eight spectra[14] show a broad absorption in the 3 – 5 keV observed energy range (∼8.1 – 13.5 keV rest frame), but this seems to be highly significant (> 99%) only for four spectra (ObsIDs 431 A, 12831 A, 13961 A, 14517 A); given the shape of the contours, such broad absorption could probably be produced by two blended lines. ObsID 11538 A, instead of a broad feature, shows a narrow absorption line (> 90% confidence) slightly above 4 keV obs. frame (10.78 keV r.f.). Seven spectra show a narrow absorption line below 1 keV obs. frame (2.69 keV r.f.) and for one of these the contours indicate it to be highly significant (> 99% confidence for ObsID 431 A).

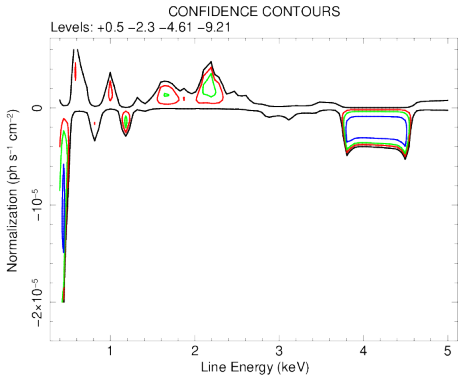

(a) ObsID 431, image A.

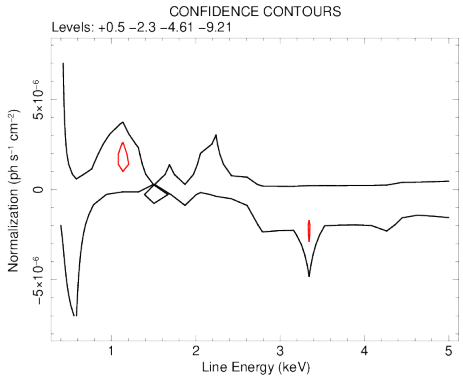

(b) ObsID 431, image B.

Figure 3.14: Confidence contour plots of line energy vs. intensity with respect to the absorbed single power-law model (68% (red), 90% (green), 99% (blue) levels). The black line indicates $\Delta\chi^2 = +0.5$ and represents the reference level for the continuum model. *On the x axis:* observed-frame energy.

[14] ObsIDs 431 A, 6839 A, 11534 A, 12831 A, 13961 A, 14513 A, 14514 A, 14517 A.

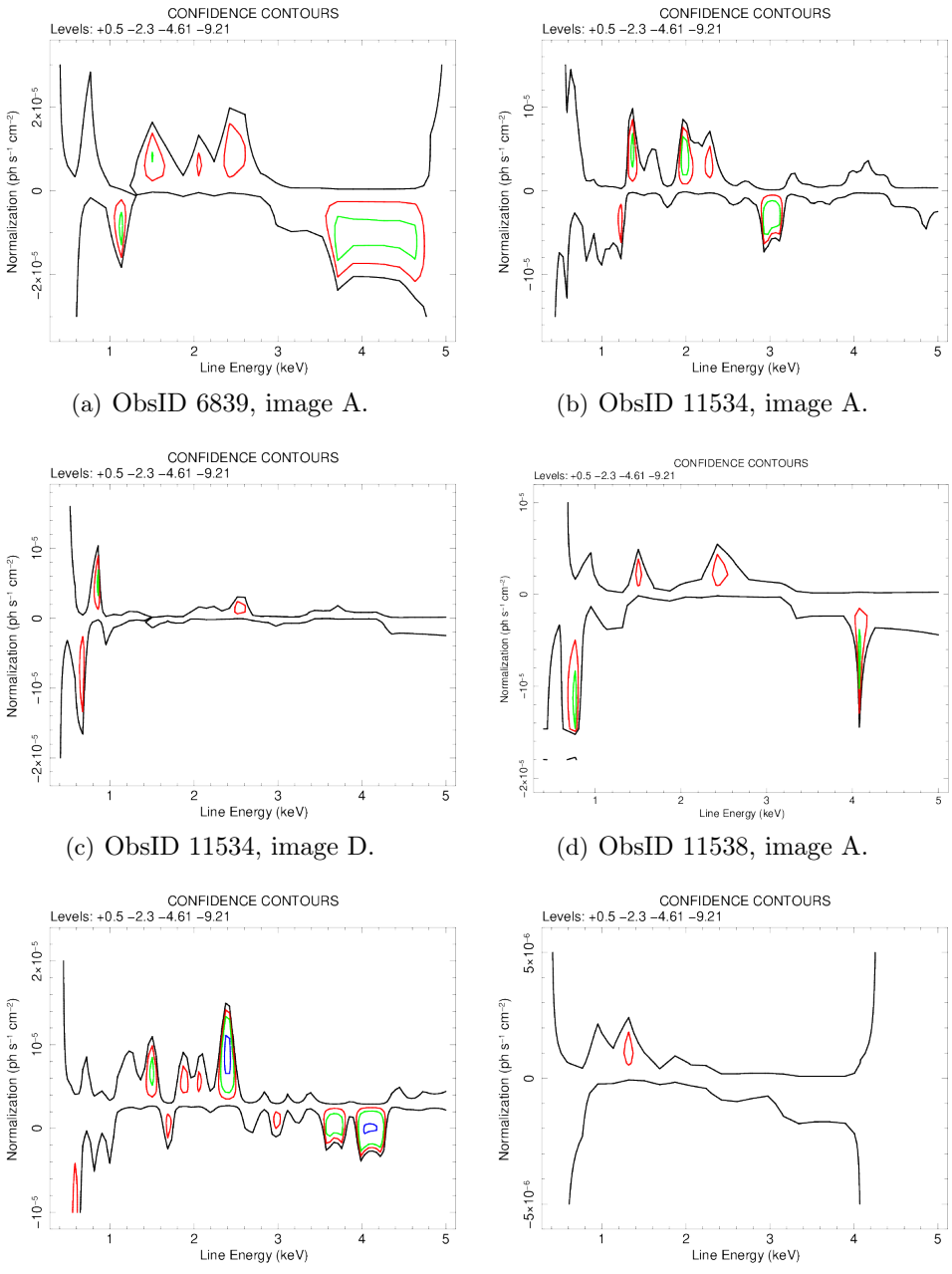

(a) ObsID 6839, image A.

(b) ObsID 11534, image A.

(c) ObsID 11534, image D.

(d) ObsID 11538, image A.

(e) ObsID 12831, image A.

(f) ObsID 12831, image C.

Figure 3.15: Confidence contour plots of line energy vs. intensity with respect to the absorbed single power-law model (68% (red), 90% (green), 99% (blue) levels). The black line indicates $\Delta\chi^2 = +0.5$ and represents the reference level for the continuum model. *On the x axis:* observed-frame energy.

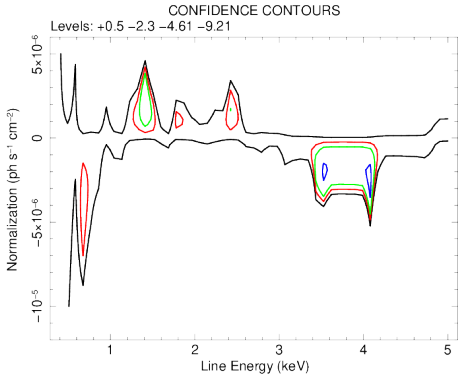

(a) ObsID 13961, image A.

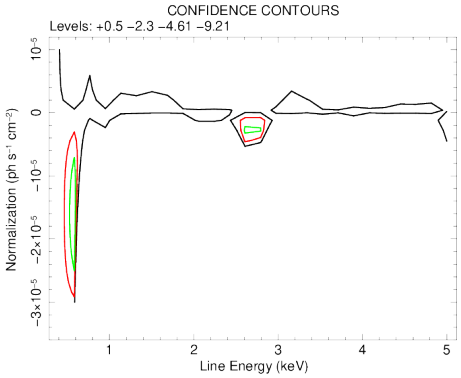

(b) ObsID 14513, image A.

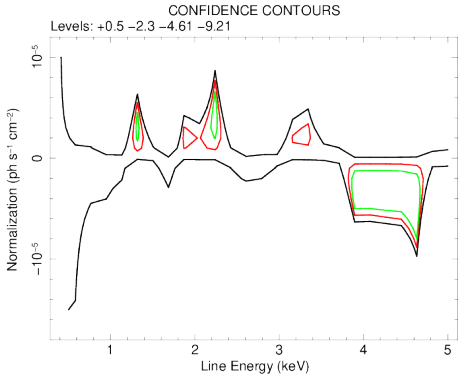

(c) ObsID 14514, image A.

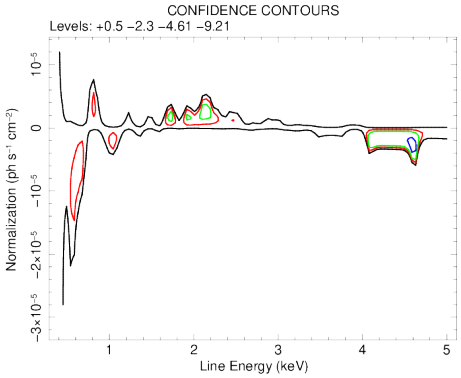

(d) ObsID 14517, image A.

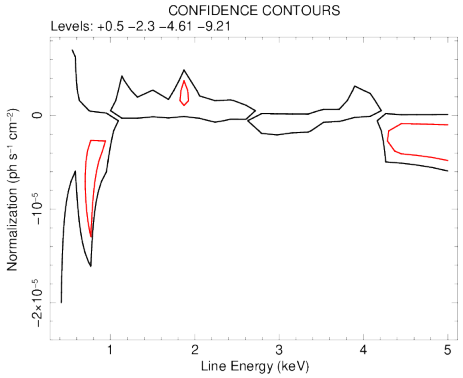

(e) ObsID 14518, image A.

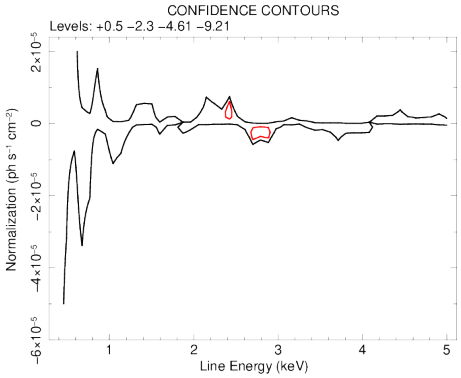

(f) ObsID 18804, image A.

Figure 3.16: Confidence contour plots of line energy vs. intensity with respect to the absorbed single power-law model (68% (red), 90% (green), 99% (blue) levels). The black line indicates $\Delta\chi^2 = +0.5$ and represents the reference level for the continuum model. *On the x axis:* observed-frame energy.

Regarding the emission lines, from this blind search, eight spectra[15] show emission lines at energies below $\simeq 3.5$ keV at more than 90% significance (but $< 99\%$); only ObsID 12831 A shows a highly significant emission line, at $\sim$2.4 keV obs. frame ($\sim$6.47 keV r.f.). These features, as those in absorption, seem to be qualitatively variable through the epochs with energies varying from ≈ 1.5 keV obs. frame to ≈ 3.5 keV obs. frame ($\sim$4.0 and 9.4 keV r.f.).

The significance of each absorption/emission line that has more than 90% confidence in Figures 3.14 – 3.16 (i.e., those that present the green contours) was evaluated adding a narrow `zgauss`[16] component in the respective spectrum, searching for the best fit and producing the standard confidence contours for each of them. This yielded almost the same results as the Tombesi et al. (2010) tool, with the exception of the absorption lines below 1 keV obs. frame, whose significance is, in each case, lower than that shown in Figures 3.14 – 3.16 (and never above 90%), probably due either to the fact that they are placed at the very soft energy end of the spectra or that the continuum modeling is not correctly reproducing the lower energies part.
Table 3.4 summarizes all the energies and intensities of the lines detected at more than 90% confidence, with those at more than 99% shown in bold (four absorption lines and one emission line).

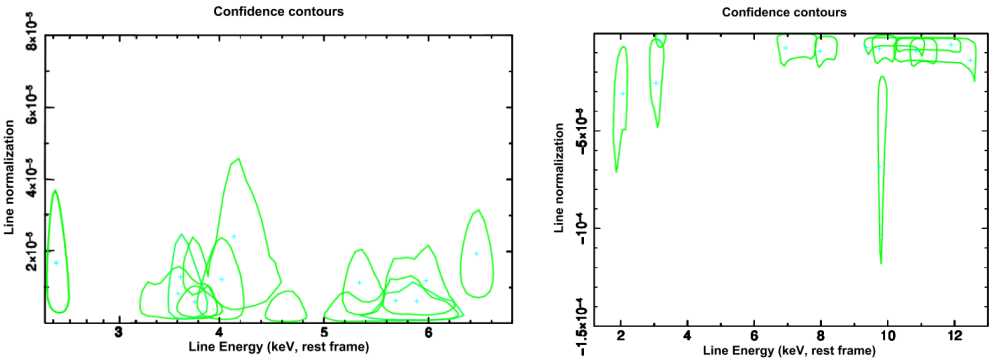

(a) Emission features. (b) Absorption features.

Figure 3.17: Overlapping of the 90% energy-normalization confidence contours (1.6σ) for the emission and absorption lines reported in Table 3.4. (a): ObsIDs 431 A, 6839 A, 11534 A, 11534 D, 12831 A, 13961 A, 14514 A, 14517 A. (b): ObsIDs 431 A, 6839 A, 11534 A, 11538 A, 12831 A, 13961 A, 14513 A, 14514 A, 14517 A.

To inspect the persistence of such features through the different spectra, I overlapped the 90% confidence contours of the emission and absorption lines separately; these are displayed in Figure 3.17. Figure 3.17(a) shows that the emission lines almost evenly cover the 3.2 – 6.6 keV rest-frame energy

[15] ObsIDs 431 A, 6839 A, 11534 A, 11534 D, 12831 A, 13961 A, 14514 A, 14517 A.

[16] This is the same as the `gauss` component, but returns the rest-frame energy. The redshift was frozen to the systemic redshift of the quasar.

band and seem to cluster in two groups, one between 3.2 and 4.8 keV, and the other in the 5.0 – 6.2 keV; the absorption features (Fig. 3.17(b)) show a clustering around 11 keV, two lines at about 8.0 keV, two around 3.0 keV and one at 2.0 keV. Regarding the clustering at higher energies, what catches the eye is the one narrow absorption spike just below 10 keV; it corresponds to ObsID 6839 A and, in spite of its significance ($> 90\%$), it could be explained as a microlensing event that magnified part of the production region of the 10 keV absorption features. What is interesting is that, among these lines, those having a significance above 99% confidence are consistent with each other once their errors are taken into account; given their energies, they must be produced by a highly ionized absorber. Furthermore, these lines are detected in epochs whose minimum inter-observation time separation is about a year and 3 months[17] ($\sim$ 5.6 months proper time) and whose maximum exceeds ten years[18] (> 3.7 yrs proper time), thus this consistency suggests the highly ionized absorption component to be variable. The microlensed Fe Kα found by Dai et al. (2003) in the combined spectra of ObsIDs 431 and 1632 image A ($E = 5.7^{+0.2}_{-0.3}$ keV, $\sigma = 0.87^{-0.30}_{-0.15}$) is detected in the spectrum of ObsID 431 image A at the 90% confidence level a narrow line, probably due to the stacking they performed; the emission line at $E = 6.47^{+0.11}_{-0.12}$ detected with more than 99% confidence in ObsID 12831 A is inconsistent with the results of Reynolds et al. (2014) ($E = 6.82^{+0.12}_{-0.09}$), but this is probably due to the different approach: they analyzed the stacked spectra of 26 observations (ObsIDs 431 – 14514) spanning over 13yrs (4.8 yrs in the quasar rest frame), regardless of the possible variability between the different epochs.

3.3.3 On the statistical significance of the absorption features

It was argued in Protassov et al. (2002) that the F-test distribution cannot be used to assess the significance of a line component and they propose to build a Bayesian posterior predictive probability through Monte Carlo simulations instead. This method was applied to evaluate the actual significance of the absorption lines above 6 keV that, according to the contour plots, are significant at $> 90\%$ confidence level[19] (see Table 3.4). Therefore, following the procedure presented in Protassov et al. (2002), each of these eight spectra was simulated 1000 times through the `XSPEC fakeit` function from its null model (Galactic absorption, single power and if required – see Table 3.3 – cold absorption); the latter was then used to fit the simulated data, storing the best-fit χ^2. I then added a narrow absorption line component to the model with initial energy randomly seeded in the 6.4 – 13 keV range, then I searched for the new best fit and stored its χ^2 value. The yielded $\Delta\chi^2$ of the

[17] ObsIDs 12831,13961 $\longrightarrow$ May 2011, August 2012.
[18] ObsIDs 431, 12831 $\longrightarrow$ September 2000, May 2011.
[19] ObsIDs 431 A, 6839 A, 11534 A, 12831 A, 13961 A, 14513 A, 14514 A, 14517 A.

simulated data where then plotted against the best-fit energy of the line for each spectra and compared it with the $\Delta\chi^2$ obtained fitting the real data.

This method allowed us to evaluate the probability of having detected the line by chance: since the spectrum was simulated 1000 times, the probability of a spurious line detection is equal to 1/1000 times the number (x) of trials that show a $\Delta\chi^2$ higher than that of the best fit of real data, therefore the probability of a detection is (1-x).
This method yielded that eight out of fourteen spectra show a line detection above 90% confidence[20]. Through the binomial distribution I evaluated the probability of obtaining this result by chance:

$$P = \binom{n}{k} p^k \, q^{n-k} \tag{3.1}$$

where n=14, k=8, p=0.10 and q=0.90. The probability of a by-chance detection is $P = 1.5 \cdot 10^{-5}$, yielding a more than 99.99% significance (i.e. higher than 4σ) of the actual presence of the absorption features in the Fe resonant lines range.

3.4 Summary of the results obtained from Chandra

The partially uncorrelated trends of image B and D multi-epoch light curves (see Figure 3.5) might be due to micro-lensing effects that, given the proximity of the lensing galaxy, are thought to show a timescale variability of ∼months in this gravitationally lensed system. To actually assess the micro-lensing phenomena, more dedicated analysis is required. Significant variability of the spectral shape was inferred from the analysis of the whole *Chandra* sample, in the form of significant variability of the best-fit photon index through the epochs (Fig. 3.7).

Limiting the analysis to the so-called high-statistics sample (Table 3.2), I found that an absorption component is required at more than 99% confidence level in four cases (11534 image A and D, 11538 image A, 18804 image A) out of fourteen. Moreover, the column density of such absorber shows significant variability between the epochs in which it is observed; the rest-frame time elapsing the two nearest observations with detected absorption (ObsIDs 11534 and 11538) if ~ 0.3 yrs. Such variability and its timescale support the hypothesis of the absorber to be placed at the quasar redshift, instead of being produced by the lensing galaxy. Focusing on the narrow emission/absorption features, a blind search was carried out for the whole sample in the $0.4 - 5.0$ keV observed-energy band to limit the analysis to the range with the best representation of the continuum and that of interest for soft X-ray and iron resonant lines. Eight spectra[21] show emission lines below

[20] Of those eight, five show an absorption line detection with more than 99% confidence.
[21] ObsIDs 431 A, 6839 A, 11534 A, 11534 D, 12831 A, 13961 A, 14514 A, 14517 A.

3.5 keV (detected at more than 90%, but less than 99%, confidence). ObsID 12831 A shows a highly significant narrow emission line at $E \simeq 6.47$ keV rest frame whose energy is not consistent to that detected in the stacked *Chandra* spectra by Reynolds et al. (2014), while the line found by Dai et al. (2003) in only marginally detected in the spectrum of ObsID 431 A. Regarding the absorption lines, eight spectra show narrow features in the $3-5$ keV observed-frame energy band ($\sim 8.1-13.5$ keV rest-frame) at more than 90% confidence (assessed through Monte Carlo simulations). A certain persistence of the absorption features in this energy range can be inferred from the superposition of the 1.6σ energy-normalization confidence contours of the lines detected in the spectra out of the high-statistic sample (Fig. 3.17(b)). The overall significance of the detection of these absorption features is proved to be higher than 99.99%. The overlapped 1.6σ contours of the emission lines almost evenly cover the $\sim 3.2-6.6$ keV range, even though they seem to "cluster" in two groups, between $3.2-4.8$ keV and $5.0-6.2$ keV.

Chapter 4

The XMM-Newton view of the Einstein Cross

For a more complete analysis of Q2237+030 spectral properties, XMM-*Newton* data is fundamental; having an effective area substantially higher than the one of *Chandra*, it grants better quality spectra, although its poorer angular resolution does not allow to resolve the individual images.
XMM-*Newton* pointed the quasar three times: two of these observations are archival observations (2002 and 2016), while the most recent (2018, PI: Mauro Dadina) will become public in June 2019. Their properties are summarized in Table 4.1.

Table 4.1: Basic information of each XMM-*Newton* observation of Q2237+030.

Observation ID	Date	Exposure time (s)
0110960101	2002-05-28	42870
0781210201	2016-11-26	24900
0823730101	2018-05-19	141600

In the following sections, I will go through the reduction (Sec. 4.1) and the analysis (Sec. 4.2) of the whole XMM-*Newton* dataset.

I reduced and preliminarily analyzed both EPIC-MOS and EPIC-pn data, but then I focused only on the latter since the pn provides the best sensitivity and maximizes the spectra statistics; therefore, only the pn data analysis will be presented in the following sections.

4.1 Data reduction and spectra extraction

Raw data have been reduced using the most up-to-date calibration files. This was done through the standard procedure of XMM-*Newton* Science Analysis Software (SAS 16.1). I will briefly explain the generic basic steps of the process and how they were applied to the observations of Q2237+030.

The first step in the reduction of XMM-*Newton* data is the building of the Calibration Index File (CIF) from the Current Calibration Files (CCF) using the SAS task `cifbuild`. The CIF is then used to generate the calibrated event file from the Observation Data Files (ODF) through the tasks `odfingest` and `epproc` or `emproc`, based on the instrument (pn or MOS respectively).

The second step is to clean the calibrated event file. One big issue regarding XMM-*Newton* data is to be found in the interaction between its detectors and solar protons trapped in the Earth magnetosphere, causing the so-called soft-proton flares, which produce fake events (see Fig. 4.1). It is indeed necessary to check how extensive this contamination is for each observation in order to properly filter the data. The standard procedure requires for the creation of the good time intervals (GTIs), during which the detector count rate is lower than a certain value. This is performed by constructing the detector light curve extraction (i.e. the 10 – 12 keV observed-energy band light curve) to find the maximum count-rate threshold to filter against. The reason of this particular energy range is that the optics only poorly focus astrophysical photons above 10 keV (due to the rapid decrease of its effective area, see Fig. 2.3), therefore it is effectively dominated by the soft protons. If this light curve is proven to be fluctuating around one mean and low value,

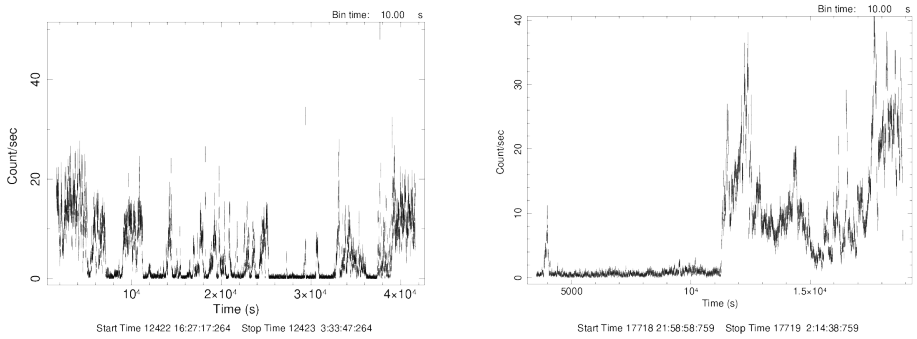

(a) 2002 data detector light curve.

(b) 2016 data detector light curve.

Figure 4.1: (a), (b): Detector light curves for the 2002 and 2016 XMM-*Newton* observations, extracted in the 10-12 keV observed energy band with a time bin size of 10s, where we expect to be dominated by spurious events produced by soft protons. As reported in the main text, (a) is flared during most of its exposure, (b) for half of its duration.

without any evident spike during the whole exposure, then the observation can be referred to as not significantly flared and not dominated by soft protons. If one or more spikes are present, the data are to be filtered either in counts, count rate or time in order to leave out those spurious events. The task `tabgtigen` selects the time intervals that correspond to the threshold given in input, creating the GTI files.
The 2002 and 2016 observations are both strongly affected by flares, whereas

the 2018 data present only a short flare at the end of the exposure. Figures 4.1(a),4.1(b) and 4.2(a) show their $10-12$ keV light curves; the 2002 is flared during the whole exposure, while the 2016 for half of its duration. The GTI threshold for the first dataset was chosen based on the SNR and the background spectra extracted from event files filtered against different thresholds, as described in the following section (Section 4.1.1), method that was applied also to the 2016 data (Section 4.1.1). Regarding the 2018 data, the selection was quite straightforward and the data were filtered against a count rate threshold of 0.9 cts/s.

The third step in the reduction process is to check for pile-up, which can occur in the case of bright sources. Pile-up is produced when two or more photons hit the same pixel in such a short amount of time that the system cannot separate the events; they are therefore recorded as one event of energy equal to the sum of that of the single photons, producing an artificial hardening of the spectrum and a reduction of the count rate, yielding a deformation of the PSF at its peak. Through the task `epatplot` we checked the importance of pile-up for the Einstein Cross and found that the source is not bright enough to be significantly affected by it.

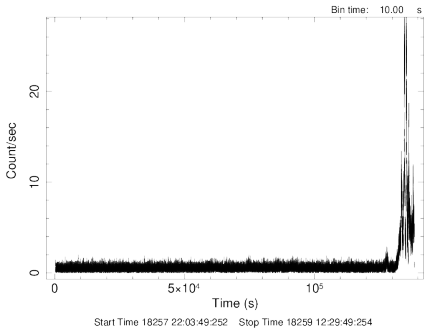

(a) 2018 data detector light curve.

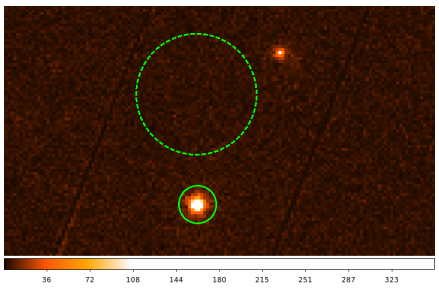

(b) 2002 image with extraction regions.

Figure 4.2: (a): Detector light curve for the 2018 XMM-*Newton* observation, extracted in the 10-12 keV observed energy band, where we expect to be dominated by spurious events produced by soft protons. The time bin size is 10s. As reported in the main text, the 2018 data show only a limited flare at the end of the observation. (b): Image of the EPIC-pn data (energy range: 0.3 – 10.0 keV) from the 2002 observation. The dashed circled is the background spectrum extraction region (80" radius), while the solid circle is the one for the source spectrum (25" radius), the distance between the centers is $\simeq$2'20".

Having calibrated and cleaned the data, the standard procedure was applied for the image production; this is done through the task `evselect`, selecting the events based on the energy range of interest (usually 0.3 – 10.0

keV[1]) and their pattern[2]. After producing the image, the source and background extraction regions are to be selected to produce both the light curves and the spectra. As for *Chandra*, one has to choose the source extraction region with a radius that includes at least 85% of the encircled energy (see Fig. 2.7), which for XMM-*Newton* corresponds to at least 25", and the background extraction region in the same CCD chip as the target, close enough to be representative of the actual background but distant enough so as not to include the photons from the source.

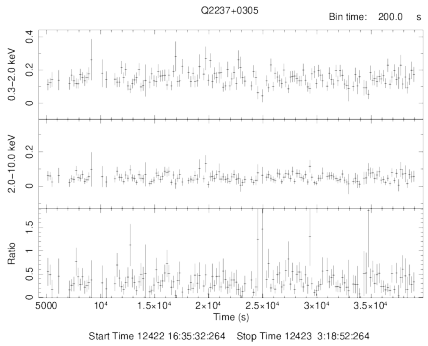

(a) 2002 data 0.3 – 10.0 keV light curve.

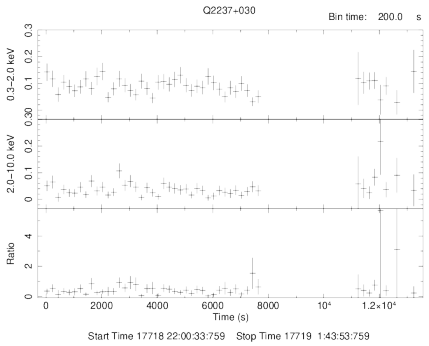

(b) 2016 data 0.3 – 10.0 keV light curve.

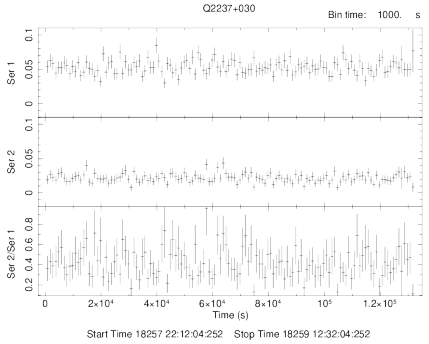

(c) 2018 data 0.3 – 10.0 keV light curve.

Figure 4.3: XMM-*Newton* 0.3 – 2.0 keV (first panel) and 2.0 – 10.0 keV (second panel) background-subtracted light curves extracted from a 25" radius source region and their ratio (third panel). (a): XMM-*Newton* 2002 data with a time bin size of 200s. (b): XMM-*Newton* 2016 data with a time bin size of 200s. (c): XMM-*Newton* 2018 data with a time bin size of 1000s.

For each observation, I used a 25" radius circle as source region (85% encir-

[1]Regarding the energy range of interest, we consider energies higher than 0.3 keV because below this energy some calibration issues might be present, while the events above 10.0 keV are not considered because of the rapid decrease of the effective area.

[2]As for *Chandra*, the photons can hit the detector in many different ways and can "light-up" more than one pixel, creating different event patterns. Only few patterns are considered valid; the actual list depends on which XMM-*Newton* instrument is of interest.

cled energy fraction) and a 80" radius circle as background region (the offset of its center with respect to the source region is approximately 2'20"); Figure 4.2(b) shows, for instance, the regions overlapped to the 2002 data 0.3 – 10.0 keV image. From Figure 4.2(b) it is evident, as expected, that XMM-*Newton* cannot resolve the quasar in its four images, therefore the analysis can only be spatially integrated.

The light curves are produced through the `evselect` task applied to the cleaned event file. Usually, two light curves are extracted: one in the soft band (0.3 – 2.0 keV) and the other in the hard band (2.0 – 10.0 keV). This is done to check whether the source shows significant variability in the two energy ranges separately and how the two bands are related to each other. To obtain the background-subtracted light curve (i.e. the source light curve), one has to extract the source+background light curve from the source region and then correct it for the background light curve (extracted from the background region) through the task `epiclccorr`. Figure 4.3 displays the 2002, 2016 and 2018 source light curves. To assess whether the source has significantly varied during the observation, each light curve from Fig. 4.3 was fitted with a constant. To do so, few bins in the 2002 and 2016 light curves were excluded because background dominated, due to the soft-p^+ flares. We consider a light curve to be significantly variable when it shows variability at more than 99.9% confidence. For the XMM-*Newton* data, all of the extracted light curves were found consistent with being not highly variable; the soft band shows a higher variability (ranging from ∼97% significance for the 2002 data to ∼82% for the 2016 data), while the hard band is more stable (variable at ∼44% confidence in 2002 and at ∼14% in 2018). Having assessed the significance of the variability during the observation, the spectra can be extracted, along with the response matrices, through the tasks `evselect`, `arfgen` and `rmfgen`.

4.1.1 Relation between SNR and GTI threshold

As mentioned above and as Figure 4.1(a) shows, the 2002 observation is highly flared during the whole exposure, therefore there is no straightforward answer when looking for the GTI threshold, either in count rate or time. For this reason, I decided to proceed as follows.
I applied six different count rate thresholds (0.6, 2.0, 5.0, 10.0, 15.0, 25.0 cts/s) and chose the one that produced the best pair of (SNR, source net counts) in the 2.0 – 8.0 keV observed-energy band (∼5.4 – 21.6 keV rest-frame energy band). I restricted the analysis to this energy range since it is where one might expect to see absorption features produced by an outflowing gas; furthermore, the effective area starts decreasing around 2 keV, while above 8 keV it drops and the quantum efficiency of the detector is not flat anymore. Operationally, I filtered the data against these six thresholds and extracted the source and background spectra for all of them, using the same extraction

regions each time (those shown in Figure 4.2(b), 25" radius for the source, 80" for the background). The SNR was calculated through the following formula, obtained from its definition (eq. (2.3)):

$$\mathrm{SNR} = \frac{\mathrm{S}}{\sigma_{\mathrm{S}}} = \frac{\mathrm{T}-\mathrm{B}}{\sqrt{\sigma_{\mathrm{T}}^2+\sigma_{\mathrm{B}}^2}} = \frac{\mathrm{T}\cdot \mathrm{S}_{\%}}{\sqrt{\mathrm{T}+\mathrm{B}\left(\frac{\mathrm{r_S}}{\mathrm{r_B}}\right)^2}} \tag{4.1}$$

where S=source net counts, T=total counts, B=background counts, $\mathrm{r_S} = 25''$, $\mathrm{r_B} = 80''$, $\mathrm{S}_{\%}$=percentage of source events in the source extraction region, $\sigma_{\mathrm{i}} = \sqrt{\mathrm{i}}$ (Poisson noise, $\mathrm{i} = \mathrm{S}, \mathrm{T}, \mathrm{B}$). The background counts are normalized to the ratio of the extraction regions, which corresponds to the squared ratio of their radii since circular regions were extracted.
Table 4.2 summarizes the properties of each trial, which correspond to rate thresholds of 0.6, 2.0, 5.0, 10.0, 15.0 and 25.0 cts/s. Figure 4.5(a) shows those values plotted versus the chosen threshold.

Table 4.2: Summary of each trial (rate thresholds of 0.6, 2.0, 5.0, 10.0, 15.0 and 25.0 cts/s) properties for the EPIC-pn 2002 data. All the values are referred to the 2.0 – 8.0 keV observed-energy band. The flux is obtained using a Galactic absorption and single power-law model.

Threshold (cts/s)	SNR	T (cts)	$\mathrm{S}_{\%}$	S (cts)	Flux (erg/cm^2/s)	Net CR (10^{-2} cts/s)
0.6	21.2	504±22	94.8	478±22	$3.31{\cdot}10^{-13}$	3.8±0.2
2.0	25.2	800±28	89.6	717±27	$3.32{\cdot}10^{-13}$	3.8±0.2
5.0	27.2	1122±33	81.8	918±30	$3.33{\cdot}10^{-13}$	3.9±0.1
10.0	27.9	1624±40	70.2	1140±34	$3.41{\cdot}10^{-13}$	3.9±0.1
15.0	28.3	2154±46	62.0	1336±37	$3.57{\cdot}10^{-13}$	4.0±0.1
25.0	29.2	2431±49	60.3	1466±38	$3.64{\cdot}10^{-13}$	4.2±0.1

This method yielded some unforeseen results. One would have expected that, decreasing the threshold, the SNR would rise, which is the exact opposite to what is displayed in Figure 4.5(a). This can be explained by the fact that when the threshold is reduced, the filtering gets stronger, the number of GTIs decreases and so do the source counts.
Another issue to take into consideration is the level of the background once the spectra are extracted. Changing the grade of flare filtering strongly affects the number of spurious events that are counted as real, hence the background spectra. In the chosen energy range, the background contribution has to be kept under control since it is where the $\mathrm{A_{eff}}$ decreases (Fig. 2.3). Figure 4.4 shows the source spectrum overlapped to the corresponding background for each trial: the latter dominates over the target signal in the

hard band for threshold 10.0, 15.0 and 25.0 cts/s, while in the case of 0.6 cts/s it is much lower, but so are also the source counts.

Thus, when deciding the best filtering approach, one needs to consider all of these aspects. I used the 5.0 cts/s threshold since it produces a good SNR (> 25), a considerable number of data counts (> 1000 counts) and the background is quite limited ($\simeq 82\%$ of the total counts in the target's extraction region are source events), as shown in Figure 4.4(c). All the following analysis of the 2002 EPIC-pn data will be performed on this spectrum.

Regarding the 2016 dataset and given its detector light curve (see Figure 4.1(b)), the most straightforward choice would seem to select the GTIs through a time-filtering approach. I did not choose for this method though, because it would have meant to directly lose the collected data during almost half of the exposure. In an attempt to make the most out of this observation, I applied the technique used for the 2002 data, iterating it six times through as many count rate thresholds: 0.6, 2.0, 5.0, 10.0, 20.0, 40.0 cts/s.

The results are summarized in Table 4.3, while the obtained source and background spectra are shown in Figure 4.6. Unfortunately, the cases where the background is not prevailing, the source has less than 250 counts in the 2.0 – 8.0 keV energy range, which means a too low statistics for this XMM-*Newton* spectrum to be meaningful and to be compared to those from the 2002 and 2018 observations (which have 1122 and 1834 net counts in this energy range respectively). Thus, given the too low spectral statistics provided by the 2016 observation, I decided not to include it in my analysis any further.

Table 4.3: Summary of each trial (rate thresholds of 0.6, 2.0, 5.0, 10.0, 20.0 and 40.0 cts/s) properties for the EPIC-pn 2016 data. All the values are referred to the 2.0 – 8.0 keV observed energy band. The flux is obtained using a Galactic absorption and single power-law model.

Threshold (cts/s)	SNR	T (cts)	$S_{\%}$	S (cts)	Flux (erg/cm^2/s)	Net CR (10^{-2} cts/s)
0.6	9.1	100±10	91.8	92±10	$2.96 \cdot 10^{-13}$	2.7±0.3
2.0	12.5	200±14	88.6	177±13	$2.66 \cdot 10^{-13}$	2.7±0.2
5.0	12.9	262±17	88.5	211±15	$2.63 \cdot 10^{-13}$	2.8±0.2
10.0	14.0	588±24	58.8	346±19	$3.13 \cdot 10^{-13}$	3.4±0.2
20.0	13.5	856±29	47.4	408±20	$3.04 \cdot 10^{-13}$	3.3±0.2
40.0	13.6	1110±33	42.0	466±22	$3.19 \cdot 10^{-13}$	3.5±0.3

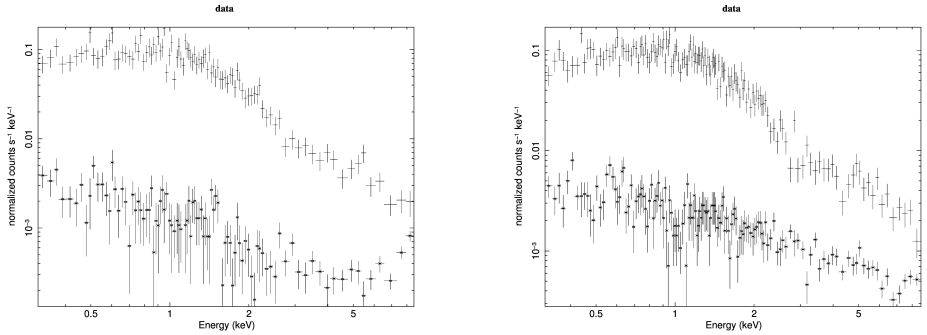

(a) Threshold = 0.6 cts/s.

(b) Threshold = 2.0 cts/s.

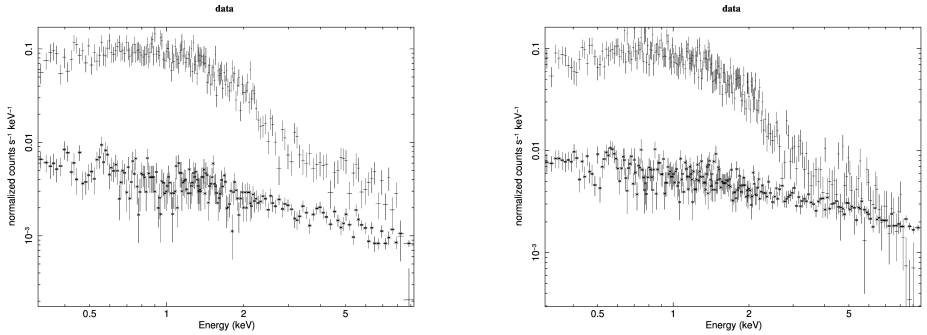

(c) Threshold = 5.0 cts/s.

(d) Threshold = 10.0 cts/s.

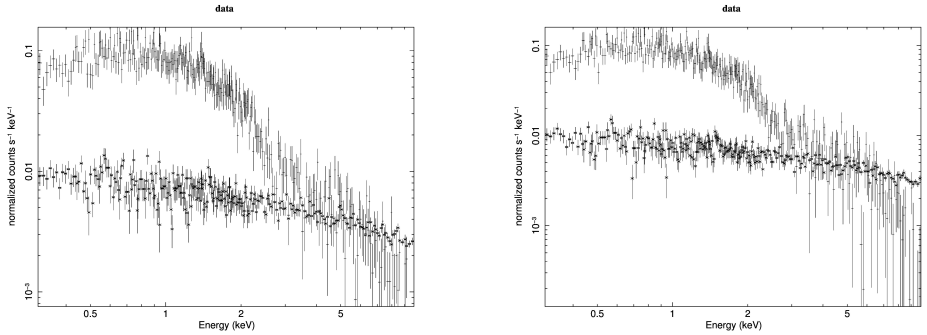

(e) Threshold = 15.0 cts/s.

(f) Threshold = 25.0 cts/s.

Figure 4.4: Background-subtracted source (crosses) and only background (stars) spectra ($\geq$ 20 cts per bin) for each count rate threshold trial over the 2002 EPIC-pn data. The energy range where the background intercepts and then dominates the source spectrum is where it is important to check for the significance of the data (i.e. SNR).

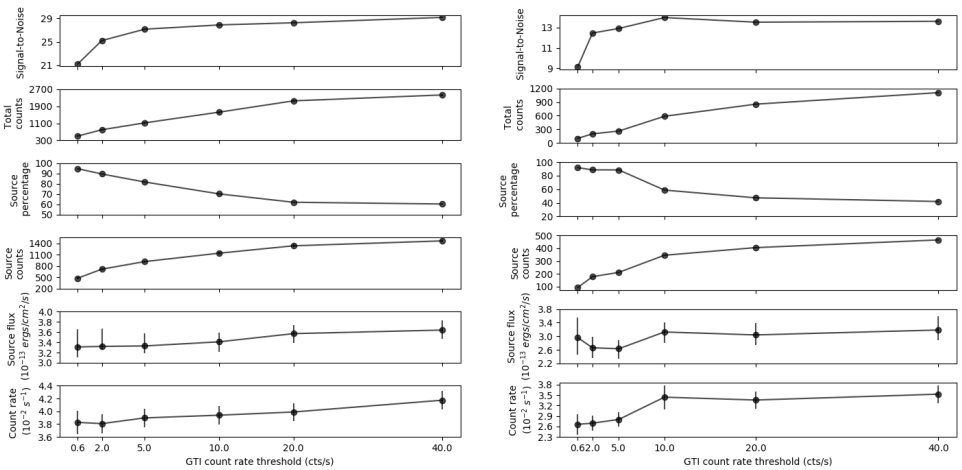

(a) 2002 data (b) 2016 data

Figure 4.5: (a): SNR, total counts, source percentage, source counts, source flux and net count rate as a function of the adopted GTI threshold for the 2002 EPIC-pn data. The source and total counts error bars are contained in the dots. (b): Same graphs as (a) for the 2016 EPIC-pn data.

4.2 Spectral analysis of the XMM-Newton data

The spectra were binned at more than 20 cts/bin and, given the high number of counts, a minimum energy width of the bins was selected in order not to oversample the instrument resolution: the lowest width was set to one third of the CCD resolution at the center energy of the bin through the task `specgroup`. Table 4.4 summarizes the properties of the two spectra.

Table 4.4: Basic information of the XMM-*Newton* spectra in the 0.3 – 10.0 keV band.

Observation ID	Date	Nominal Exposure (s)	Cleaned Exposure (s)	Net Counts	Net CR (10^{-2} cts/s)
0110960101	2002-05-28	42870	23530	3837	16.3±0.3
0823730101	2018-05-19	141600	108000	6569	6.0±0.1

The detailed spectral analysis will be presented in the next sections, first for the 2002 data, then for the 2018 observation. For both epochs, I focused on assessing which models best reproduced the two spectra, with particular attention to reflection and complex absorption models, bearing in mind the results obtained from the *Chandra* high-statistics sample analysis.

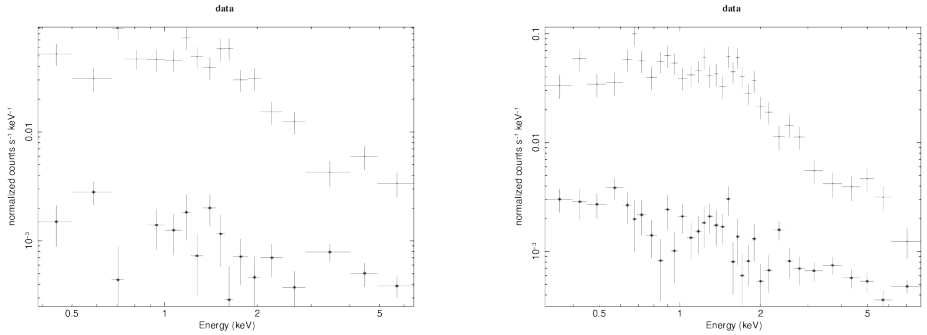

(a) Threshold = 0.6 cts/s.

(b) Threshold = 2.0 cts/s.

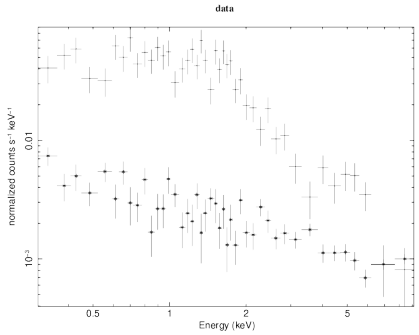

(c) Threshold = 5.0 cts/s.

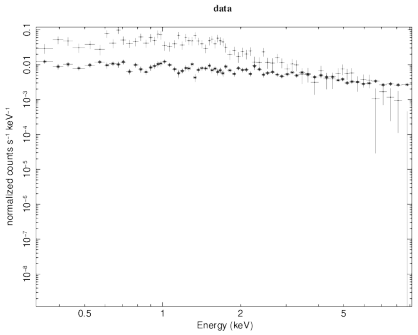

(d) Threshold = 10.0 cts/s.

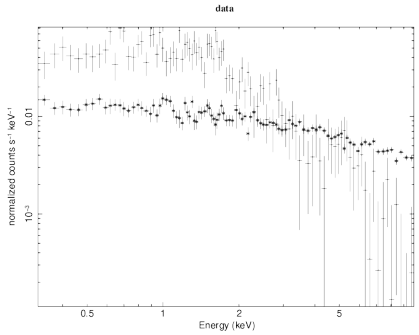

(e) Threshold = 20.0 cts/s.

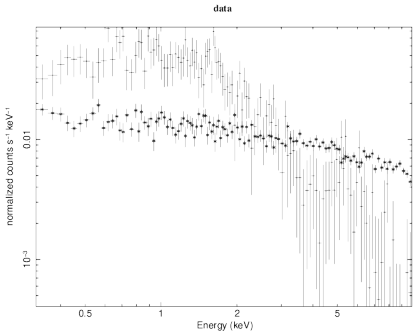

(f) Threshold = 40.0 cts/s.

Figure 4.6: Background-subtracted source (crosses) and only background (stars) spectra ($\geq$ 20 cts per bin) for each count rate threshold trial over the 2016 EPIC-pn data. The energy range where the background intercepts and then dominates the source spectrum is where it is important to check for the significance of the data (i.e. SNR).

4.3 Spectral analysis of the 2002 data

As for the *Chandra* data, the first approach to the spectral analysis was to fit it with a single power-law model plus Galactic absorption (hereafter referred as Model 0: `phabs*zpowerlw`). The rest-frame best-fit residuals are displayed in Figure 4.7 (best-fit slope: $\Gamma = 1.67 \pm 0.04$); they show absorption complexities both in the soft- and hard-energy bands, in particular in the 1.0 – 1.5 keV range and between 7.0 and 10.0 keV. In the 5.0 – 6.0 keV energy range the residuals seem to indicated the presence of an emission line; some excess is found also in the 3.0 – 4.0 keV range. From this simple modeling of the continuum, hints of two narrow absorption lines in the hard band stand out, one at ~ 7.4 keV and the other at ~ 11.8 keV. Moreover, above 10 keV the residuals show an increasing trend up to 20 keV that could be interpreted as a hint of reflection component, despite few negative residuals, which might indicate the presence of some absorption lines.

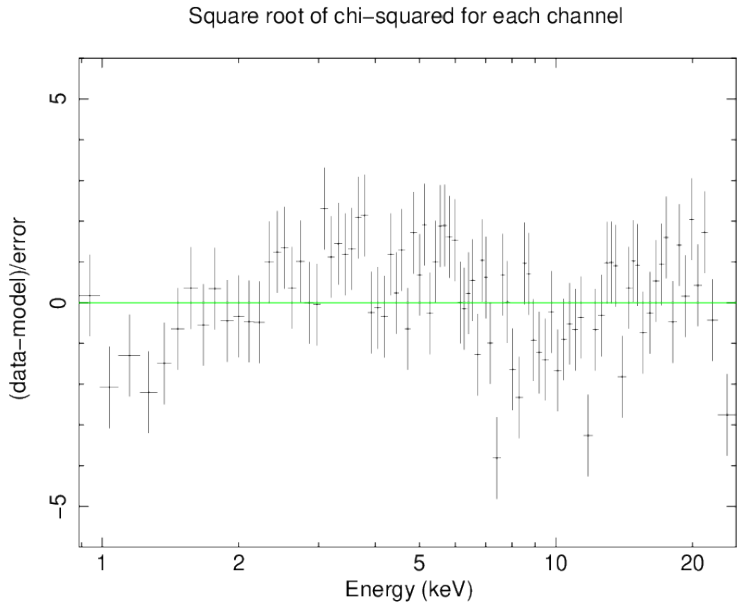

Figure 4.7: 2002 rest-frame best-fit residuals of a Galactic absorption and single power-law model. As discussed in Section 4.3, they show a deficit of counts below 1.5 keV, some excess in the 2.5 – 6 keV range and indicate the presence of a narrow absorption line between 7 and 8 keV.

The overall trend of the residuals indicates that a single power-law is a too simple model to reproduce the data at best. Given the shape of the residuals in the soft band, I started from the addition of an absorption component, using both cold and ionized models, in order to find which gas phase reproduced this spectrum at best. Having assessed the feasible absorption, given the rise of the residuals at high energies, I investigated the possibility of a

reflection component.

4.3.1 Complex-absorber models: `warmabs`

I assessed the significance yielded by the addition of an absorption component, beginning from the less complex modeling: photoelectric absorption produced by a cold material of Solar abundances (`zphabs`), the same used for the high-statistics sample. Given the variability inferred from *Chandra* data (see Section 3.3.1), all the extra absorption components with respect to the Galactic one were placed at the redshift of the quasar. This is the simplest absorber available since, having set its redshift, it adds only one parameter (the column density) to the pre-existent model and, being neutral, completely absorbs all the flux below a certain threshold energy, determined by its column density. The variation in the model induced by different column densities is displayed in Figure 4.8.

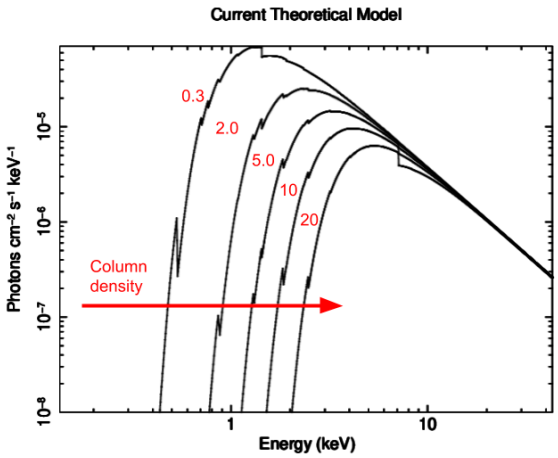

Figure 4.8: Superposition of Model 1 (`phabs*zphabs*zpowerlw`) spectra at varying column densities; as indicated by the red arrow, the column density increases from left to right ($N_H = 0.3,\ 2.0,\ 5.0,\ 10.0,\ 20.0 \times 10^{22}$ cm^{-2}).

This additional absorption turned out to be significantly requested by the data: the resulting column density is $N_H = 0.33^{+0.12}_{-0.12} \times 10^{22}$ cm^{-2} (see Table 4.5), yielding a $\Delta\chi^2 = 25$ for the addition of one parameter ($> 99.99\%$ confidence). The best-fit residuals (Model 1: `phabs*zphabs*zpowerlw`) are shown in Figure 4.10; as displayed, Model 1 produces a good representation of the data in the soft band, leaves the hard band almost unchanged with respect to Model 0 (Fig. 4.7). While with the *Chandra* spectra the aim was to assess whether a generic absorption could be present and, possibly, varying in time, the XMM-*Newton* data, thanks to its unprecedented counting statistics, allows us to explore the use of more complex absorption models, and to investigate their significance. In particular, I explored three different

possibilities: i) the absorption is only partially covering the source flux; ii) the absorber is ionized; iii) both of the previous cases. Case i) corresponds to a material that does not completely cover the source, allowing part of it to be seen directly; an ionized absorber instead (case ii) only absorbs part of the incoming flux at low energies because the less energetic transitions are those corresponding to the first ionization levels; case iii) corresponds to an ionized material that covers only a portion of the source flux, while the remaining is seen directly. Figure 4.9 show the variation in the model induced by changing the covering factor for a neutral medium of equal N_H (left panel) and that induced by changing the ionization parameter for a medium of equal N_H and covering factor (right panel).

Table 4.5: Summary of the best-fit parameters for each tested absorption model. The numbering corresponds to those reported in the main text. The column density is given in units of 10^{22} cm^{-2}, while the ionization parameter is in units of erg s^{-1} cm. The $\Delta\chi^2$ is computed with respect to Model 0 ($\chi^2 = 143.9, \nu = 88$).

#	Γ	N_H	CF	logξ	z_{abs}	$\Delta\chi^2$	$\Delta\nu$
0	$1.67^{+0.04}_{-0.04}$	–	–	–	–	–	–
1	$1.83^{+0.12}_{-0.12}$	$0.33^{+0.12}_{-0.12}$	–	–	1.695	25.3	1
2	$1.95^{+0.11}_{-0.11}$	$2.07^{+1.26}_{-1.11}$	$0.52^{+0.09}_{-0.11}$	–	1.695	32.4	2
3	$1.90^{+0.12}_{-0.04}$	$3.00^{+2.20}_{-2.14}$	$0.48^{+0.18}_{-0.11}$	$1.09^{+0.80}_{-1.09}$	1.695	27.1	3
4	$1.83^{+0.04}_{-0.04}$	$20.9^{+6.3}_{-4.9}$	–	$3.02^{+0.09}_{-0.01}$	$\simeq 1.448$	40.7	3

The first case was investigated through a partial covering cold absorber (Model 2: `phabs*zpcf*zpowerlw`); one free parameter, the covering fraction (CF), returns the fraction of absorbed flux with respect to the total produced by the source, which can roughly be computed as the ratio of the flux intensities. The significance of this component turned out to be lower than that of `zphabs`: Model 2 produced a $\Delta\chi^2 = 32.4$ for the addition of two parameters (best-fit values: $N_H = 2.07^{+1.26}_{-1.11} \times 10^{22}$ cm^{-2} and covering fraction CF $= 0.52^{+0.09}_{-0.11}$, see Table 4.5), compared to $\Delta\chi^2 = 25$ for the addition of only one parameter of Model 1. Therefore, on a statistical basis, Model 2 gives a slightly worse overall representation of the data than Model 1, even though the soft-end range shows very similar residuals (Fig. 4.10).
The variation in column density between Model 1 and 2 is to be assigned to the different geometry of the absorber; since it absorbs at maximum 61% of the incoming flux instead of 100%, it has to be thicker than that in Model 1 to produce the same phenomenological outcome. To be noticed is the fact that, with respect to Model 0, both Model 1 and 2 produced no variations in the hard-energy band residuals, which still show a prominent narrow absorption feature ($7 - 8$ keV) and other complexities above 9 keV. Given the energies of these features, they could be ascribed to (highly) ionized material intercepting the line of sight. For this kind of absorption, among the standard

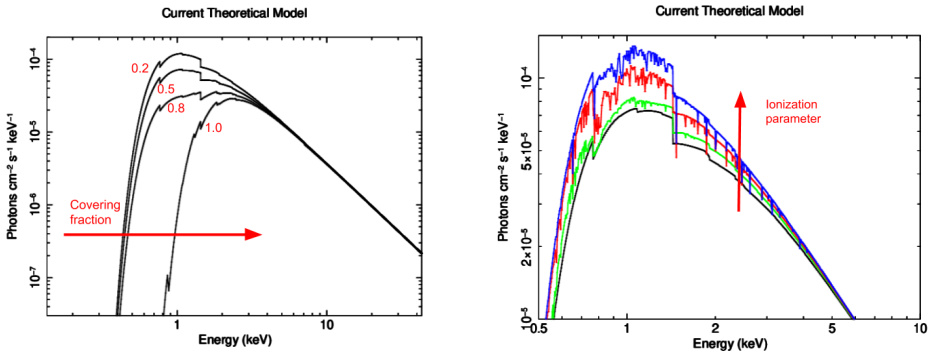

(a) Varying covering factor. (b) Varying ionization parameter.

Figure 4.9: (a): Superposition of Model 2 (`phabs*zpcf*zpowerlw`) spectra at varying covering factor. The column density is set to $N_H = 2.0 \times 10^{22}$ cm^{-2}. As indicated by the red arrow, the CF grows from left to right (CF = 0.2, 0.5, 0.8, 1.0). (b): Superposition of Model 3 (`phabs*zxipcf*zpowerlw`) spectra at varying ionization parameter.The column density is set to $N_H = 2.0 \times 10^{22}$ cm^{-2} and the covering factor to CF = 0.5. Black, red, green, blue line indicate $\log(\xi/\text{erg s}^{-1}\text{cm}) = 0,\ 1,\ 2,\ 3$, respectively.

models available in the latest release of `XSPEC`, the most reliable is `zxipcf`. It uses a grid of `XSTAR` photoionized absorption models, which assume a source of ionizing photons with a spectral energy distribution that is typical for an AGN, a microturbulent velocity for the absorbing gas of 200 km/s, and then considers the material as partially covering the source (Reeves et al., 2008). This absorption is parameterized through column density, ionization parameter ($\log\xi$, in units of erg s^{-1}cm), covering fraction and redshift. Having set the latter to the systemic redshift of the Einstein Cross, the additional free parameters are three. Model 3[3] best-fit parameters for column density and covering fraction are consistent with those of Model 2 within their 90% errors, while the ionization is $\log\xi \leq 1.89$ (erg s^{-1} cm). Besides yielding the least improvement ($\Delta\chi^2 = 27$ for three additional parameters) with respect to Model 1 and 2, Model 3 produces non-continuous confidence contours in the parameter spaces of (N_H, ξ), (N_H, Γ) and (N_H, CF), indicating that the parameters are not actually constrained, probably due to the complexity of the calculation performed by the model.
Figure 4.10 shows the comparison between Model 1 (bottom panel), Model 2 (central panel) and Model 3 (top panel). Indeed, there is almost no difference among the residuals of the three cases, except for few bins below 2 keV, and the absorption features in the hard band are visible in any case. For this reason, I decided to search for a more precise model for ionized absorption and found it in the `XSTAR` model `warmabs` (Kallman and Bautista, 2001). Unlike `zxipcf`, which uses grids of precalculated tables, this is an analytic model

[3]Model 3: `phabs*zxipcf*zpowerlw`.

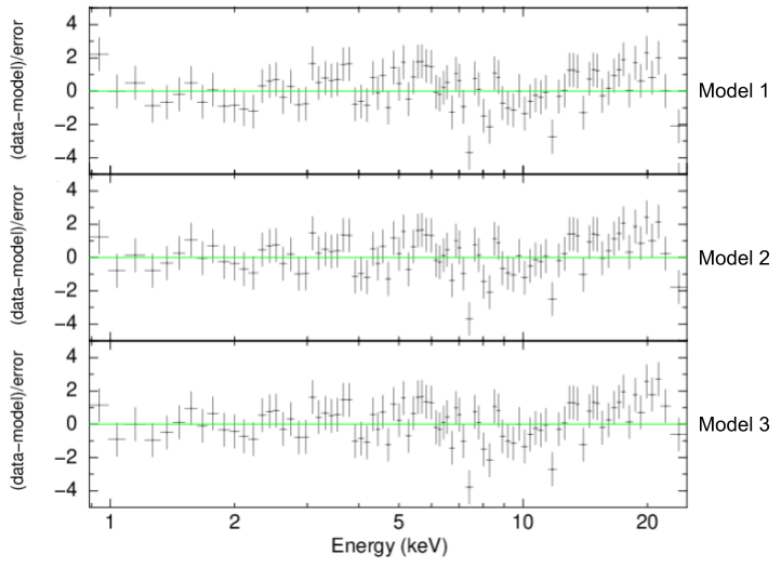

Figure 4.10: 2002 rest-frame best-fit residuals derived from using a model with Galactic absorption, single power-law model and extra absorption parameterized through three different components: `zxipcf` (top panel, Model 3), `zpcf` (central panel, Model 2), `zphabs` (bottom panel, Model 1).

of self-consistent absorption produced by a partially photoionized material, where the AGN emission modelled in `XSPEC` ionizes the same gas that absorbs its spectrum. The code loads from an external file the initial properties of the material (abundances and density) and the ionizing spectrum (power-law slope) to compute the actual absorber optical depth at varying energy, which can be later rescaled if the user sets different abundances. I used the population corresponding to a gas with solar abundances, a 10^4 cm^{-3} density and a $\Gamma = 2$ power-law slope. Furthermore, it includes self-consistent absorption lines, which are stored alongside all their properties in a FITS file. Figure 4.11 shows the superposition of Model 4 (`phabs*warmabs*zpowerlw`) for a total covering medium of $N_H = 2.0 \times 10^{22}$ cm^{-2} and varying ionization parameter; to be noticed is that higher ionization states produce less absorption lines. This model is highly complex and comprises many parameters; of these, only the column density, the ionization parameter and the redshift were allowed to vary in my analysis, since I assumed solar abundances and set the gas turbulent velocity to 5000 km/s (typical for the Broad Line Region). The possible absorption lines above 7 keV (rest-frame) show energies that could be interpreted as blueshifted iron resonant lines, therefore the absorber redshift was not set to that of the quasar to test whether an outflowing material were present in Q2237+030. Figure 4.12 shows the best-fit spectrum and the corresponding residuals for Model 4. The best fit ($\Delta\chi^2 = 40.7$ for three additional parameters) yielded an

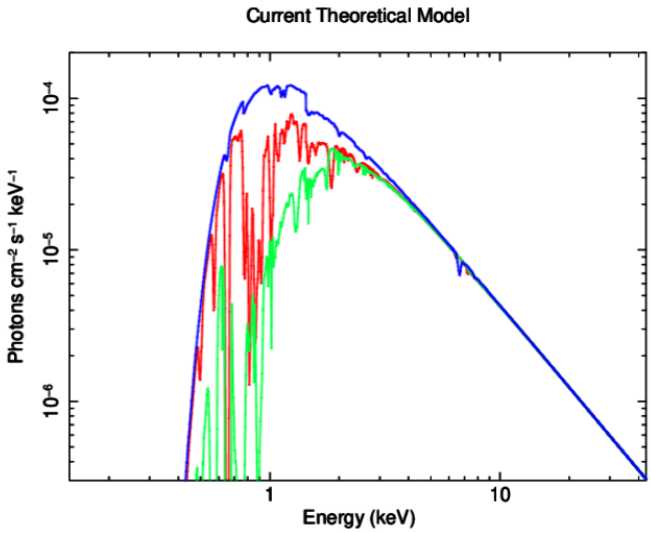

Figure 4.11: Superposition of Model 4 (`phabs*warmabs*zpowerlw`) spectra at varying ionization parameter.The column density is set to $N_H = 2.0 \times 10^{22}$ cm^{-2} and the covering factor to CF = 0.5. Green, red, blue line indicate $\log(\xi/\mathrm{erg\ s^{-1}cm}) = 1,\ 2,\ 3$, respectively.

ionized absorber of $N_H = 2.09^{+0.63}_{-0.49} \times 10^{23}$ cm^{-2}, $\log\xi = 3.02^{+0.09}_{-0.01}$ erg s^{-1}cm and $z \simeq 1.448$ The outflow velocity can be determined as follows. The model returns the observed value (z_o) of the absorber redshift, that is related to the intrinsic redshift z_a of the medium (i.e. in the source rest frame) as $(1 + z_o) = (1 + z_a)(1 + z_q)$. One can compute the outflowing velocity v_{out} from the relativistic Doppler effect formula: $1 + z_a = [(1 - \beta)/(1 + \beta)]^{0.5}$, where $\beta = v_{out}/c$. Given $z_q = 1.695$, $z_o \simeq 0.1c$ corresponds to an outflowing velocity of $v_{out} = 0.10^{+0.01}_{-0.01}$ c. In addition, as shown by Fig. 4.12, this outflowing wind model also reproduces the absorption line at $E \simeq 7.4$ keV (rest-frame); given the ionization state and the outflowing velocity of the absorber, this line is consistent with being dominated by Fe XXV (rest-frame energy of the Kα transition: 6.7 keV).

I added a `zgauss` absorption component to Model 1 (Model 1.1: `phabs*zphabs*(zpo+zga)`), since it is the one that provides the best representation of the data, when limiting the modeling to `XSPEC` standard components. This yielded a $\Delta\chi^2 = 38.7$ for the addition of three parameters with respect to Model 0, of which the only line component accounts for $\Delta\chi^2 = 13.4$ for the addition of two parameters. Compared to the statistical improvement produced by the `warmabs` component (Model 4), Model 1.1 returns a representation of the data that is almost as good. The difference between the two modelings is that Model 4 naturally explains the absorption line as produced by the same material that absorbs the source flux, while for Model 1.1 a less straightforward explanation would be required. On the basis of this last argument, the best representation of the 2002 data can be

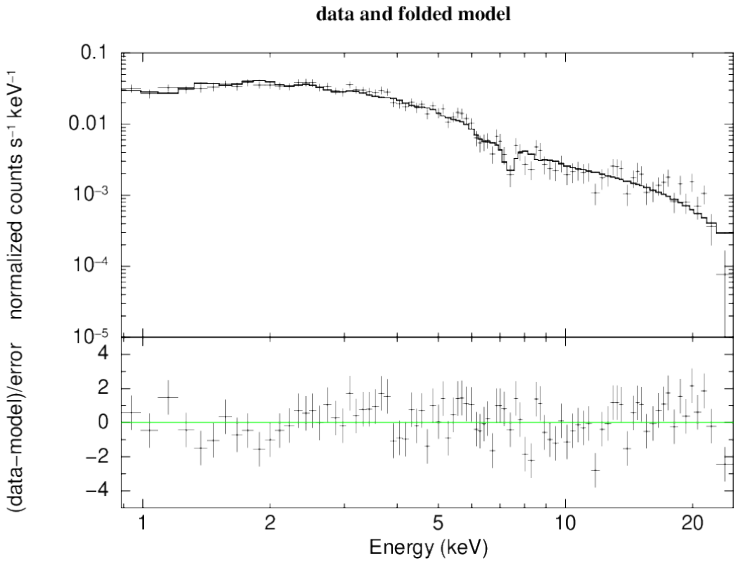

Figure 4.12: 2002 rest-frame best-fit residuals of Model 4 (`phabs*warmabs*zpo`).

addressed to Model 4. All the best-fit parameters of each model are summarized in Table 4.5. In conclusion, when investigating the possibility of an absorption component, the best modeling is obtained through a rather thick ($N_H \simeq 2 \times 10^{23} cm^{-2}$), highly ionized absorber $\log\xi \simeq 3$ erg s^{-1}cm, outflowing at v $\sim$ 0.1 c. However, this best-fit model fails to explain the narrow absorption line at $\sim$ 11.8keV.

Given the little excess still shown by the residuals between 5 and 6 keV (Fig. 4.12), I added a narrow emission line to the model to assess the significance of this component (Model 4.1: `phabs*warmabs*(zpowerlw+zgauss)`). This turned out to be a marginally detected emission line placed at E = 5.7 $\pm$ 0.2 keV ($\sim$ 90% confidence), that could be interpreted as a microlensed FeKα line since it is consistent with what found in Dai et al. (2003).

4.3.2 Reflection models: `pexrav`

Another possible explanation for the remaining residuals at high energies shown in Figures 4.7 – 4.12 is the presence of a reflection component, which is usually associated to the FeKα emission line at E = 6.4 − 6.7 keV, depending on the ionization state. Here the only possible, but marginal, emission line is found at E $\simeq$ 5.7 keV (rest-frame). For this reason, self-consistent reflection models that include the FeKα emission would not be appropriate for this spectrum. Thus, I chose to model the reflection component with a cold accretion disk (`pexrav`) plus a narrow emission line (Model 5: `phabs*(zpowerlw+pexrav+zgauss)`); the reflected power-law was set to the intrinsic emission, the abundances equal to Solar, the inclination angle to

45° and the cutoff energy to 300 keV[4]. This model yielded a $\Delta\chi^2 = 14.5$ for three additional free parameters (fraction of reflected AGN emission with respect to the direct emission, line energy and intensity), which means that the improvement with respect to Model 0 is at 97% confidence; the best-fit continuum is flat ($\Gamma = 1.66 \pm 0.04$), while the best-fit reflected fraction (R) is consistent with zero, which would mean that this component is not required by the data. The line is detected at $E = 5.69 \pm 0.13$ keV with 99% confidence. Given the analysis carried out using the *Chandra* spectra and that described in the previous section, the relatively flat power-law slope and the fact that the residuals ($\leq$ 2 keV) show the same structure as that of Model 0, I investigated whether the addition of an absorption component to Model 5 would had improved the representation of the data.

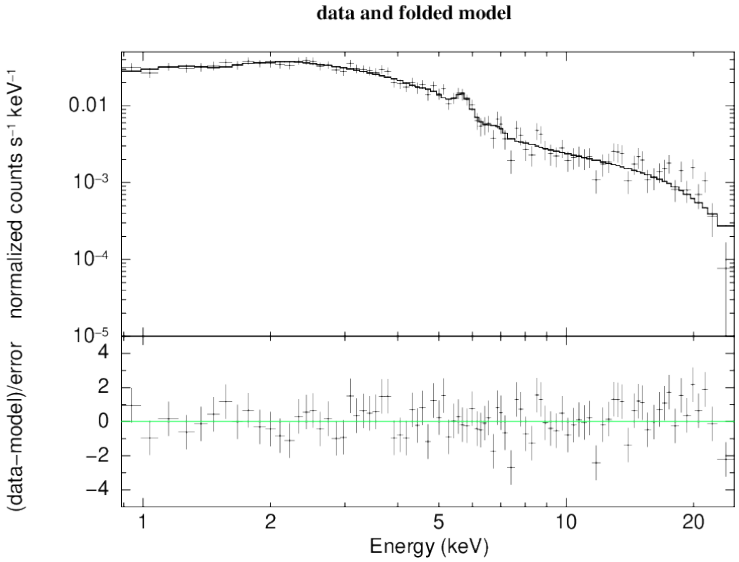

Figure 4.13: 2002 best-fit residuals of Model 6.2, which comprises Galactic absorption, partially covering cold absorption at the quasar redshift, power-law, reflection component, an emission line (`phabs*zpcf*(zpowerlw+pexrav+zgauss)`).

From the analysis in Section 4.3.1 we know that the best absorption modeling involves an outflowing ionized absorber but, given the already inherent complexity of the reflection model, I chose to test this possibility through a less complicated model: firstly a total covering cold absorber (Model 6.1: `phabs*zphabs*(zpowerlw+pexrav+zgauss)`), secondly a partial covering cold absorber (Model 6.2: `phabs*zpcf*(zpowerlw+pexrav+zgauss)`). The addition of the absorption turned out to be highly significant in both cases, but Model 6.2 is the one that best reproduces the data, both on a statistical basis ($\Delta\chi^2 = 26.2$ for $\Delta\nu = 2$ and $\Delta\chi^2 = 43.4$ for $\Delta\nu = 3$ for Model

[4]The cutoff energy is thought to be higher than 100 keV; when the energy range of the spectrum is too limited to contain it, it is usually set at this value or above.

6.1 and 6.2, respectively) and phenomenologically, since it accounts for a partial absorption of the soft-energy radiation (see Section 4.3.1). The emission line is still detected at the same energy and confidence as before.

Focusing on the best-fit parameters, Model 6.2 yielded $R = 0.62^{+0.43}_{-0.31}$ and $\Gamma = 2.65^{+0.31}_{-0.34}$, which is a steep power-law, at the limits of the expected values for an AGN (Ghisellini et al., 1994; Piconcelli et al., 2005). The emission line is detected at $E = 5.69^{+0.18}_{-0.16}$ keV at more than 99% confidence, with an equivalent width of $EW = 154^{+99}_{-103}$ eV; following Makishima (1986) and Leahy (2001), it is in accordance to what expected given the reflection fraction R. As mentioned in the previous section, this line could be explained as a micro-lensed FeKα and its energy is consistent to that detected by Dai et al. (2003), with the difference that in my analysis it is consistent with being narrow, since even letting its energy width vary it remains lower than the CCD energy resolution.

The residuals in Fig. 4.13 still show a narrow absorption feature just above 7 keV; I assessed its significance by adding a narrow absorption `zgauss` component (Model 7: `phabs*zpcf*(zpo+pexrav+zga+zga)`). Its best-fit produced a $\Delta\chi^2 = 6.6$, resulting in a marginally detected absorption narrow line ($\sim 96\%$ confidence), consistent with the need of a ionized absorber (see previous Section).

The best fit for Model 6.2 yielded quite a steep power-law. This could be due to the possible degeneracy among the absorption and the spectral shape of the continuum. To break such degeneracy, the photon index was set to the standard value of $\Gamma = 1.90$ (Haardt and Maraschi, 1991, 1993; Nandra and Pounds, 1994; Perola et al., 2002; Cappi et al., 2006; Dadina, 2008), that is also consistent to the average photon index of the *Chandra* data and that of the absorption models for this spectrum (see Table 4.5). When doing so, the quality of the best fit decreases ($\Delta\chi^2 = 25.4$ for $\Delta\nu = 3$ and $\Delta\chi^2 = 10.6$ for $\Delta\nu = 2$ for Model 6.2 with free slope and set slope, respectively) and the reflection fraction becomes consistent with zero ($R < 0.14$). Therefore, the reflection component turns out not to be required by the 2002 data when imposing a typical power-law slope for an AGN. The fact that setting a flatter power-law produces a smaller reflection fraction is not surprising, since the two parameters are degenerate (Perola et al., 2002), especially when limiting the analysis to small energy ranges as in the analysis carried out in this work.

4.4 Spectral analysis of the 2018 data

The procedure applied to analyze the 2018 EPIC-pn spectrum was the same used for the 2002 data. First, I inspected the residual distribution of single power-law model plus Galactic absorption (Model 0: `phabs*zpowerlw`), second I assessed the presence of an absorber (through different modelings), third the significance of a possible reflection component was investigated.

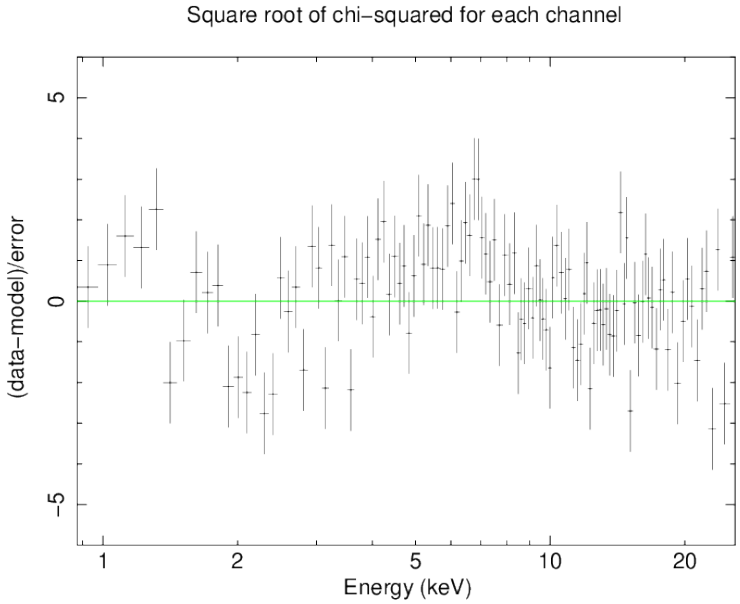

Figure 4.14: 2018 best-fit residuals of a Galactic absorption and single power-law model. As discussed in Section 4.4, they show clear complexity over the whole band, in particular Model 0 overestimates the data in the $1.5-2.5$ keV range and the residuals strongly indicate an emission line below 7 keV.

Figure 4.14 shows the best-fit residuals of Model 0 (best-fit slope: $\Gamma = 1.58 \pm 0.03$). This spectrum presents complexities both in the soft- and hard-energy bands, indicating that also for the 2018 data that a single power-law model is way too simplistic. The model seems also to underestimate the spectrum around 1.5 keV, while between $1.5-2.5$ keV hints of absorption can be seen. Just below 7 keV, the residuals indicate the presence of an evident emission line; at high energies, however, the distribution is quite flat, even though noisy, suggesting the absence here of a reflection component. No hints of absorption lines in the hard-energy band are seen either.

Model 0 best-fit residuals for the 2018 data (Fig. 4.14) are quite different with respect to those of the 2002 data (Fig. 4.7), suggesting that the source has varied in the 16 years elapsed between the two observations. To support this hypothesis, I divided the 2018 spectrum by that of the 2002 to investigate how this variation took place and whether it can be considered differential in energy. Figure 4.15 displays the ratio of the two spectra in the observed-energy range; the binning is set at more than 20cts/bin and differential in energy to consistently compare these two source spectra). Each bin shows a value that is lower than unity, which indicates that the total source brightness has reduced between the two dataset as expected (see count rates in Table 4.4). When fitting with a constant, the ratio is found significantly variable ($> 99\%$ confidence). Given the noise shown by the last bins, I fitted the ratio

excluding the last five bins. Even in this case the ratio was found variable at more that 99% confidence. Thus the source varied both in its total flux and in its spectral shape between the two epochs.

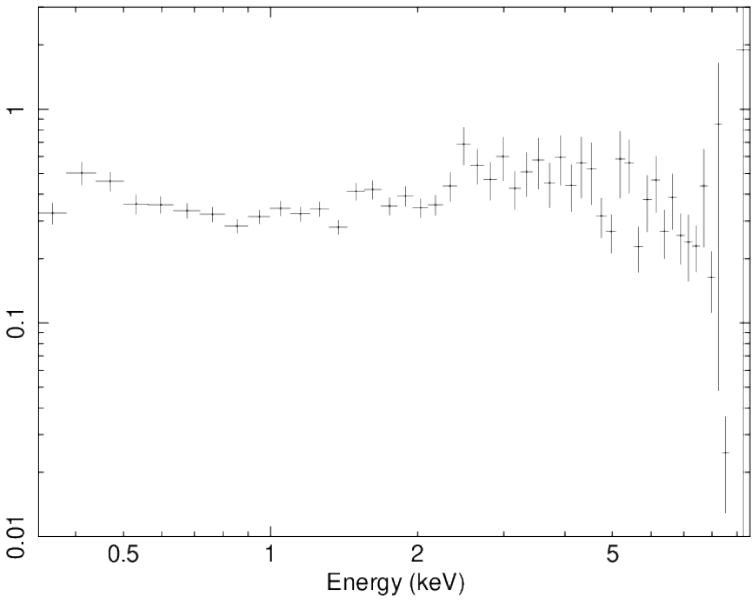

Figure 4.15: Ratio of the 2018 over the 2002 spectral data. As discussed in Section 4.4, the source shows a lower overall flux in the 2018 epoch ($F_{2018} \simeq 40\%$ F_{2002} over the entire energy range).

4.4.1 Complex-absorber models

Given the distribution of the residuals in the soft band, an absorption component seems to be required by the data. The trend shown by the residuals below 3 keV is probably a hint of either a partial covering neutral material or an ionized absorber or both. As for the 2002 data, for all the following analysis the redshift of the absorber has been set to that of the quasar, based on the same argument discussed in Section 4.3.1.

In order not to exclude any possibility a priori, I started with a total covering material (Model 1: `phabs*zphabs*zpowerlw`), which, as just speculated, was clearly not required by the data ($\Delta\chi^2 = 0$, best fit column density consistent with zero). I then assessed the significance of a partial covering neutral material (Model 2: `phabs*zpcf*zpowerlw`); this model yielded a $\Delta\chi^2 = 56$ for the addition of two parameters and best-fit values of $N_H = 1.14^{+0.25}_{-0.22} \times 10^{23}$ cm^{-2} and $CF = 0.57^{+0.07}_{-0.08}$. I then investigated the possibility of an ionized absorber, through the `zxipcf` component (Model 3: `phabs*zxipcf*zpowerlw`). This turned out to be quite significant ($\Delta\chi^2 = 46.6$ for the addition of three parameters), but it yielded non-

continuous contours in the parameter spaces, as for the 2002 data, possibly due to the complexity of the model. Furthermore, the statistical improvement in the best fit is more limited with respect to that of Model 2.

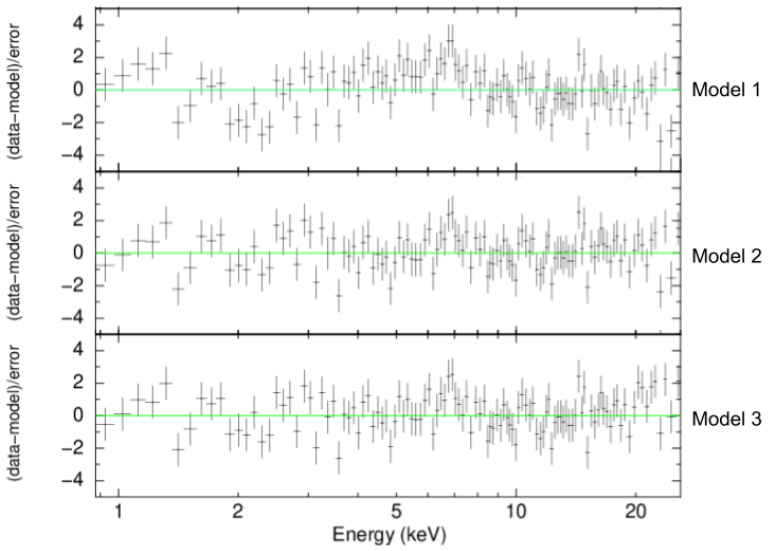

Figure 4.16: 2018 best-fit residuals derived from using a Galactic absorption, single power-law model and extra absorption parameterized through three different components: `zxipcf` (top panel, Model 3), `zpcf` (central panel, Model 2), `zphabs` (bottom panel, Model 1).

Figure 4.16 shows the comparison between the best-fit residuals of the three models. The bottom panel displays the residuals yielded by Model 1, which are identical to those of Model 0, confirming that a cold total covering absorber is not required by the 2018 data. Moreover, the residuals of Model 2 and Model 3 are different with respect to those of Model 0, but quite similar when comparing one another.

Based on the best-fit residuals and the statistical significance of each modeling, the one that better reproduces the 2018 data is Model 2; thus, when limiting the analysis to a feasible absorption component, the 2018 spectrum is consistent with a partial covering cold material.

Given the similarities among the residuals of Model 2 and Model 3, I evaluated the upper limit of the ionization state through `warmabs`, since, as said, it is a more physically grounded warm absorption modeling than `zxipcf`. To mimic the partial covering, the model included two power-law components, one as seen directly and the other as scattered in the absorber (Model 4: `phabs*(zpo+warmabs*zpo)`). Their slopes were set to be equal, since the primary emission is the same for both components. However, their normalizations were not forced to be equal given the covering factor yielded by Model 2 best fit. The 90% upper limit of the ionization parameter inferred

with this procedure was log$\xi \leq 2.1$ erg s^{-1}cm.

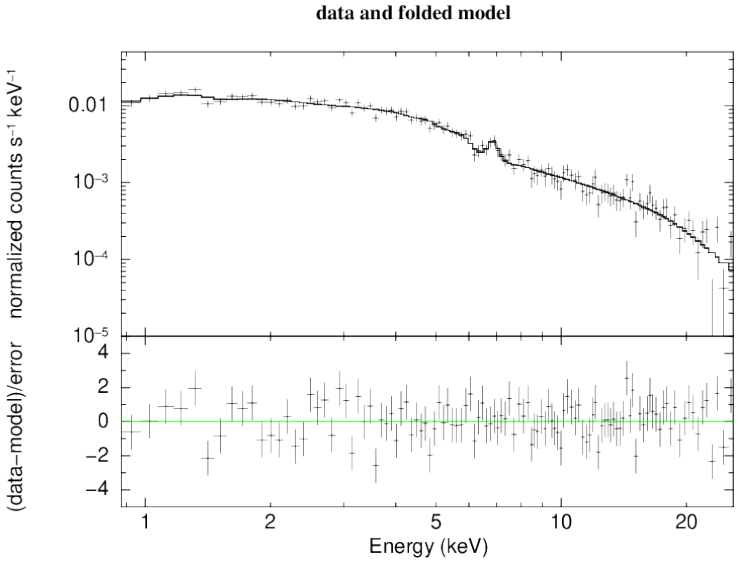

Figure 4.17: 2018 best-fit residuals and spectrum of Model 2.1: Galactic absorption, partial covering cold absorption at the redshift of the quasar, power-law and narrow emission line (`phabs*zpcf*(zpowerlw+zgauss)`).

All the residuals shown in Figures 4.14 and 4.16 strongly indicate the presence of an emission line just below 7 keV, therefore I assessed its significance and properties by adding a narrow emission line component to Model 2 (Model 2.1: `phabs*zpcf*(zpowerlw+zgauss)`). This feature turned out to be highly significant: it yielded a $\Delta\chi^2 = 15.3$ for the addition of two parameters with respect to Model 2 ($\Delta\chi^2 = 71.3$ with respect to Model 0), which means a 99.8% confidence (evaluated through the F-test). Figure 4.17 displays the best-fit spectrum and residuals of Model 2.1. The line best-fit energy is $\mathrm{E} = 6.84^{+0.11}_{-0.10}$ keV and shows an equivalent width of $\mathrm{EW} = 267^{+110}_{-111}$ eV. Following Makishima (1986), the ionization parameter (log$\xi \leq 2.1$ erg s^{-1}cm) determined for the absorber translates to a material that is dominated by iron from Fe I to Fe XX, whose FeKα energies are lower than $\simeq 6.5$ keV. This detected emission line would be consistent, within its errors, with being dominated by Fe XXV-XXVI which, however, would require a much more ionized gas than what found for this dataset (log$\xi \approx 3$ erg s^{-1}cm). Another possible explanation for such line could be the micro-lensing differential magnification of a relativistic blurred FeKα produced by the reflection over the accretion disk (see Section 4.4.2). Furthermore, the energy of this line is inconsistent to that of the marginal emission line in the 2002 data, but it is consistent to the emission line detected by Reynolds et al. (2014) in the stacking of the *Chandra* data (ObsIDs from 431 to 14514).

Table 4.6: Summary of the best-fit parameters for each tested model. The numbering corresponds to those reported in the main text. The column density is given in units of 10^{22} cm^{-2}, while the ionization parameter is in units of erg s^{-1} cm. The $\Delta\chi^2$ is computed with respect to Model 0 ($\chi^2 = 194.9, \nu = 114$).

#	Γ	N_H	CF	logξ	R	E_{line}	$\Delta\chi^2$	$\Delta\nu$
0	$1.58^{+0.03}_{-0.03}$	–	–	–	–	–	–	–
1	$1.58^{+0.03}_{-0.03}$	$< 10^{-6}$	–	–	–	–	0	1
2	$2.00^{+0.09}_{-0.09}$	$11.04^{+2.46}_{-2.16}$	$0.57^{+0.07}_{-0.08}$	–	–	–	56	2
2.1	$1.97^{+0.10}_{-0.10}$	$10.30^{+2.48}_{-2.17}$	$0.54^{+0.07}_{-0.09}$	–	$6.84^{+0.11}_{-0.10}$	–	71.3	2
3	$1.95^{+0.12}_{-0.12}$	$8.30^{+5.02}_{-1.29}$	$0.54^{+0.08}_{-0.12}$	$0.19^{+1.00}_{-0.21}$	–	–	46.6	3
5	$1.59^{+0.03}_{-0.03}$	–	–	–	< 0.005	$6.83^{+0.08}_{-0.09}$	27	3
6	$2.01^{+0.19}_{-0.10}$	$9.87^{+1.33}_{-2.27}$	$0.55^{+0.09}_{-0.09}$	–	$0.03^{+0.13}_{-0.03}$	$6.84^{+0.10}_{-0.10}$	27	3

4.4.2 Reflection models: `pexrav`

After assessing the significance of an extra absorption, I tested whether a reflection component was required by the data. The only possible emission line is placed at energies that are not consistent with the typical neutral FeKα emission, therefore I assessed the significance of such component by the simultaneous addition of reflection and narrow emission line through separate components to Model 0 (Model 5: `phabs*(zpowerlw+pexrav+zgauss)`). As for the 2002 data, considering the reflection component without an absorption did not yield good results: $\Delta\chi^2 = 27$ for the addition of three parameters (best-fit values: $R \leq 0.005$, $\Gamma = 1.59 \pm 0.03$, $E = 6.83^{+0.09}_{-0.08}$) and the residuals, except for those corresponding to the emission line, are almost unchanged with respect to those in Figure 4.14. Furthermore, the best-fit reflection fraction is consistent with zero, indicating that this component is not required. However, even adding the reflection and emission line to Model 2 (Model 6: `phabs*zpcf*(zpowerlw+pexrav+zgauss)`) did not yield great results: $\Delta\chi^2 = 15.5$ for the addition of two parameters with respect to Model 2. Also in this case the residuals are almost unchanged from what is shown in Figure 4.16, middle panel, except for those determined by the emission line. Moreover, the best-fit reflection fraction is again consistent with zero within its 90% errors ($R \leq 0.16$). By comparing the significance of Model 5 to that of Model 2.1, it is clear that the statistical improvement is almost totally due to the addition of the emission line, thus it can be stated that the 2018 data do not require a reflection continuum component.

4.5 Summary of the XMM-Newton results

The 2002 spectrum is consistent with a power-law emission model absorbed both by the Milky Way and by a rather thick ($N_H \simeq 2 \times 10^{23}$cm^{-2}), highly

ionized ($\log(\xi/\mathrm{erg\ s^{-1}cm}) \simeq 3$) material, outflowing at $v_{out} \sim 0.1c$. The prominent absorption iron resonant line measured at $E \simeq 7.4$ keV, given the outflowing velocity and the ionization state of the material, is consistent with being dominated by Fe XXV (at the rest-frame energy of 6.70 keV). The same data are almost equally well represented by a power-law emission absorbed both by the Galaxy and a rather thin total covering neutral gas, plus a narrow Guassian component as absorption line. However, the first representation is thought to be preferable given the natural explanation that it provides for the absorption line at ~ 7.4 keV thanks to its ionization and outflowing velocity.

The 2018 data do not show any blueshifted absorption feature that could be attributed to an outflowing gas; some absorption complexities, however, are found in the soft band. These are best reproduced by a partial covering cold material ($N_H \simeq 1.1 \times 10^{23}$ cm^{-2}, $CF \simeq 0.57$), with a 90% upper limit to its ionization state of $\log(\xi/\mathrm{erg\ s^{-1}cm}) \leq 2.1$. The data show a narrow emission line at $E = 6.84^{+0.11}_{-0.10}$ keV, with an equivalent width of $EW = 267^{+110}_{-111}$ eV. However, this line is in tension with being produced by the absorber since, given its ionization parameter upper limit, it is consistent with iron at a ionization state between Fe I – XX (Makishima, 1986).

Constraining the reflection component is challenging both for the 2002 and 2018 spectra, also due to the limited energy range provided at high energies. For what concerns the 2002 data, a reflection component is statistically significant only when a very steep power-law ($\Gamma \simeq 2.65$) is assumed, while it is negligible when a typical AGN slope ($\Gamma \simeq 1.9$) is adopted. In any case, the data show some excess below 6 keV that could be interpreted as a micro-lensed FeKα, which is, however, only marginally detected. Regarding the 2018 data, a prominent emission line is placed at energies consistent with being a FeKα ($E = 6.84^{+0.11}_{-0.10}$ keV) but, in either case, the reflection component was found not to be required by the data; therefore, the interpretation of the $\simeq 6.84$ keV line as produced by the reflection over the accretion disk cannot be supported.

Chapter 5

Discussion of Chandra and XMM-Newton results, and future perspectives

The characterization of AGN feedback and a full comprehension of the physics behind it are still open issues. The AGN feedback is thought to be linked with the powerful winds that are likely to rise from the innermost regions of the AGN, the so-called UFOs. Winds have been detected at different wavelengths, indicating the presence of various gas phases, each outflowing at different velocities and showing different spatial distributions and sizes. Moreover, the kinetic power of molecular winds and UFOs were found to correlate for the few sources that show both components (for instance, IRASF11119+13257 Tombesi et al., 2015). This led to the idea that UFOs could be energetic enough to expand and be able to actually sweep out the gas of the host galaxy, thus directly acting on its evolution.
UFOs have been observed in a large number ($\sim 40-50\%$) of bright, low-redshift (<0.1) Seyfert galaxies for which good XMM-*Newton* and/or Suzaku spectra are available. At high redshift, the number of detections is still limited but UFOs were seen both in radio-quiet quasars and radio-loud objects ($z \simeq 1.5-4$). The cosmic time at which the interaction between the AGN and its host galaxy is expected to be most relevant is $z \simeq 2$, when both the cosmic star formation density and the AGN/QSO activity peaked. Almost all the sources showing UFO signatures at $z \gtrsim 0.1$ are gravitationally lensed. Indeed, given the induced flux magnification, gravitational lensing offers a unique tool to investigate such winds in distant AGN. In this regard, I analyzed in a uniform and comprehensive way all the available *Chandra* and XMM-*Newton* observations of the X-ray bright and lensed quasar Q2237+030 at $z = 1.695$. This object is part of a larger sample (of approximately ten sources), composed of other gravitationally lensed distant quasars ($z \geq 1.5$) and non-lensed high-flux QSOs at high redshift, which will allow

to statistically study the occurrence of these X-ray winds at high redshift.

All the available X-ray data as of October 2018 were analyzed: 35 *Chandra* archival observations and two[1] XMM-*Newton* datasets, one public (2002) and one proprietary data (2018, PI: M. Dadina), spanning in total over 18 years ($\sim$ 6.7yr in the QSO rest frame). On the one hand, the *Chandra* data, given their superb angular resolution, allow a spatially resolved spectral analysis over the single images of the quasar. On the other hand, XMM-*Newton* cannot resolve the images but, given its larger effective area, grants better quality spectra. These datasets are fundamental to investigate the physical origin of the source emission through more complex and physical models. However, for a comprehensive analysis of the X-ray properties of the source, both *Chandra* and XMM-*Newton* data are necessary, given the rather complementary strengths of these X-ray facilities.

The *Chandra* data allowed me to probe the source spectral variability in terms of photon-index evolution through the various epochs (see Figure 3.7). The spectral shape shows significant variations (at $> 99.9\%$ confidence) through time. These variations are consistent among the four images, in agreement to what found by Chen et al. (2012). This can be interpreted either as due to intrinsic source variability or to the presence of a variable absorption component. Limiting the analysis to the high-statistics sample (fourteen spectra having more than 500 cts, see Table 3.2), the addition of an absorber is highly required in four datasets out of the fourteen (ObsIDs 11534 image A and D, 11538 image A, 18804 image A). Comparing the 90% confidence contours of the two observations showing the highest variation in column density (ObsIDs 11534 A and 11538 A, Figure 3.13), it turned out that these are not consistent within 1.6σ. Given the time elapsed between the two epochs ($\simeq$ 0.3yrs in the QSO rest frame), this result allows us to state that, at more than 90% confidence, the absorber is located at the quasar redshift, instead of the lensing galaxy. This statement is also supported by the fact that such absorption component is detected in the same image for both observations. Moreover, the best-fit column densities of these four spectra show a significant variability ($> 99\%$ confidence level) when assuming the photon index obtained averaging those of the high-statistics sample ($< \Gamma >= 1.93$) for all the four spectra. Thus, it seems likely that the photon index variability could be ascribed to a variable absorber, but we cannot exclude that part of such variability could be produced by an intrinsic variation of the source emission.

The need of an extra absorber (and, eventually, an investigation of its nature) was pursued using XMM-*Newton* data, since the lower statistics of the *Chandra* spectra remain difficult to constrain more complex physical models. The 2002 data are well reproduced by a rather thick ($N_H = (2.1^{+0.5}_{-0.6}) \times 10^{23}$ cm^{-2}), highly ionized ($\log(\xi/\mathrm{erg\ s^{-1}cm}) = 3.0 \pm 0.1$)

[1]The 2016 observations was left out because highly affected by soft-p$^+$ flares.

medium, outflowing at $v_{out} = (0.1 \pm 0.01)c$, whose properties are consistent with the prominent absorption line at $E = 7.4 \pm 0.1$ keV. On a statistical basis, the 2002 spectrum is similarly well reproduced by a phenomenologial model composed of a cold absorber plus a narrow absorption feature. However, the first scenario allows a natural and self-consistent explanation for the absorption line, while the second does not. For this reason, we consider that the best modeling for the 2002 data includes such thick, highly ionized, outflowing absorber. This component, however, fails to explain the hints of an additional narrow absorption at ~ 11.8 keV which, if we assume it to be blueshifted Fe XXVI, would require an outflowing velocity of $\approx 0.5c$. This could be the hint of a multi-velocity outflow, where the most prominent during the 2002 observation was the component outflowing at 0.1c. The measured, rest-frame $2 - 10$ keV luminosity corrected for the absorption for the 2002 observation is $L_{2-10} \simeq 6.8 \times 10^{44}$ erg s^{-1}. Given the magnification factor $\mu \approx 16$ estimated by Schmidt et al. (1998), the intrinsic absorption-corrected luminosity is $L_{2-10} \simeq 4.3 \times 10^{43}$ erg s^{-1}. Assuming the bolometric correction factor ($k_{bol} \approx 20$) by Lusso et al. (2012), it implies a bolometric luminosity of $L_{bol} \simeq 8.6 \times 10^{44}$ erg s^{-1}.

Following Tombesi et al. (2012), one can estimate the location of the outflowing gas as upper and lower limits of its distance from the central BH. The minimum distance (r_{min}) can be inferred assuming that the absorber is located at the distance from the BH corresponding to its escape velocity:

$$r_{min} = \frac{2GM_{BH}}{v_{out}^2} \tag{5.1}$$

while the maximum distance (r_{max}) can be computed from the definition of the ionization parameter $\xi = L_X/nr^2 = L_X/N_H r$, i.e.

$$r_{max} = \frac{L_X}{N_H \xi}. \tag{5.2}$$

Given the best-fit values, we find $r_{min} = 0.010^{+0.020}_{-0.007}$ pc and $r_{max} = 0.07^{+0.03}_{-0.02}$ pc for the position of the outflowing wind detected in the 2002 data; these values are consistent with the typical size of the BLR in this source ($\gtrsim 0.1$pc, Metcalf et al., 2004). A rough estimate of the mass outflow rate $\dot{M}_{out}$ can be obtained from the following formula (Crenshaw et al., 2003)

$$\dot{M}_{out} = 4\pi m_p \mu N_H v_{out} r C \tag{5.3}$$

where m_p is the proton mass, μ is the mean atomic mass per proton (1.4 for solar abundances), r is the distance from the BH and C is the global covering factor of the wind (typical value ≈ 0.5; Tombesi et al., 2012). To be conservative, we consider the lower limit of the distance from the BH ($r_{min} \simeq 0.01$pc) in order to compute the lower limit of the mass-outflow rate: $\dot{M}_{out} = (3.96^{+1.08}_{-0.44}) M_\odot$ yr^{-1}. This value implies a mechanical output

($\dot{E}_{kin} = \frac{1}{2}\dot{M}_{out}v_{out}^2$, Tombesi et al., 2012) of $\dot{E}_{kin} = (1.2^{+0.4}_{-0.4}) \times 10^{45}$ erg s^{-1}, which corresponds to an outflow efficiency of ≈ 1.4 L_{bol}. The outflow momentum rate ($\dot{p}_{out} = \dot{M}_{out}v_{out}$, Tombesi et al., 2012) is $\dot{p}_{out} = (7.9 \pm 2.7) \times 10^{35}$ g cm s^{-2} and the radiation force ($\dot{p}_{rad} = L_{bol}/c$) is $\dot{p}_{rad} \simeq 2.9 \times 10^{34}$ g cm s^{-2}, thus their ratio is $\dot{p}_{out}/\dot{p}_{rad} \approx 28$. Given the approximations that are intrinsic to the modeling of these kind of winds and those produced by the data analysis itself, the uncertainties of $\dot{E}_{kin}$ and $\dot{p}_{out}$ are given as a third of their mean value. This is an indicative percentage of the real uncertainty, since the error on the mass outflow rate, obtained propagating the uncertainties of the quantities in eq. 5.3, is ≈25% of its value. The $\dot{E}_{kin}/L_{bol}$ and $\dot{p}_{out}/\dot{p}_{rad}$ ratios are much higher than those seen in local AGN and well above the limit predicted for efficient wind-driven AGN feedback ($> 0.05 - 0.5\%$, Di Matteo et al., 2005; Hopkins and Elvis, 2010). However, this is not the first distant AGN showing a fast outflow with this kind of properties. For instance, the radio-quiet quasar HS 0810+2554 ($z = 1.51$) shows a $\dot{E}_{kin}/L_{bol} \approx 9$ (Chartas et al., 2016) and also the radio-loud lensed quasar MG J0414+0534 ($z = 2.64$) has $\dot{E}_{kin}/L_{bol} \approx 2.5$ and $\dot{p}_{out}/\dot{p}_{rad} \approx 17$. The difference resides in the outflowing velocity, since the one we detect in the Einstein Cross is much lower than that of the other two systems, being $\approx 0.43 - 0.76$c for HS 0810 and ≈ 0.3c for MG J0414. In any case, it would seem that such outflow might actually be able to significantly affect the evolution of the host galaxy and the large ratios suggest that the wind might significantly accelerated by magnetic forces along with radiation itself. The rough estimates for the location and the best-fit parameters of the wind are consistent with the typical properties of UFOs detected in local ($z \leq 0.1$) radio-quiet AGN, while the mass outflow rate is higher than the mean values found for the local sources (Tombesi et al., 2012).

For what concerns winds at different wavelengths (i.e. gas phases), Fiore et al. (2017) analyzed the properties of massive outflows found in 94 AGN, from sub-pc to kpc scales, in order to assess the scaling relations between host galaxy and AGN properties and those of the AGN winds. The aim of their work was to represent the state-of-the-art of our observational understanding of quasar-mode AGN feedback. However, the sample of Fiore et al. (2017) does not allow to estimate the outflow occurrence because, being a compilation of objects in which winds were detected, it is biased and not complete. Figure 5.1 displays the $\dot{M}_{out} - L_{bol}$ and $\dot{E}_{kin} - L_{bol}$ plots by Fiore et al. (2017) where I added the Einstein Cross (orange hexagon) to show how its absorber relates with the winds detected in other sources. As one can see, its mass outflow rate (Figure 5.1, left panel) is much higher than that of local X-ray winds and seems to be more in agreement with the ionized winds showing the least mass outflow rates. If we consider the values found for HS 0810+2554 ($\dot{M}_{out} = 1.5 - 3.4$ $M_\odot$ yr^{-1}, $L_{bol} \simeq 1.4 \times 10^{45}$ erg s^{-1}, Chartas et al., 2016) and MG J0414+0534 ($\dot{M}_{out} \approx$ $M_\odot$ yr^{-1}, $L_{bol} \simeq 1 \times 10^{46}$ erg s^{-1}, Dadina et al., 2018), both of these sources seem to be more consistent with

the scaling relation found by Fiore et al. (2017) for the ionized winds, rather than that for local X-ray winds, just as found for the Einstein Cross. Figure 5.1 graphically shows that the kinetic power of this wind is larger than the bolometric luminosity of the system and is similar to the $\dot{E}_{kin}$ of the bright quasar PG 1211+143 (Pounds and Reeves, 2007, 2009).

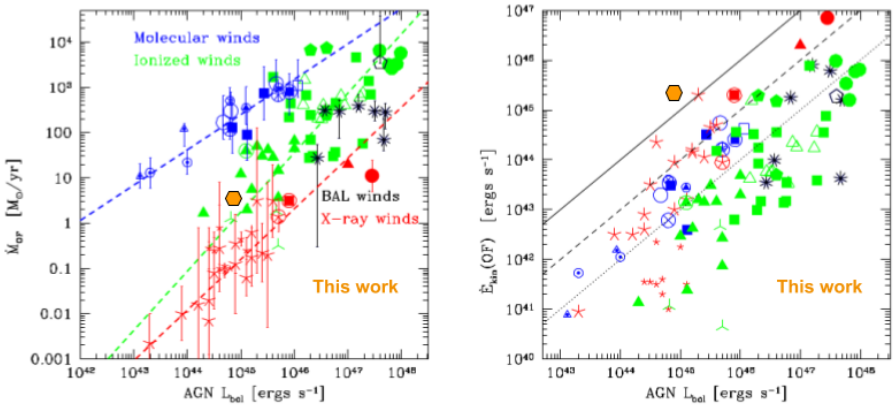

Figure 5.1: $\dot{M}_{out} - L_{bol}$ (*left panel*) and $\dot{E}_{kin} - L_{bol}$ (*right panel*) plots by Fiore et al. (2017) for molecular winds (blue markers), ionized winds (green markers), BAL winds (black markers) and X-ray winds (red markers). The dashed lines in the left panel represent the best fit correlations of molecular, ionized and X-ray winds, color-coded as the respective markers. The dotted, dashed, solid lines in the right panel represent the correlations $\dot{E}_{kin} = 0.01, 0.1, 1\ L_{bol}$. The orange hexagon indicates the properties of the outflow detected in the 2002 XMM-*Newton* data, as described in the main text.

Interestingly, the 2018 data, instead, do not show any prominent absorption line in the hard band and seem to be best reproduced by a partially covering cold absorber ($N_H = (1.1 \pm 0.2) \times 10^{23}$ cm^{-2}, $CF = 57\% \pm 8\%$, $z_{abs} = z_Q$), with ionization parameter of $\log(\xi/\text{erg s}^{-1}\text{cm}) < 2.1$ (90% confidence limit). The intrinsic, absorption-corrected $2 - 10$ keV luminosity for the 2018 data is $L_{2-10} \simeq 2.0 \times 10^{44}$ erg s^{-1}, that corresponds to approximately 47% of that found for the 2002 data. From the upper limit of the ionization state, we evaluated the lower limit of the maximum distance from the central BH of this absorption component (using eq. (5.2)): $r \geq 4.96$pc. Such absorber is therefore in agreement with being placed at a distance consistent with being external to the previous location (BLR) and more typical of the molecular torus (e.g. Jaffe et al., 2004; Burtscher et al., 2013).

The time elapsed between the two XMM-*Newton* observations is $\simeq 5.94$yr in the quasar rest frame. To test the possibility that the two absorption components are one the evolution of the other, we evaluated the minimum time the gas would have taken to move from ≈ 0.66pc to ≈ 4.96pc, making the (strong) assumption of its velocity always being equal to 0.1c. The yielded travel-time is ≈ 148 yr, therefore the two gas phases cannot be one the evolution of the other. Given that the winds generated by the accretion disk

are thought to have a global covering fraction less than unity, the scenario we propose is that between the 2002 and the 2018 observations the wind has changed its direction with respect to the line of sight and the disk, and part of the clouds contained in or within the molecular torus intercepted the line of sight during the second pointing. Given the short timescale, we think it is unlikely that the outflow has been totally suppressed between the two observations. Moreover, from the lowest timescale of the absorber variability obtained from the *Chandra* data ($\simeq$ 0.3yrs rest frame between ObsIDs 11534 and 11538), one can infer the spatial scale at which such medium could be placed: $d \approx c\Delta t \approx 0.09$pc. Therefore, the absorber detected in four of the *Chandra* high-statistics sample could be placed at the innermost part of the torus and the outermost of the BLR. Given that these observations were taken in between the XMM-*Newton* ones, this result is thought to be consistent with the proposed patchy torus scenario, even though the lower statistics of the *Chandra* spectra did not allow us to investigate the presence of more complex absorbers than a neutral medium.

Regarding the spectral features, we detected significant narrow absorption lines in the X-ray spectra of the Einstein Cross for the first time. The most prominent absorption feature is that of the 2002 data which, given the best-fit parameters of the outflowing medium, is consistent with a blueshifted FeKα line dominated by Fe XXV ($\log[\xi/\mathrm{erg\ s^{-1}cm}] \simeq 3$, Makishima, 1986). Absorption lines in the range of blueshifted resonant iron features were also detected at more than 90% confidence in eight spectra of the *Chandra* high-statistics sample, suggesting the persistence of such absorber in the X-ray spectra of this quasar (see Figure 3.17(b)). However, they seem to "prefer" higher energies with respect to the $\simeq$ 7.4 keV line detected in the 2002 spectrum and seem to be more consistent with the hints of a narrow absorption line observed at $\sim$ 11.8 keV in the 2002 data. Assuming the absorption lines detected at energies higher than $\sim$ 9 keV to be produced by an outflowing absorber with an ionization state similar to that detected in 2002 data yields, for these lines, a much higher outflowing velocity ($v_{out} \simeq 0.3 - 0.5$ c, when assumed to be dominated by Fe XXVI). Further analysis is required to assess the presence of a multi-velocity outflow component. The 2018 XMM-*Newton* data, instead, do not show any relevant absorption feature in the hard energy band. This is in agreement with the non detection of an outflowing absorber. A rough estimate of the wind duty cycle can be obtained by the occurrence of the iron resonant absorption lines. We detected a fast wind in nine spectra (one XMM-*Newton*, eight *Chandra*) out of sixteen, five of them at the 99% and four at the 90% confidence level. These detections yield a wind duty cycle of approximately 50%.

The 2018 spectrum shows a prominent narrow emission line, whose energy was constrained to be at E $\simeq$ 6.8 keV. This is consistent with the one detected by Reynolds et al. (2014), who analyzed the spatially-integrated summed spectrum of 26 *Chandra* observations (ObsIDs from 431 to 14514).

We first interpreted this line as possibly associated with a reflection component. This component turned out not to be required by the data, ruling out also the scenario of a micro-lensed FeKα. Another possibility is that the line is produced by the absorber itself. However, given the energy of the line, it is inconsistent with the ionization state of the medium. Following Makishima (1986), the upper limit to the ionization parameter of the absorber ($\log[\xi/\mathrm{erg\ s^{-1}cm}] < 2.1$) implies Fe I–XX, while the energy of the line is consistent with being dominated by Fe XXV–XXVI. Given these premises, one last possible scenario can be the presence of an additional highly ionized component ($\log(\xi/\mathrm{erg\ s^{-1}cm}) \geq 3$) that was not accounted for in our analysis, since we limited the investigation to just one gas phase.
Moreover, eight spectra out of the *Chandra* high-statistics sample show emission lines in the $2.0 - 6.5$ keV rest-frame energy range which are only marginally (90% confidence) detected. However, to be noticed is that such lines seem to "cluster" in two groups (see Figure 3.17(a)), one around ~ 4 keV and the other around ~ 5.8 keV, where the latter shows energies around that of the micro-lensed FeKα emission line detected by Dai et al. (2003). One possible explanation of such "clustering" could be that of those lines are micro-lensed FeKα lines, whose energy has varied among the epochs due to the caustic crossing different regions of the accretion disk, as a result of the motion of the stars in the lensing galaxy (Chartas et al., 2002). However, to test this scenario, a more accurate analysis of the micro-lensing effects of the system would be required.

5.1 Summary and future perspectives

From the analysis of all the available X-ray data as of October 2018, we detected, for the first time, absorption features in the X-ray spectra of the Einstein Cross. Given the photon index variations derived from the *Chandra* single-image spectra and the detection of absorption only in four out of the fourteen *Chandra* high-statistics spectra, the presence of a variable absorber seems to be the most reasonable explanation. Furthermore, this finding would be in agreement with the variation inferred from the XMM-*Newton* data, where we detected a highly-ionized, fast outflowing absorber in the 2002 spectrum but then only a cold, partially covering medium in the 2018 data. The proposed scenario is that the fast winds generated by the accretion disk intercepted the line of sight during the 2002 observation, while the clouds of the molecular torus did not. Then, being those winds only partially covering the disk, they could well have exited the line of sight and let the molecular torus inner clouds intercept it during the 2018 pointing.

To test the proposed scenario, an interesting future analysis could be to investigate the presence of a neutral or ionized absorption component in all the *Chandra* spectra, even though complex models are hard to constrain

given the statistics that these datasets provide. Moreover, two additional long observations (PI: G. Chartas) were made public after October 2018 and other three additional observations (PI: G. Chartas) will be made public by the beginning of 2020; four of the five new datasets have exposures longer than ~ 20 ks.

A deeper and more accurate analysis of the micro-lensing effects is surely required to test the possibility of a micro-lensed FeKα, whose energy varies among the epochs. This could be explained by the intricate motion of the stars in the lensing galaxy that induce caustic crossing events, magnifying only part of the emission and/or reflecting region responsible for the FeKα emission.

Another future development surely resides in the increase of the distant source sample to better assess the properties of X-ray winds in high-redshift AGN. This could be achieved through either XMM-*Newton* and *Chandra* programs aimed at obtaining long exposures of distant, less luminous gravitationally lensed sources, as long as these two X-ray facilities continue to acquire high-quality data. To this goal, the advent of *Athena* (Advanced Telescope for High Energy Astrophysics), scheduled for 2031, will provide a breakthrough in the characterization of X-ray winds, thanks to its unparalleled sensitivity ($A_{\rm eff} \sim 1.4$ m^2 at 1 keV, $A_{\rm eff} \sim 0.25$ m^2 at 6 keV) and the unprecedented energy resolution of its X-ray Integral Field Unit (X-IFU, < 2.5 eV between 0.1 and 7 keV). The sample of quasars could then be expanded to much fainter and/or more distant objects, significantly improving the statistical basis when probing the presence and properties of such fast X-ray winds. To this regard, the All Sky Survey that will be performed by *eROSITA* in the next years will allow to search for new candidates. However, specific follow-ups would them be required using XMM-*Newton*, *Chandra* or *eROSITA* itself in order to obtain spectra with good enough signal-to-noise to properly constrain the models.

Bibliography

Antonucci, R. (1993), 'Unified models for active galactic nuclei and quasars.', *Annual Review of Astronomy and Astrophysics* **31**, 473–521.

Antonucci, R. R. J. and Miller, J. S. (1985), 'Spectropolarimetry and the nature of NGC 1068.', *ApJ* **297**, 621–632.

Arnaud, K. A. (1996), XSPEC: The First Ten Years, *in* G. H. Jacoby and J. Barnes, eds, 'Astronomical Data Analysis Software and Systems V', Vol. 101 of *Astronomical Society of the Pacific Conference Series*, p. 17.

Assef, R. J., Denney, K. D., Kochanek, C. S., Peterson, B. M., Kozłowski, S., Ageorges, N., Barrows, R. S., Buschkamp, P., Dietrich, M., Falco, E., Feiz, C., Gemperlein, H., Germeroth, A., Grier, C. J., Hofmann, R., Juette, M., Khan, R., Kilic, M., Knierim, V., Laun, W., Lederer, R., Lehmitz, M., Lenzen, R., Mall, U., Madsen, K. K., Mandel, H., Martini, P., Mathur, S., Mogren, K., Mueller, P., Naranjo, V., Pasquali, A., Polsterer, K., Pogge, R. W., Quirrenbach, A., Seifert, W., Stern, D., Shappee, B., Storz, C., Van Saders, J., Weiser, P. and Zhang, D. (2011), 'Black Hole Mass Estimates Based on C IV are Consistent with Those Based on the Balmer Lines', *ApJ* **742**, 93.

Avni, Y. (1976), 'Energy spectra of X-ray clusters of galaxies.', *ApJ* **210**, 642–646.

Bassani, L., Dadina, M., Maiolino, R., Salvati, M., Risaliti, G., Della Ceca, R., Matt, G. and Zamorani, G. (1999), 'A Three-dimensional Diagnostic Diagram for Seyfert 2 Galaxies: Probing X-Ray Absorption and Compton Thickness', *The Astrophysical Journal Supplement Series* **121**, 473–482.

Blustin, A. J., Page, M. J., Fuerst, S. V., Branduardi- Raymont, G. and Ashton, C. E. (2005), 'The nature and origin of Seyfert warm absorbers', *A & A* **431**, 111–125.

Burtscher, L., Meisenheimer, K., Tristram, K. R. W., Jaffe, W., Hönig, S. F., Davies, R. I., Kishimoto, M., Pott, J. U., Röttgering, H., Schartmann, M., Weigelt, G. and Wolf, S. (2013), 'A diversity of dusty AGN tori. Data

release for the VLTI/MIDI AGN Large Program and first results for 23 galaxies', *A & A* **558**, A149.

Cappi, M., Panessa, F., Bassani, L., Dadina, M., Di Cocco, G., Comastri, A., della Ceca, R., Filippenko, A. V., Gianotti, F., Ho, L. C., Malaguti, G., Mulchaey, J. S., Palumbo, G. G. C., Piconcelli, E., Sargent, W. L. W., Stephen, J., Trifoglio, M. and Weaver, K. A. (2006), 'X-ray spectral survey with XMM-Newton of a complete sample of nearby Seyfert galaxies', *A & A* **446**, 459–470.

Chartas, G., Agol, E., Eracleous, M., Garmire, G., Bautz, M. W. and Morgan, N. D. (2002), 'Caught in the Act: Chandra Observations of Microlensing of the Radio-loud Quasar MG J0414+0534', *ApJ* **568**, 509–521.

Chartas, G., Brandt, W. N. and Gallagher, S. C. (2003), 'XMM-Newton Reveals the Quasar Outflow in PG 1115+080', *ApJ* **595**, 85–93.

Chartas, G., Brandt, W. N., Gallagher, S. C. and Proga, D. (2007), 'XMM-Newton and Chandra Spectroscopy of the Variable High-Energy Absorption of PG 1115+080: Refined Outflow Constraints', *ApJ* **133**, 1849–1860.

Chartas, G., Cappi, M., Hamann, F., Eracleous, M., Strickland, S., Giustini, M. and Misawa, T. (2016), 'The Wide-angle Outflow of the Lensed z = 1.51 AGN HS 0810+2554', *ApJ* **824**, 53.

Chartas, G., Eracleous, M., Dai, X., Agol, E. and Gallagher, S. (2007), 'Discovery of Probable Relativistic Fe Emission and Absorption in the Cloverleaf Quasar H 1413+117', *ApJ* **661**, 678–692.

Chartas, G., Saez, C., Brandt, W. N., Giustini, M. and Garmire, G. P. (2009), 'Confirmation of and Variable Energy Injection by a Near-Relativistic Outflow in APM 08279+5255', *ApJ* **706**, 644–656.

Chen, B., Dai, X., Kochanek, C. S., Chartas, G., Blackburne, J. A. and KozŎ142owski, S. (2011), 'Discovery of energy-dependent x-ray microlensing in q2237+0305', *The Astrophysical Journal Letters* **740**(2), L34.
URL: *http://stacks.iop.org/2041-8205/740/i=2/a=L34*

Chen, B., Dai, X., Kochanek, C. S., Chartas, G., Blackburne, J. A. and Morgan, C. W. (2012), 'X-Ray Monitoring of Gravitational Lenses with Chandra', *ApJ* **755**, 24.

Corrigan, R. T., Irwin, M. J., Arnaud, J., Fahlman, G. G., Fletcher, J. M., Hewett, P. C., Hewitt, J. N., Le Fevre, O., McClure, R., Pritchet, C. J., Schneider, D. P., Turner, E. L., Webster, R. L. and Yee, H. K. C. (1991), 'Initial light curve of Q2237 + 0305', *ApJ* **102**, 34–40.

Crenshaw, D. M., Kraemer, S. B. and George, I. M. (2003), 'Mass Loss from the Nuclei of Active Galaxies', *Annual Review of Astronomy and Astrophysics* **41**, 117–167.

Dadina, M. (2008), 'Seyfert galaxies in the local Universe (z $\leq$ 0.1): the average X-ray spectrum as seen by BeppoSAX', *A & A* **485**, 417–424.

Dadina, M., Vignali, C., Cappi, M., Lanzuisi, G., Ponti, G., Torresi, E., De Marco, B., Chartas, G. and Giustini, M. (2018), 'Yet another UFO in the X-ray spectrum of a high-z lensed QSO', *A & A* **610**, L13.

Dai, X., Chartas, G., Agol, E., Bautz, M. W. and Garmire, G. P. (2003), 'Chandra Observations of QSO 2237+0305', *ApJ* **589**, 100–110.

Di Matteo, T., Springel, V. and Hernquist, L. (2005), 'Energy input from quasars regulates the growth and activity of black holes and their host galaxies', *Nature* **433**, 604–607.

Done, C., Gierliński, M., Sobolewska, M. and Schurch, N. (2007), The Origin of the Soft Excess in AGN, *in* L. C. Ho and J. W. Wang, eds, 'The Central Engine of Active Galactic Nuclei', Vol. 373 of *Astronomical Society of the Pacific Conference Series*, p. 121.

Fabian, A. C. (2012), 'Observational Evidence of Active Galactic Nuclei Feedback', *Annual Review of Astronomy and Astrophysics* **50**, 455–489.

Fabian, A. C., Lohfink, A., Kara, E., Parker, M. L., Vasudevan, R. and Reynolds, C. S. (2015), 'Properties of AGN coronae in the NuSTAR era', *MNRAS* **451**, 4375–4383.

Fedorova, E. V., Zhdanov, V. I., Vignali, C. and Palumbo, G. G. C. (2008), 'Q2237+0305 in X-rays: spectra and variability with XMM-Newton', *A & A* **490**, 989–994.

Feruglio, C., Fiore, F., Carniani, S., Piconcelli, E., Zappacosta, L., Bongiorno, A., Cicone, C., Maiolino, R., Marconi, A., Menci, N., Puccetti, S. and Veilleux, S. (2015), 'The multi-phase winds of Markarian 231: from the hot, nuclear, ultra-fast wind to the galaxy-scale, molecular outflow', *A & A* **583**, A99.

Feruglio, C., Piconcelli, E., Bischetti, M., Zappacosta, L. and Fiore, F. (2017), AGN feedback through UFO and galaxy-wide winds in the early Universe, *in* 'The X-ray Universe 2017', p. 78.

Fiore, F., Feruglio, C., Shankar, F., Bischetti, M., Bongiorno, A., Brusa, M., Carniani, S., Cicone, C., Duras, F., Lamastra, A., Mainieri, V., Marconi, A., Menci, N., Maiolino, R., Piconcelli, E., Vietri, G. and Zappacosta, L. (2017), 'AGN wind scaling relations and the co-evolution of black holes and galaxies', *A & A* **601**, A143.

Gallagher, S. C. and Everett, J. E. (2007), Stratified Quasar Winds: Integrating X-ray and Infrared Views of Broad Absorption-line Quasars, *in* L. C. Ho and J. W. Wang, eds, 'The Central Engine of Active Galactic Nuclei', Vol. 373 of *Astronomical Society of the Pacific Conference Series*, p. 305.

Ghisellini, G., Haardt, F. and Matt, G. (1994), 'The contribution of the obscuring torus to the X-ray spectrum of Seyfert galaxies: a test for the unification model.', *MNRAS* **267**, 743–754.

Guerras, E., Dai, X., Steele, S., Liu, A., Kochanek, C. S., Chartas, G., Morgan, C. W. and Chen, B. (2017), 'Extended X-Ray Monitoring of Gravitational Lenses with Chandra and Joint Constraints on X-Ray Emission Regions', *ApJ* **836**, 206.

Haardt, F. and Maraschi, L. (1991), 'A Two-Phase Model for the X-Ray Emission from Seyfert Galaxies', *ApJ* **380**, L51.

Haardt, F. and Maraschi, L. (1993), 'X-Ray Spectra from Two-Phase Accretion Disks', *ApJ* **413**, 507.

Haardt, F., Maraschi, L. and Ghisellini, G. (1997), 'X-Ray Variability and Correlations in the Two-Phase Disk-Corona Model for Seyfert Galaxies', *ApJ* **476**, 620–631.

Hasinger, G., Schartel, N. and Komossa, S. (2002), 'Discovery of an Ionized Fe K Edge in the z=3.91 Broad Absorption Line Quasar APM 08279+5255 with XMM-Newton', *ApJL* **573**, L77–L80.

Hopkins, P. F. and Elvis, M. (2010), 'Quasar feedback: more bang for your buck', *MNRAS* **401**, 7–14.

Hopkins, P. F., Hernquist, L., Cox, T. J., Di Matteo, T., Robertson, B. and Springel, V. (2006), 'A Unified, Merger-driven Model of the Origin of Starbursts, Quasars, the Cosmic X-Ray Background, Supermassive Black Holes, and Galaxy Spheroids', *The Astrophysical Journal Supplement Series* **163**, 1–49.

Huchra, J., Gorenstein, M., Kent, S., Shapiro, I., Smith, G., Horine, E. and Perley, R. (1985), '2237 + 0305: A new and unusual gravitational lens', *ApJ* **90**, 691–696.

Jaffe, W., Meisenheimer, K., Röttgering, H. J. A., Leinert, C., Richichi, A., Chesneau, O., Fraix-Burnet, D., Glazenborg-Kluttig, A., Granato, G. L., Graser, U., Heijligers, B., Köhler, R., Malbet, F., Miley, G. K., Paresce, F., Pel, J. W., Perrin, G., Przygodda, F., Schoeller, M., Sol, H., Waters, L. B. F. M., Weigelt, G., Woillez, J. and de Zeeuw, P. T. (2004), 'The

central dusty torus in the active nucleus of NGC 1068', *Nature* **429**, 47–49.

Kalberla, P. M. W., Burton, W. B., Hartmann, D., Arnal, E. M., Bajaja, E., Morras, R. and Pöppel, W. G. L. (2005), 'The Leiden/Argentine/Bonn (LAB) Survey of Galactic HI. Final data release of the combined LDS and IAR surveys with improved stray-radiation corrections', *A & A* **440**, 775–782.

Kallman, T. and Bautista, M. (2001), 'Photoionization and High-Density Gas', *The Astrophysical Journal Supplement Series* **133**, 221–253.

Kaspi, S., Brandt, W. N., George, I. M., Netzer, H., Crenshaw, D. M., Gabel, J. R., Hamann, F. W., Kaiser, M. E., Koratkar, A., Kraemer, S. B., Kriss, G. A., Mathur, S., Mushotzky, R. F., Nandra, K., Peterson, B. M., Shields, J. C., Turner, T. J. and Zheng, W. (2002), 'The Ionized Gas and Nuclear Environment in NGC 3783. I. Time-averaged 900 Kilosecond Chandra Grating Spectroscopy', *ApJ* **574**, 643–662.

Kellermann, K. I., Sramek, R., Schmidt, M., Shaffer, D. B. and Green, R. (1989), 'VLA Observations of Objects in the Palomar Bright Quasar Survey', *ApJ* **98**, 1195.

King, A. and Pounds, K. (2015), 'Powerful Outflows and Feedback from Active Galactic Nuclei', *Annual Review of Astronomy and Astrophysics* **53**, 115–154.

Kormendy, J. and Richstone, D. (1995), 'Inward Bound—The Search For Supermassive Black Holes In Galactic Nuclei', *Annual Review of Astronomy and Astrophysics* **33**, 581.

Lampton, M., Margon, B. and Bowyer, S. (1976), 'Parameter estimation in X-ray astronomy.', *ApJ* **208**, 177–190.

Lanzuisi, G., Giustini, M., Cappi, M., Dadina, M., Malaguti, G., Vignali, C. and Chartas, G. (2012), 'HS 1700+6416: the first high-redshift unlensed narrow absorption line-QSO showing variable high-velocity outflows', *A & A* **544**, A2.

Leahy, D. A. (2001), 'Ginga Observations of Hercules X-1: Spectrum Dependence on 35 Day Phase', *ApJ* **547**, 449–456.

Lusso, E., Comastri, A., Simmons, B. D., Mignoli, M., Zamorani, G., Vignali, C., Brusa, M., Shankar, F., Lutz, D., Trump, J. R., Maiolino, R., Gilli, R., Bolzonella, M., Puccetti, S., Salvato, M., Impey, C. D., Civano, F., Elvis, M., Mainieri, V., Silverman, J. D., Koekemoer, A. M., Bongiorno, A., Merloni, A., Berta, S., Le Floc'h, E., Magnelli, B., Pozzi, F. and

Riguccini, L. (2012), 'Bolometric luminosities and Eddington ratios of X-ray selected active galactic nuclei in the XMM-COSMOS survey', *MNRAS* **425**, 623–640.

Madau, P., Ferguson, H. C., Dickinson, M. E., Giavalisco, M., Steidel, C. C. and Fruchter, A. (1996), 'High-redshift galaxies in the Hubble Deep Field: colour selection and star formation history to z˜4', *MNRAS* **283**, 1388–1404.

Magorrian, J., Tremaine, S., Richstone, D., Bender, R., Bower, G., Dressler, A., Faber, S. M., Gebhardt, K., Green, R., Grillmair, C., Kormendy, J. and Lauer, T. (1998), 'The Demography of Massive Dark Objects in Galaxy Centers', *ApJ* **115**, 2285–2305.

Makishima, K. (1986), *Iron Lines from Galactic and Extragalactic X-ray Sources*, p. 249.

Metcalf, R. B., Moustakas, L. A., Bunker, A. J. and Parry, I. R. (2004), 'Spectroscopic Gravitational Lensing and Limits on the Dark Matter Substructure in Q2237+0305', *ApJ* **607**, 43–59.

Mosquera, A. M., Kochanek, C. S., Chen, B., Dai, X., Blackburne, J. A. and Chartas, G. (2013), 'The Structure of the X-Ray and Optical Emitting Regions of the Lensed Quasar Q 2237+0305', *ApJ* **769**, 53.

Nandra, K. and Pounds, K. A. (1994), 'GINGA observations of the X-ray spectra of Seyfert galaxies.', *MNRAS* **268**, 405–429.

Ostensen, R., Refsdal, S., Stabell, R., Teuber, J., Emanuelsen, P. I., Festin, L., Florentin-Nielsen, R., Gahm, G., Gullbring, E., Grundahl, F., Hjorth, J., Jablonski, M., Jaunsen, A. O., Kaas, A. A., Karttunen, H., Kotilainen, J., Laurikainen, E., Lindgren, H., Maehoenen, P., Nilsson, K., Olofsson, G., Olsen, O., Pettersen, B. R., Piirola, V., Sorensen, A. N., Takalo, L., Thomsen, B., Valtaoja, E., Vestergaard, M. and Av Vianborg, T. (1996), 'Monitoring of the Einstein Cross with the Nordic Optical Telescope.', *A & A* **309**, 59–64.

Padovani, P., Alexander, D. M., Assef, R. J., De Marco, B., Giommi, P., Hickox, R. C., Richards, G. T., Smolčić, V., Hatziminaoglou, E., Mainieri, V. and Salvato, M. (2017), 'Active galactic nuclei: what's in a name?', *Astronomy and Astrophysics Review* **25**, 2.

Perola, G. C., Matt, G., Cappi, M., Fiore, F., Guainazzi, M., Maraschi, L., Petrucci, P. O. and Piro, L. (2002), 'Compton reflection and iron fluorescence in BeppoSAX observations of Seyfert type 1 galaxies', *A & A* **389**, 802–811.

Peterson, B. M. (2004), Black hole masses from reverberation measurements, *in* T. Storchi-Bergmann, L. C. Ho and H. R. Schmitt, eds, 'The Interplay Among Black Holes, Stars and ISM in Galactic Nuclei', Vol. 222 of *IAU Symposium*, pp. 15–20.

Petrucci, P. O., Ursini, F., De Rosa, A., Bianchi, S., Cappi, M., Matt, G., Dadina, M. and Malzac, J. (2018), 'Testing warm Comptonization models for the origin of the soft X-ray excess in AGNs', *A & A* **611**, A59.

Piconcelli, E., Jimenez-Bailón, E., Guainazzi, M., Schartel, N., Rodríguez-Pascual, P. M. and Santos- Lleó, M. (2005), 'The XMM-Newton view of PG quasars. I. X-ray continuum and absorption', *A & A* **432**, 15–30.

Pounds, K. A. and Reeves, J. N. (2007), 'Is the X-ray spectrum of the narrow emission line QSO PG1211+143 defined by its energetic outflow?', *MNRAS* **374**, 823–831.

Pounds, K. A. and Reeves, J. N. (2009), 'Quantifying the fast outflow in the luminous Seyfert galaxy PG1211+143', *MNRAS* **397**, 249–257.

Protassov, R., van Dyk, D. A., Connors, A., Kashyap, V. L. and Siemiginowska, A. (2002), 'Statistics, Handle with Care: Detecting Multiple Model Components with the Likelihood Ratio Test', *ApJ* **571**, 545–559.

Rees, M. J. (1984), Comments on the physics of active galactic nuclei, *in* W. Brinkmann and J. Truemper, eds, 'X-ray and UV Emission from Active Galactic Nuclei', pp. 138–151.

Reeves, J., Done, C., Pounds, K., Terashima, Y., Hayashida, K., Anabuki, N., Uchino, M. and Turner, M. (2008), 'On why the iron K-shell absorption in AGN is not a signature of the local warm/hot intergalactic medium', *MNRAS* **385**, L108–L112.

Reynolds, C. S. and Fabian, A. C. (1995), 'Warm absorbers in active galactic nuclei', *MNRAS* **273**, 1167–1176.

Reynolds, M. T., Walton, D. J., Miller, J. M. and Reis, R. C. (2014), 'A Rapidly Spinning Black Hole Powers the Einstein Cross', *ApJL* **792**, L19.

Risaliti, G. and Elvis, M. (2004), A Panchromatic View of AGN, *in* A. J. Barger, ed., 'Supermassive Black Holes in the Distant Universe', Vol. 308 of *Astrophysics and Space Science Library*, p. 187.

Schmidt, R., Webster, R. L. and Lewis, G. F. (1998), 'Weighing a galaxy bar in the lens Q2237 + 0305', *MNRAS* **295**, 488.

Shakura, N. I. and Sunyaev, R. A. (1973), 'Reprint of 1973A&A....24..337S. Black holes in binary systems. Observational appearance.', *A & A* **500**, 33–51.

Tombesi, F., Cappi, M., Reeves, J. N. and Braito, V. (2012), 'Evidence for ultrafast outflows in radio-quiet AGNs - III. Location and energetics', *MNRAS* **422**, L1–L5.

Tombesi, F., Cappi, M., Reeves, J. N., Palumbo, G. G. C., Yaqoob, T., Braito, V. and Dadina, M. (2010), 'Evidence for ultra-fast outflows in radio-quiet AGNs. I. Detection and statistical incidence of Fe K-shell absorption lines', *A & A* **521**, A57.

Tombesi, F., Meléndez, M., Veilleux, S., Reeves, J. N., González-Alfonso, E. and Reynolds, C. S. (2015), 'Wind from the black-hole accretion disk driving a molecular outflow in an active galaxy', *Nature* **519**, 436–438.

Treu, T. (2010), 'Strong Lensing by Galaxies', *Annual Review of Astronomy and Astrophysics* **48**, 87–125.

Ulrich, M.-H., Maraschi, L. and Urry, C. M. (1997), 'Variability of Active Galactic Nuclei', *Annual Review of Astronomy and Astrophysics* **35**, 445–502.

Vignali, C., Iwasawa, K., Comastri, A., Gilli, R., Lanzuisi, G., Ranalli, P., Cappelluti, N., Mainieri, V., Georgantopoulos, I., Carrera, F. J., Fritz, J., Brusa, M., Brandt, W. N., Bauer, F. E., Fiore, F. and Tombesi, F. (2015), 'The XMM deep survey in the CDF-S. IX. An X-ray outflow in a luminous obscured quasar at z $\approx$ 1.6', *A & A* **583**, A141.

Wambsganss, J., Brunner, H., Schindler, S. and Falco, E. (1999), 'The gravitationally lensed quasar Q2237+0305 in X-rays: ROSAT/HRI detection of the "Einstein Cross"', *A & A* **346**, L5–L8.

Wertz, O. and Surdej, J. (2014), 'Asymptotic solutions for the case of SIE lens models and application to the quadruply imaged quasar Q2237+0305', *MNRAS* **442**, 428–439.